Characterisation of Machine Element Contacts Using Ultrasound Reflectometry

Lu Zhou

Thesis submitted for the Degree of Doctor of Philosophy

Department of Mechanical Engineering

The University of Sheffield

May 2015

Summary

Machine elements are used widely in all industrial areas and every mechanical system. From small elements, such as all kinds of bearings, bolted joints, etc., to large components like wheels and rails, and wind turbine bearings, contacts occur that need to be managed carefully. Machine elements are worn and damaged over long periods of contact with each other. By investigating these contacts and studying the behaviour of contacting bodies, unnecessary failures and even accidents can be avoided with proper maintenance and optimal component design. However, it is difficult to put sensors in the contact area as there is not enough space between two touching bodies. Besides, a lot of contacts take place inside machines or devices. Research of machine element contacts especially wheel-rail contact has been carried out for years. A number of approaches have been developed to characterize the contact, but most of them either alter the contact conditions with the sensors used or can only show part of the contact information using indirect derivation.

The ultrasonic scanning approach has long been used in medical imaging. It is a non-destructive method as the ultrasound signals can penetrate materials without affecting them. The method solves the problem of sensors not being able access directly to the contact area. Therefore a lot of work has been done on characterizing contacts using ultrasound. The method is carried out by pulsing a beam of ultrasound signals from one side of one contacting body and receiving reflected signals from the interface. The contact area can be viewed by plotting the reflected signals as a distribution map. The contact information is reflected in the changes of signal strength and phase shift. By analogizing the interface asperities as springs, the equivalent spring stiffness, noted as the interfacial stiffness can be derived, and from this the contact pressure can be calculated. Previous ultrasound measurement work has basically focused on static and metal-to-metal contacts. In this project, the ultrasound measuring method will be used in a wider range of conditions.

In this thesis, a novel ultrasound scanning technique was developed for real-time contact measuring and monitoring dynamic contacts. The technique was applied on a ball-on-flat contact which represents a normal ball bearing contact, and more importantly on a wheel-rail system aiming to characterize the wheel-rail contact dynamically. What is more, pioneering work is done using the ultrasound static and dynamic method in different conditions including non-metal, non-linear contacts and multi-body contacts.

Acknowledgements

At the completion of the thesis, firstly I would like give my greatest appreciation to my supervisor Roger Lewis. He led me to the field of Tribology, I would never have carried out the research work without his meticulous guidance. Throughout the whole PhD period, he has always been kind and patient. Even when I got stuck in my research or faced issues, he has been forgiving and encouraging. I feel very fortunate and pleased for being his student and I really expect future cooperation with him. I also would like to thank Matt Marshall for his support. He raised up a lot of useful and smart ideas for me when I have problems thinking about how to design new tests. Also he provided many suggestions on data post processing and figure presentation which are truly helpful. I am enlightened and inspired each time I have a chat with him.

Thanks also to Henry Brunskill, it is him who actually taught me everything about ultrasound tests, from how to use the equipment to test design and much more. His enthusiasm and passion in research work and experiments encouraged me and kept pushing me forward. He gave me a lot of chances to do ultrasonic related jobs other than my thesis work. I am progressing greatly with these experiences.

Besides, thanks to my colleagues Luke Buckley-Johnstone, Chris Hardwick and Oliver Burke. It has really been a great time working with you. I would especially like to thank Robin Mills who really helped me a lot in programming and solving software problems. Thanks to Stephen Lewis who provided much effort and help in my full scale wheel-rail tests. I must mention the only technician in the Tribology group Dave Butcher, he is the most amiable and talkative technician I have met here. I have never been disappointed giving my machining jobs to him.

Thanks to all my friends for their support. Especially for an uncommunicative person like me, it would have been a dull and lonely life without your companionship. You have brought happiness and a smile to my life every day.

Last and the most important, I would like to send my exalted gratitude to my parents. Not only because of their huge amount of financial support which realized my further study wish, but also of their selfless dedication in bringing me up. Thanks very much to my mother Ke Ping Gan for her caring and concerns, and thank my father Hui Xin Zhou for his inspiration when I am in depression. Although I'm 9000 kilometres away from my home, I can still feel their love strongly. My PhD journey cannot be called smooth, it has been tough studying alone overseas, particularly when I have been suffering from illness for years. But their love and expectance helped me made through, I love you both so much.

Nomenclature

v	Velocity, m/s
ρ	Density of material, kg/m^3
μ	Coefficient of friction, dimensionless
F	Nominal, measured friction force during sliding, N
P	Applied load (normal force), N
k	ellipticity ratio
p_0	Hertzian peak pressure, MPa
$\dot{\boldsymbol{s}}$	Rigid slip
ξ_x	Longitudinal creepage, dimensionless
ξ_y	Lateral creepage, dimensionless
φ	Spin creepage, dimensionless
$\boldsymbol{F_t}$	Traction force, N
σ	Maximum compressive stress, MPa
t	Block width, mm
D	Ring diameter, mm
R_a	Centre-line average surface roughness, m
D	Diameter of the sphere, m
E^*	Reduced elastic modulus, dimensionless

$E_{1,2}$	Elastic moduli (Young's moduli) of the two specimens, Pa
v	Poisson's ratio, dimensionless
R_x, R_y	Radius measurement in the horizontal and vertical directions respectively, m
U	Speed parameter, dimensionless
G	Materials parameter, dimensionless
W	Load parameter, dimensionless
K	Approximated elipticity parameter, dimensionless
$\boldsymbol{u}_{1,2}$	Displacement pf the particles, m/s
α	Pressure viscosity coefficient, dimensionless
λ	Wavelength, m
c	Speed of sound in medium, m/s
f	Frequency of ultrasound, MHz
z	Acoustic impedance of medium, $kg/m^2s \times 10^6$
R	Reflection coefficient, dimensionless
ω	Angular frequency of pulse, radians
K	Interfacial stiffness, GPa/μm
a	Major semi axis of Hertz contact ellipse, mm
b	Minor semi axis of Hertz contact ellipse, mm
p_{btm}	Bottom limit pressure for contact area calculation, MPa

Contents

Chapter 1:

Introduction

1.1 Contact Stress and Failures

The railway system is the most common and widely used transportation in the world. With the development of transportation and proceeding of worldwide industrialization and urbanization, the railway as an economic, low-carbon and high capacity transportation, has been playing a more and more important role. Increasing demands on security, efficiency, convenience and comfort lead to higher criteria on capacity and speed, and the wheel-rail conditions have become much harsher than before.

Contact stresses are stresses at the interface when two bodies are pressed together, in some situations like ball bearings and the wheel-rail system, the contact stresses are significant. In these cases, different kinds of failure can occur.

Due to heavy load, the wheel and rail or the ball bearing can be damaged by the transient impact of high pressure. But more frequently, the contacting surfaces are suffering from another type of failure known as Rolling Contact Fatigue (RCF). The wheel-rail contacts are normally intermittent, one section of the rail is in contact with the wheel cyclically as locomotives pass over rail tracks, and the rail is loaded and unloaded alternatingly. Tiny cracks grow in the wheel and rail in the long term, meanwhile the plastic material flow is taking place. Here tiny cracks refer to those initiated by strain accumulation in the material and ratchetting, and propagating below the surface. As strain accumulates, the material fails, which leads to wear or crack initiation. For all wear and failure types, materials of the wheel and the rail are being removed during the process, and eventually the wheel and rail are either catastrophically worn out or fractures occur inside the body without regular maintenance. Similar failure can happen in the ball bearing case. The bearing can suffer from flaking (the bearing frame material peels off) due to suffering from cyclic contact stresses and pitting (the holes about 0.1mm in depth generated on the surface of the raceway) due to rolling contact fatigue.

The contact stress is significant in these situations, higher contact stress increases the chance of crack generation and accelerates the rate of rolling contact fatigue. Besides, according to Archard's Law, the total wear volume is proportional to normal load, which means higher contact stresses lead to more severe wear. Therefore, the contact

stress is important in limiting the maximum life of wheel and rail or other machined elements. It is a vital parameter in designing and predicting the lifespan of a component.

The average contact stress is dependent on the size of the contact. For a certain normal load, the larger the contact size is, the lower the average contact pressure will be, and the averages indicate the information at the contact area. Therefore it is essential to determine the contact size as well as contact stress.

1.2 Measurement of Contact

In Section 1.1, the importance of contact stress has been discussed. In this section, methods of measuring contact stresses will be reviewed. Determination of contact stresses as well as contact sizes has long been a core topic in previous research work on contact mechanics. The methods are generally classified into theoretical and experimental. The theoretical techniques include analytical and numerical methods. Among which the most typical one is the Hertz theory, in which two elastic parabolic bodies are assumed to be pressed together and equations were proposed. The contact area is elliptical in Hertz theory, through the equations, the analytical solutions for contact stress distribution and semi axes of contact ellipse can be obtained.

In terms of the wheel-rail contact problem, a two dimensional simplified model was built by regarding the wheel rail movement as a cylinder rolling over a plane. The problem was first solved by Carter [1]. Johnson and de Pater solved the three dimensional case 30 years later by applying the Hertz theory [2]. As with the general wheel-rail case which involves traction force, lateral, longitudinal and spin creepages, the three dimensional elastic rolling contact was solved by Kalker with a numerical algorithm. A program CONTACT was developed using this algorithm [3]. Another simplified version known as FASTSIM was proposed for avoiding high computational time. In the algorithm, Hertz equations was also used for solving the normal contact stresses [4]. Currently, Hertz theory is stilled widely used for prediction and validation of other experimental measurements.

A model was proposed by Cretu [5] which solves non-Hertzian contact. The model is still based on half space and elastic deformation, but the profile of the contacting bodies can be any shape, roughness is also considered. A program called NON-HERTZ was developed under the model and it is solved with the conjugate gradient method. Non-Hertzian contact area was estimated by a pair of equivalent ellipses by Sauvage [6].

However, the analytical methods have a lot of limitations. The Hertz theory is based on the assumption that the contacting bodies are infinitely large, the deformation is elastic

and the surfaces are perfectly smooth. Profiles of the contacting bodies are simplified as well. But in real cases, when normal load increases to a certain extent, plastic deformation is inevitable. The components have finite sizes and the interfaces can be irregular and rough. In brief, most contacts in reality are non-Hertzian and Hertz theory can no longer be applied. Numerical methods and experimental measurements are needed for more accurate ways of obtaining contact stresses.

With the development of computational techniques, work on simulations of contacts with aid of computers has been increasing. The finite element analysis (FEA) has been a common method for solving contact problems and calculating contact stresses. The finite element method is carried out by dividing the contacting bodies into joint elements, the dividing process is called meshing, the elements can be triangular, tetrahedral, hexahedral, etc., and there are several types of elements specially for solving contact problems. As the analysis starts, the two contacting bodies are pressed together under a pre-set normal load, the bodies are meshed and basic parameters are set for the elements, the simulations are carried out with different algorithms chosen, iterative procedure is performed. After simulation, contact area and contact stresses distribution can be viewed straight forwardly on the model.

Intuitively, the smaller size a single element is, the more elements a body will be meshed into, the simulation results will be of higher resolution and better, but this results in more computational time. Therefore the capability of FEA is largely dependent on the hardware configuration of computers. With the development of computers, the FEA software became more powerful. Previously FEA only dealt with elastic problems and no surface roughness was considered. In recent years, the plastic effect has already been included into packages of some software, and roughness has also been modelled for simulation in some research work.

However it should be noted that the FEA is quite sensitive, the results can be influenced by a variety of factors such as initial boundary condition settings, constraints and even meshing methods. Inappropriate parameter or algorithm chosen will also lead to divergent results during the iterative process.

Both theoretical predictions and FEA have their limitations in reconstructing contact environments as close to the real one as possible. Experimental measuring methods do not need to simulate the contact and observe the contacting bodies directly. But a proper measuring experiment has always been difficult, since no detectors or sensors can be put inside two interacting bodies without damaging the contact. In the remaining part of this section, several kinds of measuring techniques will be discussed.

An electrical resistance method was presented by Bowden and Tabor for measuring real contact area [7]. The electricity is transmitted through the contact between two conductive bodies, and the method is based on detecting the amount of transmitted electrical energy. The main disadvantage of the method is that only contact area can be acquired through this method, no contact stress is involved. What is more, the result is significantly affected by oxide layers on the surfaces of the components.

Optical methods have also long been used for characterising contact [8]. A typical optical method is photoelasticity. The method is based on the double refractive properties of some materials when they are pressed. The contact stress distribution can be derived from the photoelastic model. But most engineering components are made of metal rather than materials with double refractive properties. There are previous work on measuring contact stresses of two gear teeth by reconstruct the components with a photoelastic material. Apparently, the contact stress measured from reconstructed models are inaccurate with materials altered, the elastic modulus and Poisson ratio all changed. The normal load which can be reproduced is also limited as the photoelastic material cannot sustain as high a load as metal or other common engineering materials do.

A pressure sensitive film was used for contact stress measurement more recently [9]. The pressure film is placed in between the surfaces of two contacting components. Microcapsules of dye are pre-enclosed into the film, and the colour (normally red) will be shown on the film in reaction to pressure. Variation of the colour represents the pressure distribution. However, the film has a certain thickness (around 0.5mm) and the contact conditions can be severely altered when a film is placed in. The contact is spread with the presence of elastic film. Besides, the pressure sensitive film has top limits on detecting contact stresses. Even with the film series for high pressure measurement, the maximum pressure that can be measured is 300MPa, which is far lower than normal wheel rail contact stresses.

Air flow has been used as a contact measuring tool [10]. The method is applied by firstly simplifying the wheel-rail contact as a cylinder rolling over a plate, and a row of holes are drilled on the plate, low pressure air is blown through the holes. When there is no contact, air flow can escape from holes freely; and when the wheel goes over the holes on the rail, the air flow is blocked leading to an increase of air pressure. By measuring the changes in the air pressure the contact information can be characterized. This method is simple and straightforward, the contact size can be easily obtained. However, the holes drilled on the rail inevitably alter the contact conditions. What is more, due to the physical sizes and the arrangement of the holes, the results are low resolution.

All the experimental methods discussed above have limitations and lack accuracy in terms of measuring contact stress. Some methods also inevitably changes the contact conditions.

1.3 Aims of the Project

The main aim of the project was to develop a new real-time non-destructive tool using ultrasonic technique for characterising dynamic contacts of engineering components including ball bearings and wheel rail. The applicability of the dynamic ultrasonic measuring method was tested in different ways. Static measurements were taken using an ultrasound scanning method prior to dynamic tests. Theoretical predictions and FEA were carried out for validation and comparison. Besides, the contact between wheel and rail endpost was also investigated using ultrasound and FEA was performed as a comparison.

With the development of a non-invasive measuring technique, information of contacts can be captured in real time. Not only contact pressure or contact size, but also the effect of slip may be reflected in the measurements, and determination of the slip using ultrasound will be included in future work. This technique can be applied in a range of materials including normal and head hardened rail.

1.4 Layout of the Thesis

The thesis is laid out in the following structure. The contact mechanics and the basic theories of wheel-rail contact are outlined in Chapter 2. A literature review of previous work on characterising wheel-rail contacts is presented in Chapter 3. The principles of ultrasound and general design of experiments is presented in Chapter 4 and Chapter 5.

In Chapter 6 the ball-on-flat contact is investigated, static and dynamic nitrile ball on perspex plate interfaces were measured using an ultrasound scanning probe and the novel dynamic ultrasonic technique respectively. Steel ball-to-steel plate rolling contact was also measured. Chapter 7 contains static wheel-rail contact measurements using ultrasound scanning with comparison to theoretical predictions and FEA. In Chapter 8 the new ultrasound scanning technique is used on the full scale wheel-rail test rig for dynamic wheel rail contact measurements. Finally Chapter 9 presents the study of rail endpost and wheel contact using ultrasound and FEA. The conclusions are in Chapter 10.

Chapter 2:

Wheel-Rail Contact Mechanics

2.1 Introduction

Nowadays railway transportation is developing rapidly worldwide. Wheel axle loads and speed of locomotives keep increasing, which puts forward growing demands on the requirements of the wheel-rail contact conditions. Increasing wear will occur in the process, which will reduce the stability of locomotives, decrease ride comfort and raise the potential risks of derailment. Therefore, it is essential to find a methodology to look into and analyse the wheel-rail contact.

Wear and fatigue related damage mechanisms of materials in contact are largely related to contact stresses. Therefore the study of contact mechanics is vital to understanding failure of materials and for scheduling maintenance processes. Different types of machine-element-contact have been studied using various methods. Theories from Hertz to Three Dimensional Rolling Contact [3] have been developed for contacts under varied conditions. Among all contacts between machine-elements, the wheel-rail contact has been a separate issue being investigated for years. Due to the sensitiveness of the open system and the complexity of wheel and rail profiles, currently there is no theory or model which fully characterises a wheel-rail contact, especially for the dynamic case under field conditions. The wheel-rail contact is determined by loads, types and profiles of wheel and rail, the roughness of the contacting surfaces and contact positions etc. In terms of rolling contact, rolling speed, creepages and friction should also be considered. Study of these factors are helpful to wheel-rail contact estimation and prediction.

The aim of this project is to investigate a ball-on-flat contact before proceeding to asses wheel-rail contact problems using experimental and numerical methods, namely, ultrasound reflectometry and the finite element method. Results from ultrasound reflectometry will be compared with finite element simulations for wheel-rail contacts and wheel-rail endpost contacts, and these two methods will be compared with Hertz predictions for static wheel-rail contacts. The initial focus was on static measurements before moving to develop dynamic approaches.

The main part of the project is to develop methodologies to obtain a static and dynamic contact characterization of the wheel-rail contact.

2.2 Surface Roughness

All machine element surfaces have roughness. No matter how a component is machined, the surface of it cannot be absolutely smooth. Even through grinding or polishing, the surface is rough at the micro scale. If the surface is zoomed in on with a microscope, inherent peaks, tiny grooves and corrugations can be observed. The surface roughness has significant influence on fatigue strength, sealing properties and wear. What is the most important in terms of this thesis work is that the surface roughness has a great impact on contact stiffness which is directly related to contact pressure calculations.

As can be seen from Figure 2.1, once a mean line is defined following the criteria that the material above is equal to the missing part below, all extreme points above the line are called peaks and those extreme points below are called valleys. Then how rough a surface is can be numerically described according to the height of peaks and valleys measured from the mean line. There are a lot of parameters to describe how rough a surface is, such as R_v and R_p which represents maximum valley depth and maximum peak height respectively, and R_t which is the difference of R_v and R_p. Further there is the root mean squared roughness R_q which is the root square of the variance of height. But among all these parameters, the arithmetic average roughness R_a is the most commonly adopted one. For continuous cases it can be calculated from Equation (2.1):

$$R_a=\frac{1}{L}\int_0^L|y|\,dx \tag{2.1}$$

where L is the sample length, and y is the height measured from the mean line. Or it can be calculated from Equation (2.2) for discrete cases:

$$R_a=\frac{1}{N}\sum_{i=1}^{N}|y_i| \tag{2.2}$$

where N is the number of sample points.

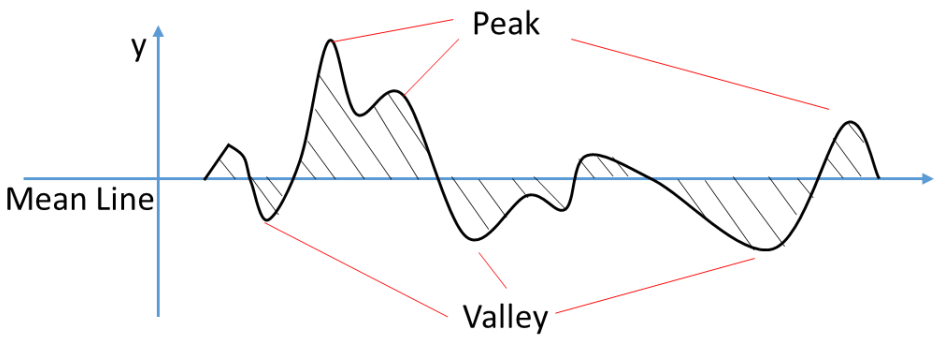

Figure 2.1 Peaks, Valleys and Mean Line for Roughness Definition

2.3 Wear and Failures of Wheel-Rail Contact

The wheel and rail are damaged under high load and long term usage, the most common damage type is wear, which is material loss from the wheel and rail. Another one is rolling contact fatigue, abbreviated as RCF, which leads to cracks and even fracture of the rail. The wear is dependent on the normal load, slip, lubricants etc. Several types of wear will be displayed by changing slip as one of the influencing factors. Here, the slip refers to the percentage of the speed difference of contacting points between the wheel and the speed relative to the ground.

Lewis & Dwyer-Joyce did a series of twin disc wear tests investigating wear mechanisms and transitions of the wheel-rail contact [11]. The severity of wear is assessed through the wear rate. Figure 2.2 shows the wear rate curve with respect to slip and the corresponding type of wear. In the figure oxidation, mild delamination and severe delamination are typical types of mild, severe and catastrophic wear respectively. Figure 2.3 shows the wear growth and crack formation of the wheel disc with increasing slip. Under 1500MPa contact pressure and 0.2 percent slip, an oxide layer and low subsurface deformation was observed (Figure 2.3a). The deformation grew deeper under 3 percent slip, cracks started growing as well (Figure 2.3b). More cracks were found and the material started breaking away under 5 percent slip (Figure 2.3c).

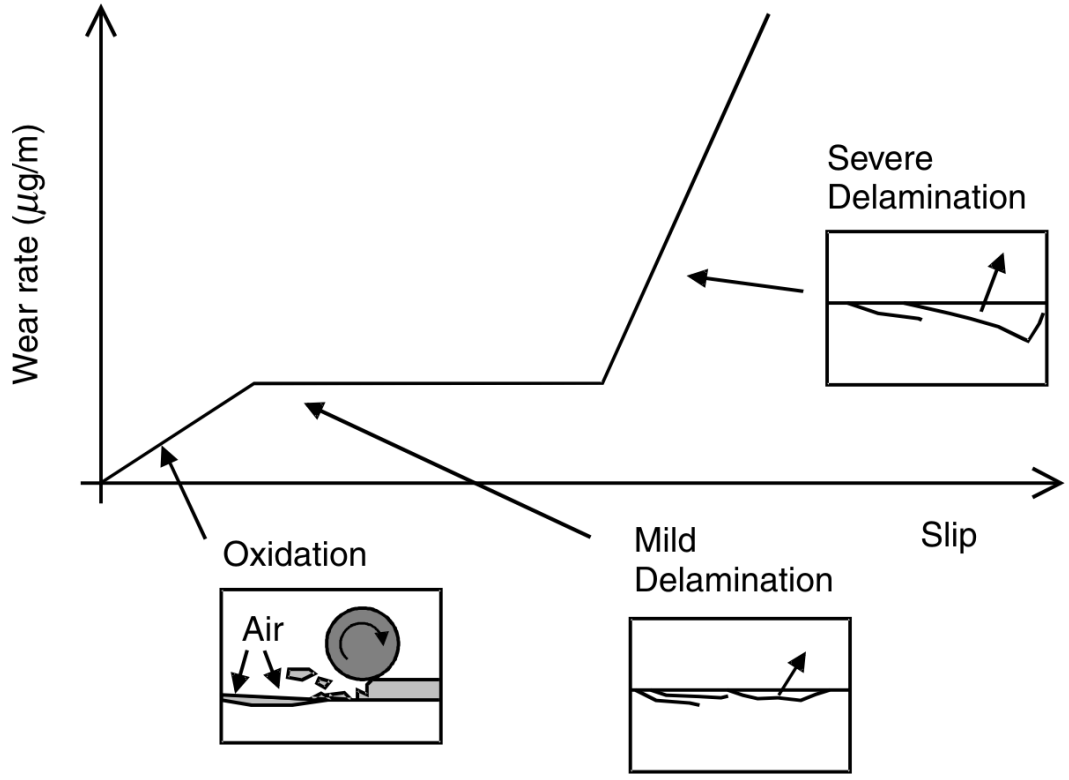

Figure 2.2 Schematic diagram of wear features and regimes [11]

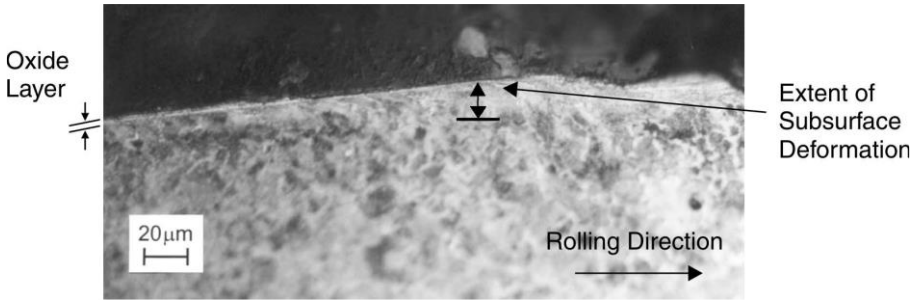

(a) 1500MPa; 0.2 percent slip

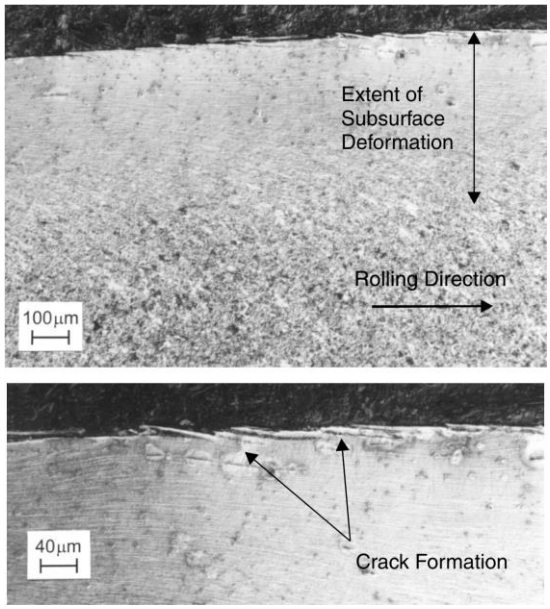

(b) 1500MPa; 3 percent slip

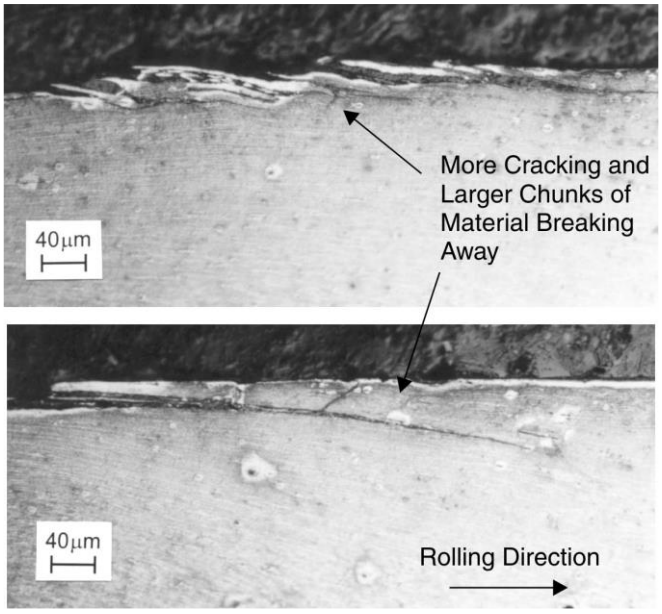

(c) 1500MPa; 5 percent slip

Figure 2.3 Section parallel to the rolling direction through the wheel disc run [11]

2.4 Wheel and Rail Profiles

Cross sections of a S1002 wheel and BS113A rail are shown in Figure 2.4, the wheel profile is divided into three regions: wheel tread, wheel flange and transmission region. The profile in the wheel tread region has the largest radii of curvature and the flange part is most curved with the transmission region in between. A similar classification can be seen in the rail profile where the rail head is flattest and the rail corners are much more curved. According to Hertz theory, the contact patch is related to the radius of the two contacting bodies. For a fixed applied normal load, flatter contact surfaces therefore lead to larger contact patch and smaller nominal contact pressures.

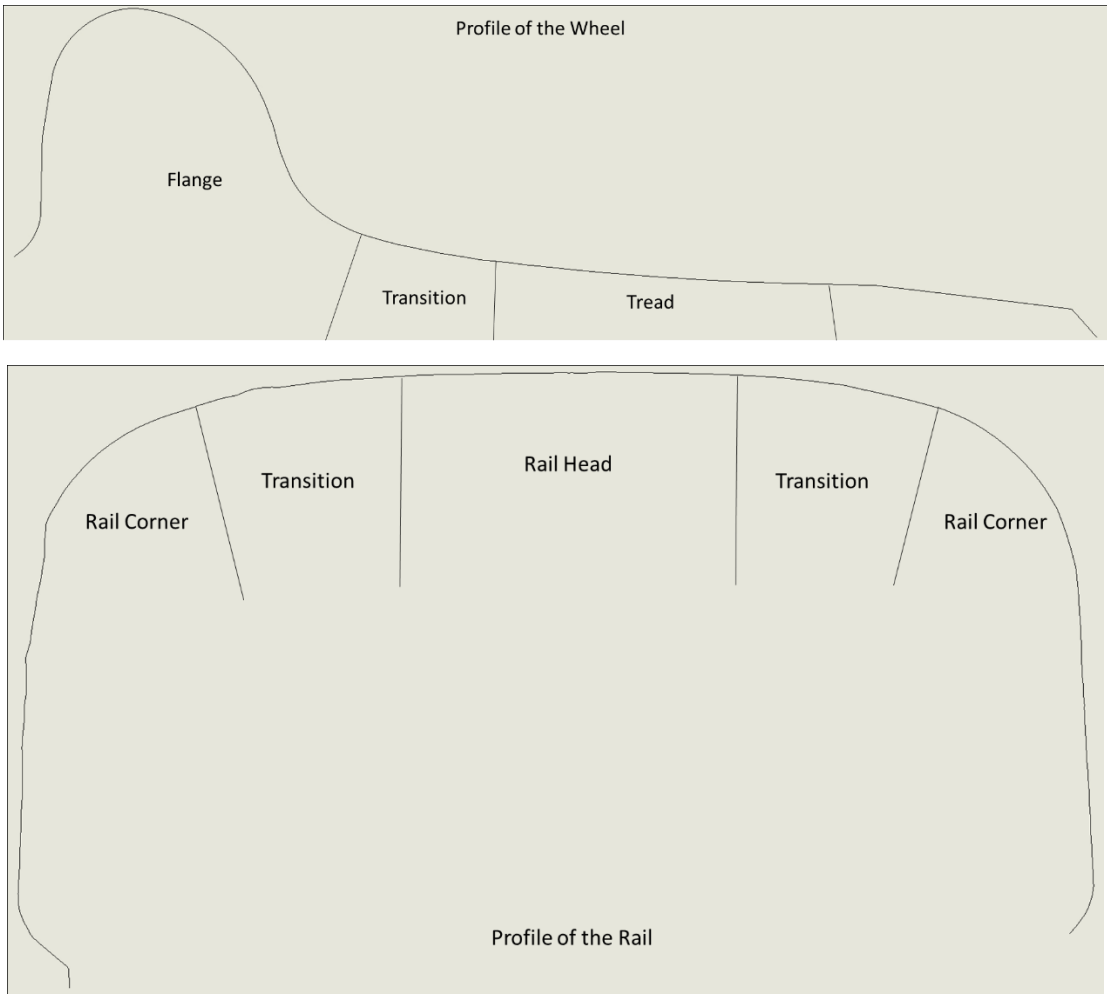

Figure 2.4 Profile of S1002 Wheel and BS113A Rail

2.5 Contact Position

The contact is also quite sensitive to the relative position of the wheel and rail, especially position in the lateral direction and the attack angle, which refers to the angle between the rolling direction of the wheel and the longitudinal direction of the rail

(shown in Figure 2.5). The wheel and rail profile is designed to largely give contact between the wheel tread and rail head because a relatively large contact patch and small contact pressure is expected. This leads to mild wear and longer life span (Figure 2.6a). However in reality, when the train is passing through a curve, the wheel flange comes into contact with either side of the rail, known as the flange contact (Figure 2.6b). Rail tracking position will influence contact position as well. The rail tracking position refers to the wheel axle position relative to the centre line of the rails. Ideally the centre of the wheel axle is always coincided with the centre line of the rails, but there are random lateral movements which lead to the axle centre being laterally displaced from the centre line as the train keeps moving, which is normally known as the lateral slip. As the radii of curvature around the wheel flange and rail corner are far smaller than those in the wheel tread and rail head region, the contact patch is much smaller and the contact pressure becomes quite high. Flange contact will lead to stress concentration, plastic deformation and severe wear, thus it should be to the largest extent avoided. On the other hand, ideally the rolling direction of the wheel should be parallel with the longitudinal direction of the rail, which means the attack angle should be zero. However, the wheel is in contact with the rail with an angle sometimes due to axle spin. Attack angle leads to a change of contact patch and potential risk of more wear and fatigue.

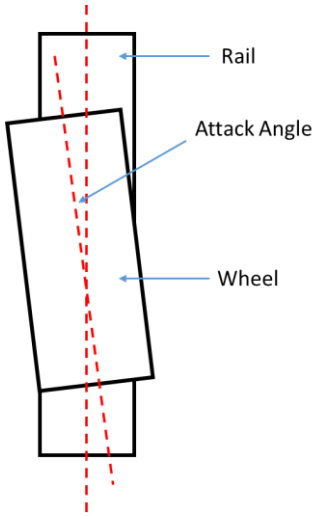

Figure 2.5 Attack Angle between Wheel and Rail

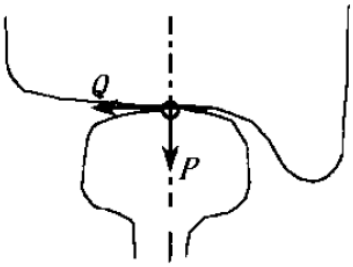

Figure 2.6a Wheel Tread-Rail Head Contact

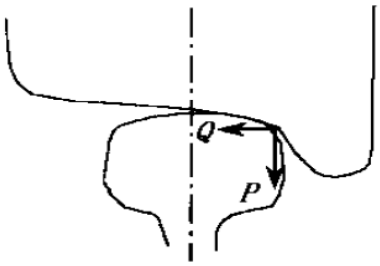

Figure 2.6b Wheel Flange-Rail End Contact

When the train is going along straight rail tracks and no flange contact takes place, the wheel is not always in contact with the same region on the rail. Tiny lateral displacements will lead to a large difference in final contact outcomes. As the train keeps moving, position and shape of the contact is changing continuously with the transmission region of the wheel and the rail coming into contact from time to time.

2.6 Contact Shape

According to classic Hertz theory and three-dimensional rolling contact theory, in terms of normal wheel tread-rail head contact, the contact shape is elliptical and only one contact patch is expected, as shown in Figure 2.7, the yellow part indicates the contact area. However, as the wheel and the rail wear and deform gradually with constant contact, the profile of the wheel fits closer against profile of the rail and the contact becomes more conformal. This leads to a larger irregular contact patch or even multiple contact patches (Figure 2.8).

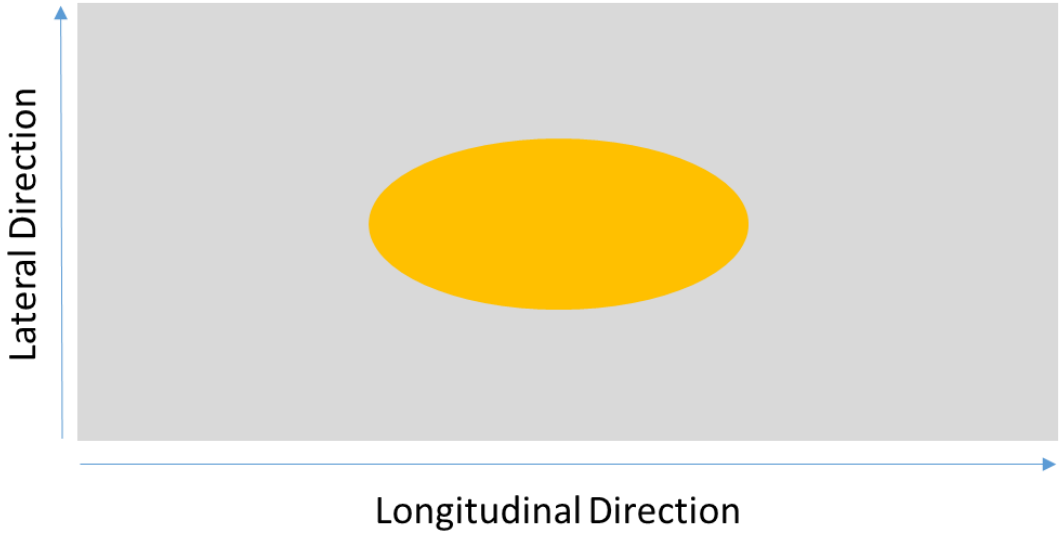

Figure 2.7 Wheel Tread-Rail Head Contact Simulation

Figure 2.8 Conformal and Multiple Wheel-Rail Contact

2.7 Summary

In this chapter, basic concepts and factors involved in wheel-rail contact are presented. The definition and classification of surface roughness of machine element surfaces is described. Surface roughness plays an important role in contact pressure determination. Typical types of wear caused by long term contact under different slips are also showed in the chapter. Wear is influenced by a number of factors, increasing normal load, i.e., contact pressures or slip will lead to more severe wear conditions. Through measuring contact pressure, the wear can be monitored and predicted more accurately. The wheel-rail contact is sensitive to profiles of wheel and rail and positions of contact, both of which are introduced in this chapter too. Both contact pressure distribution and contact shape change with different types of wheels and rails in contact, and multiple contact patches can be observed in some contact positions. By understanding this a better test environment can be designed to test the new pressure measuring approach.

Chapter 3:

Literature Review

3.1 Introduction

The interfaces between machine elements especially the wheel-rail contact have been studied for years using different methods. In this chapter, some previous work carried out on this will be reviewed and discussed. The work includes basic contact mechanics theory and research work on characterizing wheel-rail contacts using different techniques.

3.2 Contact Mechanics Background

3.2.1 Hertz

The Hertz theory deals with classic elastic contact problem and analytical solutions can be obtained. The theory assumes the contacting surfaces are ideally smooth, which means no roughness exists. Only elastic deformation is considered. Generally as with two curved bodies (shown in Figure 3.1), the contact will be a single point or a line.

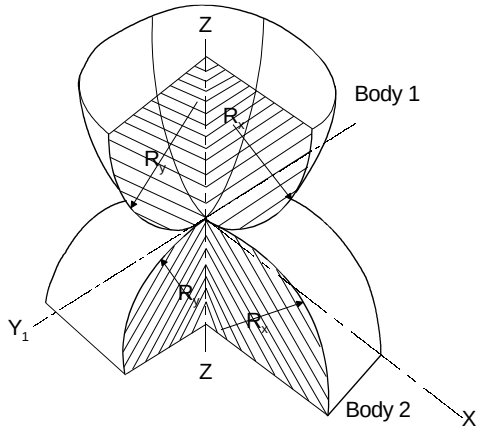

Figure 3.1 Two Curved Bodies in Contact

The curved surface of each body has a radius along x direction R_x and y direction R_y respectively. For a normal elliptical point contact, the contact size and contact pressure can be calculated as:

$$a = \sqrt[3]{\frac{3k^2 \boldsymbol{E} P R'}{\pi E^*}}, b = \sqrt[3]{\frac{3 \boldsymbol{E} P R'}{\pi k E^*}} \tag{3.1}$$

$$p_0 = \frac{3P}{\pi ab}, p(x,y) = p_0 \sqrt{1 - \frac{x^2}{a^2} - \frac{y^2}{b^2}} \tag{3.2}$$

where a and b are semi axes of the contact ellipse (Figure 3.2), p_0 is the maximum contact pressure, R' is the reduced radius of curvature and is calculated through:

$$\frac{1}{R'} = \frac{1}{R_x} + \frac{1}{R_y}, \frac{1}{R_x} = \frac{1}{R_{1x}} + \frac{1}{R_{2x}}, \frac{1}{R_y} = \frac{1}{R_{1y}} + \frac{1}{R_{2y}} \tag{3.3}$$

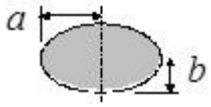

Figure 3.2 Contact Ellipse

k is the ellipticity ratio a/b and $\boldsymbol{E}$ is an elliptical integral of the second kind. These two parameters can be approximated by:

$$k = 1.0339 (\frac{R_y}{R_x})^{0.636}, \boldsymbol{E} = 1.0003 + \frac{0.5968 R_x}{R_y} \tag{3.4}$$

E^* is the combined Young's Modulus of two bodies and can be calculated by:

$$E^* = (\frac{1-v_1^2}{E_1} - \frac{1-v_2^2}{E_2}) \tag{3.5}$$

v_1 and v_2 are the Poisson's ratios of the contacting bodies; E_1 and E_2 are the Young's Modulus of the two.

When two cylinders are pressed against each other(as shown in Figure 3.3), the contact patch is a line. Similar equations can be obtained.

$$b = \sqrt[3]{\frac{4P'R'}{\pi E^*}} \tag{3.6}$$

$$p_0 = \frac{2P'}{\pi b}, p(x) = p_0 \sqrt{1 - \frac{x^2}{b^2}} \tag{3.7}$$

where b is the half width of the contact rectangle, P' is the load per unit length.

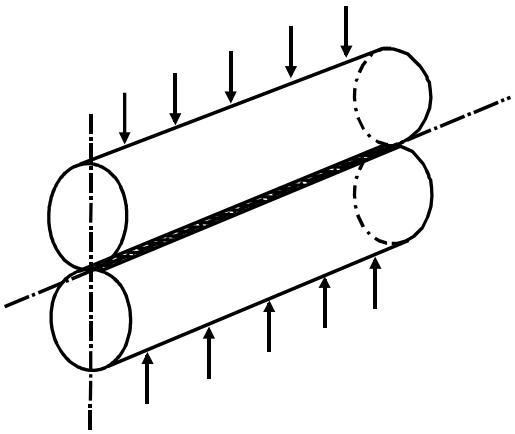

Figure 3.3 Two Cylinder Line Contact

The contacts of machine elements (ball-on-flat, wheel-rail) investigated in the thesis are elliptical point contacts, so the former one is used for analytical prediction and validation. In terms of wheel tread-rail head contact, it is necessary to have a nominal contact area outlined from the Hertz theory even though the real contact area comes from asperities contact and is smaller and discrete.

3.2.2 Three-Dimensional Rolling Contact Theory

The Hertz provides analytical solutions for classic elastic contact problems. But the theory can only be used for calculating normal contact forces. In terms of actual wheel-rail contacts where slip and spin take places, a theory for determining lateral forces is needed. Joost J. Kalker proposed *Strip Theory* [12], *Empirical Theory* [13], and *Simplified Theory* [4] respectively. In 1986, Kalker generalised the principle of virtual work for contact problems and the *Exact Three-Dimensional Rolling Contact Theory* [3] was proposed. The famous FASTSIM algorithm was developed by Kalker in 1982 based on the *Simpilified Theory*, and the *Exact Three-Dimensional Rolling Contact Theory* led to the program CONTACT. Both of which are numerical algorithms.

If one mass suffers a normal load *P* and is pressed with another. The two contact bodies deform at the contact area. The vertical deformation of the two contact bodies is defined as δ, considering two particles: P_1 on body 1 and P_2 on body 2 in contact at one common point (as shown in Figure 3.4). Before deformation, vectors of the two particles relative to global coordinates are $\boldsymbol{x_1}$ and $\boldsymbol{x_2}$ respectively; after deformation, the displacement of the particles are $\boldsymbol{u_1}$ and $\boldsymbol{u_2}$ respectively. Then:

$$\boldsymbol{r_1 = x_1 + u_1, r_2 = x_2 + u_2, r_1 = r_2} \tag{3.8}$$

At the contact point, the normal deformed distance is calculated by

$$e = h - (u_{1n} - u_{2n}) \tag{3.9}$$

In the contact area, the normal deformed distance equals to zero (e=0).

The rolling motion is defined by time steps, the rigid displacement under each time step can be defined as:

$$\boldsymbol{W_\tau} = \int_t^{t+\Delta t} \dot{\boldsymbol{s}}\, V dt, \dot{\boldsymbol{s}} = V[(\xi_x - \varphi y)\boldsymbol{i} + (\xi_y + \varphi x)\boldsymbol{j}] \tag{3.10}$$

where $\dot{\boldsymbol{s}}$ is the rigid slip, ξ_x, ξ_y and φ are longitudinal, lateral and spin creepage respectively. V is the magnitude of the rolling velocity.

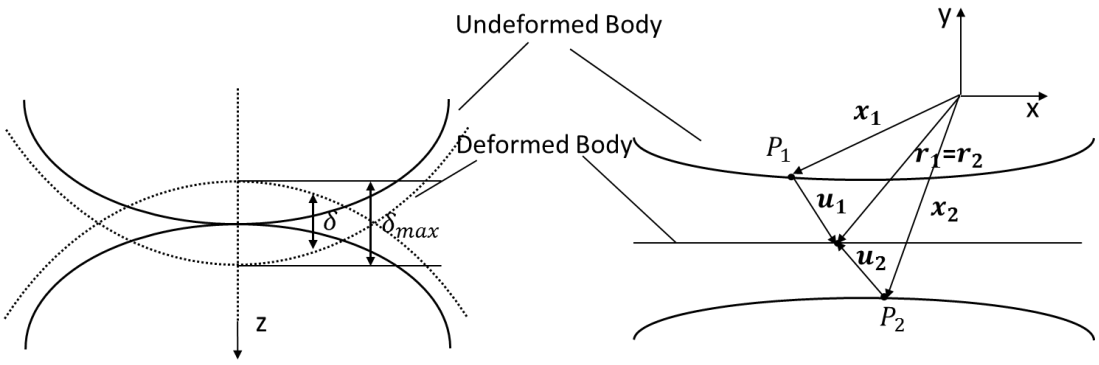

Figure 3.4 Two Bodies in Contact

The contact area under a normal load as well as a tangential traction force, according to Kalker, is divided into a slip area and an adhesion area (as shown in Figure 3.5). The condition for a slip area and an adhesion area follow Coulomb's law as:

$$\begin{cases} |\boldsymbol{F_t}| = \left|[F_{tx}\ F_{ty}]^T\right| \le \mu P;\ |\dot{\boldsymbol{w}}| = 0\ (adhesion\ area) \\ \boldsymbol{F_t} = -\frac{\mu P \dot{\boldsymbol{w}}}{|\dot{\boldsymbol{w}}|};\ |\dot{\boldsymbol{w}}| \neq 0\ (slip\ area) \end{cases} \tag{3.11}$$

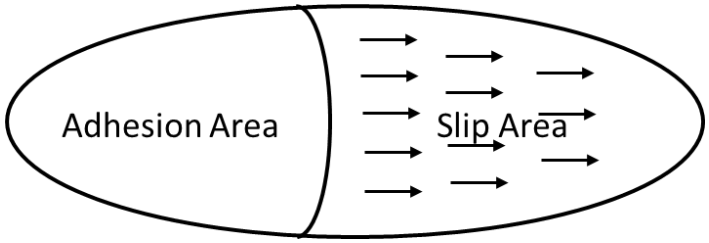

Figure 3.5 Adhesion Area and Slip Area

The boundary condition of a contact area is therefore defined by equation 3.11 and zero normal deformed distance. This can be expressed in the form of the maximum of the virtual complementary work as:

$$\min C_{u,P} = \int_{A_C} (h + \tfrac{1}{2} u_z)\, P dS + \int_{A_C} (\boldsymbol{W}_\tau + \tfrac{1}{2}\boldsymbol{u_\tau} - \boldsymbol{u'_\tau})\, \boldsymbol{F}_t dS \tag{3.12}$$

where $(')$ indicates the previous time step and $\boldsymbol{u_\tau} = [u_x\ u_y]^{\boldsymbol{T}}$.

For contact problems, the displacement at x direction under y direction traction force F_{tj} is given by the linear elasticity as follows:

$$u_i(\boldsymbol{x}) = \iint A_{ij}\boldsymbol{y}F_{tj}\,(\boldsymbol{y})dS \tag{3.13}$$

where A_{ij} is the combined influence function and can be determined analytically for half-space assumption using Bossinesq-Cerruti solution [3].

Equation 3.12 and 3.13 determines the contact area for 3-D rolling contact. These equations are solved discretely by dividing the contact area into equal rectangles. The discretized form of the Equation 3.12 is:

$$minC^*_{PJ_j} = \frac{1}{2}F_{tIi}A_{IiJj}F_{tJj} + [h_J p_{Jz} + (W_{Jz} - u'_{J\tau})\boldsymbol{F}_{tJ\tau}]$$

$$sub\ p_{Jz} \geq 0, \left|\boldsymbol{F}_{tj}\right| \leq \mu p_{jz},\ i,j = x,y,z,\ I,J = 1,\dots,N, N = MX, MY \tag{3.14}$$

The discretized form is implemented in the well-known program CONTACT.

Since Heinrich Hertz proposed his theory in 1882, which provides analytical solutions for two elastic solids in static contact, it has been used widely in the area of contact mechanics including wheel-rail static contact problems for contact sizes and contact force prediction.

Carter [1] first investigated a wheel-rail dynamic contact by using a model of a cylinder rolling over a plate. In 1982, Kalker developed a numerical theory FASTSIM [4] for general wheel-rail elastic rolling contacts which is a simplified version of his CONTACT model [3] proposed in 1990. In FASTSIM it is assumed that the relationship between elastic displacement u and stresses p in the contact plane is linear:

$$U = Lp \tag{3.15}$$

where L is the flexibility coefficient.

The tangential problem is solved in two steps: Firstly the value of the flexibility coefficient of different situations is obtained. Secondly, for a given normal stress distribution and creepages in the contact, the algorithm is applied and the tangential stress distribution is acquired. Three flexibility coefficients were introduced, L_1 for longitudinal displacements, L_2 for lateral displacements and L_3 for spin rotation around vertical axis:

$$L_1 = \frac{8a}{3c_{11}G}, L_2 = \frac{8a}{3c_{22}G}, L_3 = \frac{\pi a\sqrt{a/b}}{4c_{23}G} \tag{3.16}$$

where c_{jj} are Kalker's coefficients which are dependent on ratio of semi-axes of elliptical contact patch and creepages; a and b are semi-axes from Hertz theory; G is the shear modulus of the material.

Polach proposed a numerical algorithm for calculating traction forces [14] in 2000, the algorithm is based on the assumptions that the tangential stress experiences a linear growth with respect to slip from 0 at the leading edge to a maximum at the trailing edge as with the area of adhesion, and that the tangential stress is proportional to Hertzian normal stress for the area of slip. By imposing a proportionality coefficient C, the traction forces can be derived from integrals of tangential stresses. Spin is considered in both Kalker's theory and Polach's theory. A comparison was made between FASTSIM and Polach's [14]. Result differences are negligible, but Polach's method is 17 times faster than FASTSIM in terms of calculation time under 10 divisions.

3.3 Finite Element Analysis Background

3.3.1 Finite Element Method

The Finite Element Method (FEM) is a numerical technique for finding approximate solutions of partial differential equations as well as integral equations. In practical applications it is often known as Finite Element Analysis (FEA). The finite element method originated from the need for solving complex elasticity and structural analysis problems in civil and aeronautical engineering. With the fast development of numerical computation technology, it has spread to all engineering areas including thermal, electromagnetics, fluid dynamics, structural static and transient, linear buckling, modal analysis and so on.

Nowadays, FEA has been widely used in contact mechanics dealing with all kinds of contact problems. It is not limited by the half-space assumption, and both linear and nonlinear, elastic and plastic situations can be solved. A variety of algorithms for contact problems have been put forward, but there are basically three algorithms which are most commonly used in finite element software: pure penalty, normal Lagrange and augmented Lagrange.

3.3.2 Algorithm for Contact Problems

The pure penalty algorithm is a relatively basic algorithm which needs a penalty term to enhance the solving process and is widely used in optimization techniques. As displacement being the only primal input for the equation, it is easier to programme.

To derive the stiffness matrix, the contact zone (encompassing the contact surface) is divided into a series of contact elements. The element represents the interaction between the surface nodes of one body with the respective element face of the other body. Figure 3.6 shows a contact element in a two dimensional application. It is composed of a slave node (point *S*) and a master line, connecting nodes *1* and *2*. *S*0

marks the slave node before the application of the load increment, and *S* marks the node after loading.

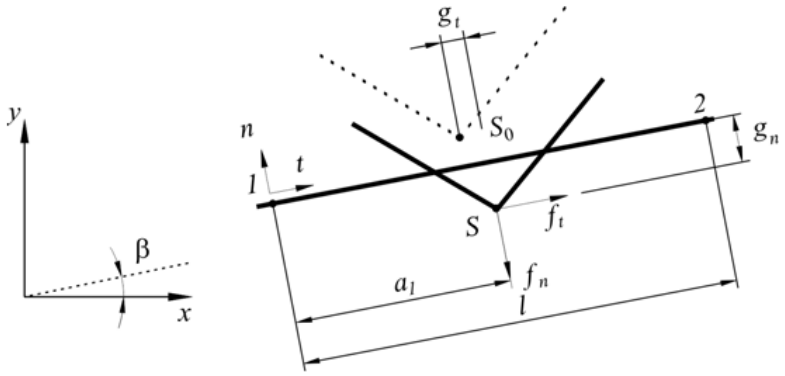

Figure 3.6 Contact Element – Penalty Method

The main disadvantage of the pure penalty method is that it is very sensitive to contact stiffness, which normally could be chosen from 0.01 to 10. Results could vary quite a lot with different initial contact stiffness settings. Besides, it allows penetration for initial contact pairs [15]. Therefore, it is likely to get a result which is not correct without the proper contact stiffness being chosen.

In the case of the classical Lagrange Multiplier Method the contact forces are expressed by Lagrange multipliers. The augmented Lagrange method involves the regularization of classical Lagrange method by adding a penalty function from the penalty method [16]. This method, unlike the classical one, can be applied to sticking friction, sliding friction, and to a frictionless contact.

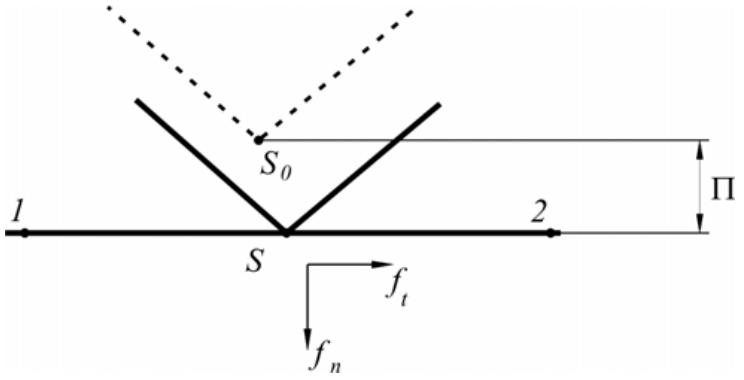

Figure 3.7 Contact Element – Lagrangian Method

Contact stiffness is also needed for the Augmented Lagrangian method. But compared to pure penalty, it is not as sensitive to contact stiffness. Contact stiffness here is not an essential parameter but rather a coefficient to enhance the speed of calculation.

Since simulation software for wheel-rail dynamics was developed in the early 1970s, the finite element method has been proven to be a useful and common method for analysing wheel-rail contact problems. There is a variety kind of software which is specifically for wheel and rail modelling or has wheel and rail modelling packs such as SIMPACK and GENSYS, and simulation software like ABAQUS and ANSYS.

Telliskivi and Olofsson developed a tool which is a macro for building, meshing and analysing a wheel-rail quasi-static model in ANSYS [17]. In the paper, both wheel tread-rail head contact and wheel flange-rail corner contact were modelled and analysed. The Contac49 contact element was used for contact surface meshing and Solid45 was used for the body meshing. The Contac49 element is an element which has five nodes with three degrees of freedom at each node. It is generally used for representing 3-D point-to-surface or surface-to-surface contact. Other similar elements such as Contac12 and Contac48 are used for 2-D point-to-point contact and 2-D point-to-surface contact respectively. The Solid45 element is used for 3-D solid meshing, and it has eight nodes with three degrees of freedom at each node. The element has plasticity, creep, swelling, stress stiffening, large deflection, and large strain capabilities. A normal load of 80377N was applied in both cases; contact sizes and maximum contact pressure were compared with results from traditional methods Hertz and CONTACT. For flange contact, a maximum of 300% difference for contact area and 200% difference in terms of maximum contact pressure was found between FEM and traditional methods. Figure 3.8 shows FEM results compared with Hertz and CONTACT theory.

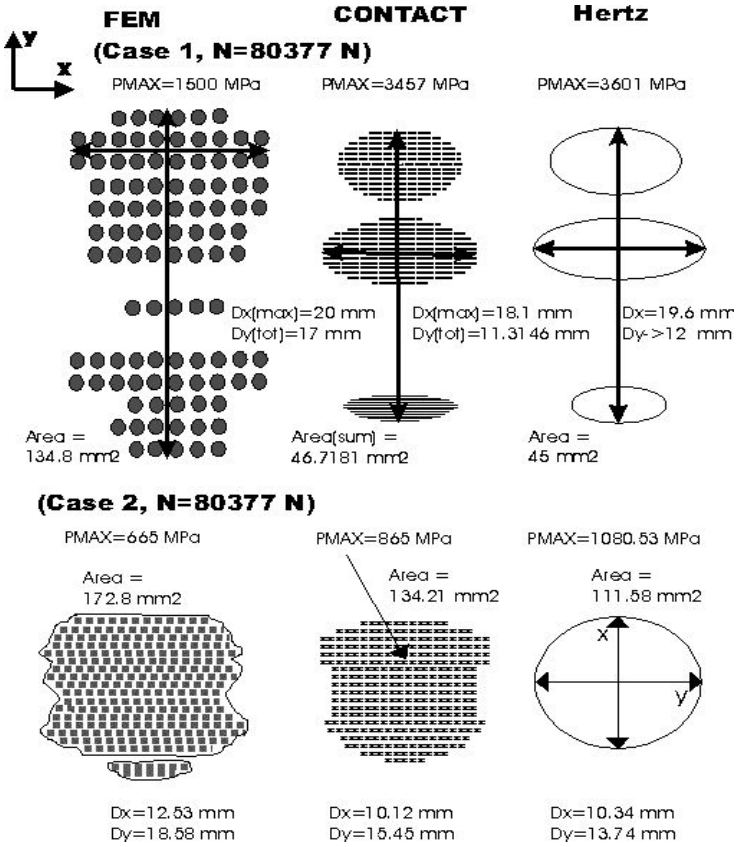

Figure 3.8 Wheel-Rail Contact Patch Comparison between Hertz and FE [17]

Similar research was carried out by Wiest et al. [18] on wheel-rail contacts. The contact point of wheel and rail was close to the wheel flange where the radii of curvature is small, which means for real cases, the contact problem is likely to be conformal and no half-space assumption is applicable. Yet it is worth taking approximations of contact stresses using Hertz and CONTACT as comparison. Both elastic and elastic-plastic finite element models were modelled in Gensys and analysed in ABAQUS, and contact pressure distribution compared with results from Hertz and CONTACT. It was found in the paper that for the elastic finite element case, contact pressure results match well with Hertz and CONTACT outcomes. For the elastic-plastic finite element case, however, simulation results show a large difference compared with the other three methods, with contact area being twice as large and non-elliptical, maximum contact pressure 42% lower than the elastic result and penetration depth 20% larger.

Arslan and Kayabas built a finite element model of a half wheel in contact against a section of rail and analysed the model in ANSYS. A Bi-linear Kinematic Hardening elastic–plastic material model was used [19]. A 100kN load was applied on the wheel shaft and the friction coefficient was set at 0.3. Von-mises stresses together with elastic and plastic strains as well as contact pressure distribution were investigated and plotted for both wheel and rail. Since the contact point was close to wheel flange and the load is relatively high, 696MPa maximum Von-Mises stress was found on the wheel, which went over the yield point of the wheel steel; and 600MPa maximum stress on rail which was above the yield point of rail as well. The contact shape is elliptical and the maximum contact pressure was 1359MPa, which is however not very high. This is due to the adapted elastic-plastic model, where normally much lower contact pressure is expected than pure elastic model.

Vahid Monfared assumed three different shapes of wheel-rail contact area (elliptical (ECS), rectangular (RCS) and circular (CCS)) for numerical stress simulation and analysed contact stresses for each case [20]. Contact stresses under three cases were compared in the format as a ratio of normalized stress divided by exact contact stress with loads from 50kN to 200kN applied. Von-Mises stresses distribution was also simulated and critical points specified to help monitor fatigue and predict crack growth in the wheel-rail contact system.

3.4 Ultrasound Reflectometry

In 1971, Kendall and Tabor first introduced ultrasound reflectometry technology into the field of contact mechanics [21]. They found when the wavelength of an ultrasound signals is long compared to the magnitude of the air gaps between two surfaces, the interface behaves like a reflector， and the contact can be regarded as a spring, the relationship between the reflection coefficient and contact stiffness was proposed. For two contact bodies with same materials, the reflection coefficient is defined as:

$$R = \frac{H_t}{H_i} = \frac{1}{\sqrt{1+(\omega z/2K)^2}} \tag{3.17}$$

where H_t and H_i are the amplitude of the reflected ultrasonic waves and incident waves respectively， the ratio of these two is defined as reflection coefficient *R* by Tattersall [22]. $\omega = 2\pi f$ is the angular frequency of the ultrasonic waves; *K* is the contact stiffness which indicates the load acquired to cause unit approach of the mean lines of roughness for two contacting surfaces, the stiffness increases from zero to infinity with increasing load applied; $z = \rho c$ is the acoustic impedance of contacting material, and ρ is the density and *c* is the speed of sound in the material.

For low applied load, only a small portion of asperities are in contact against each other, it is easy to deform these asperities and therefore the stiffness is low. As the load increases, more asperities are compressed together, it becomes harder to reduce surface separation which indicates growth of stiffness. When the surface load increases to such an extent that all the asperities are pressed and no further surface separation can be reduced, the contact stiffness becomes infinite. Contact stiffness depends not only on the load applied, but also the size, shape and distribution of asperities of the surfaces. Therefore there is no single relationship between interfacial stiffness and contact pressure, which directly related to load. Drinkwater et al. [23] investigated the spring model and found out this model can be applied to ultrasound reflection signals up to frequencies of 50MHz, and they discovered that the relationship between interfacial stiffness and contact pressure can be found for a given pair of surface roughness with a calibration test carried out. The relationship appears to be linear for the first loading on two contacting surfaces under the yield stress, which was found by Hodgson et al. [24].

Ultrasound reflectometry is now frequently used in characterizing machine elements contact. Quinn et al. [25] used ultrasound to investigate the contact patch between a 20mm radius EN24 steel ball from a ball bearing and a flat plate of same material, hardened to 600 H_v mainly using a 25MHz transducer with increasing loads from 0.05kN to 2.15kN applied. A curved line between reflection coefficient and contact pressure was plotted to fit the experimental data acquired and an empirical equation was proposed for the curve:

$$P = 10125e^{-RC} + 3096RC - 6814.8 \tag{3.18}$$

The curve was proved to fit experimental data quite well using chi-square testing. With the calibration curve, contact pressure distributions were plotted from reflection coefficient maps and compared with Herzian theory under 3 loads. Furthermore, a quasi-static spring model was investigated for calculating interfacial stiffness and thus contact pressure from reflection coefficient in more general cases. Applicability of the model was validated using an experimental method under 4 conditions, that is, the transducer frequency was set to be 8MHz and 25MHz and the combined surface roughness was set to be around 0.5-0.7 μm and 1-2.1 μm. The predicted error of the quasi-static spring model was shown to be within 9% in the frequency range from 4MHz to 31MHz, and the surface roughness range from 0.5 μm to 2.1 μm, which covers

the roughness range of common machine elements. An elastic numerical model was also built to acquire interfacial stiffness and compared with that from experimental data, good agreement was found between these two.

Marshall et al. [26] used ultrasound reflectometry to measure contact stresses in machine joints and concentrated contacts, where three contact examples were put forward for investigation: press fitted joints, a bolted joint and a wheel/rail contact pair. The test apparatus consists of an ultrasound pulsar and receiver, an oscilloscope, a PC and a scanning tank. A transducer with central frequency of 10MHz was used for scanning. Two methods were used to reveal the relationship between interfacial stiffness and contact pressure for a certain pair of surface roughness: the first one was to carry out a calibration experiment over a known contact area, calibration specimens of the same roughness as the components under consideration were chosen, and a calibration curve was plotted under a series of loads; the second method was to calculate out the coefficient by dividing nominal total contact pressure against total contact stiffness using the reflected voltage map obtained from experiment. This method is based on the fact that for low pressure cases, the relationship between stiffness and contact pressure is approximately linear. For all three contact pairs, references were taken to eliminate signal attenuation in the material. A line pressure map was plotted for press fitted joints under five different fitting cases; two-dimensional contact pressure maps were plotted for wheel/rail contact with a series of loads from 20kN to 80kN applied; reflected voltage map of scanning over bolted joints with half-apex angle of 41 °was plotted.

The curve was proved to work well for all kinds of metal to metal contact. Yet as it is also pointed out, for two materials with large acoustic impedance difference in contact, normally metal to non-metal contact, amplitude of the reflected signals from interface becomes small so that noise can no longer be ignored. Edge effects which were found in both press fitted joints and bolted joints, and spatial resolution limit of contact pressure maps due to the minimum focal spot diameter limitation were discussed.

In terms of the wheel-rail contact, further tests over a wider range of conditions included were carried out by Marshall et al. [26]. In the paper, three wheel/rail surface conditions: un-used, worn and sand damaged were tested. Calibration tests for different surface conditions were performed and equations were proposed to best fit the calibration results. The *P-K* relationship is approximately linear in the low contact pressure zone: $P=\delta K$, where δ is a dimensioned coefficient and the unit of δ is $10^{-15}m$. The values of δ are 418, 123 and 263 for un-used, worn-thread and sand-damaged cases respectively, one calibration line for sand-damaged case is shown below (Figure 3.9).

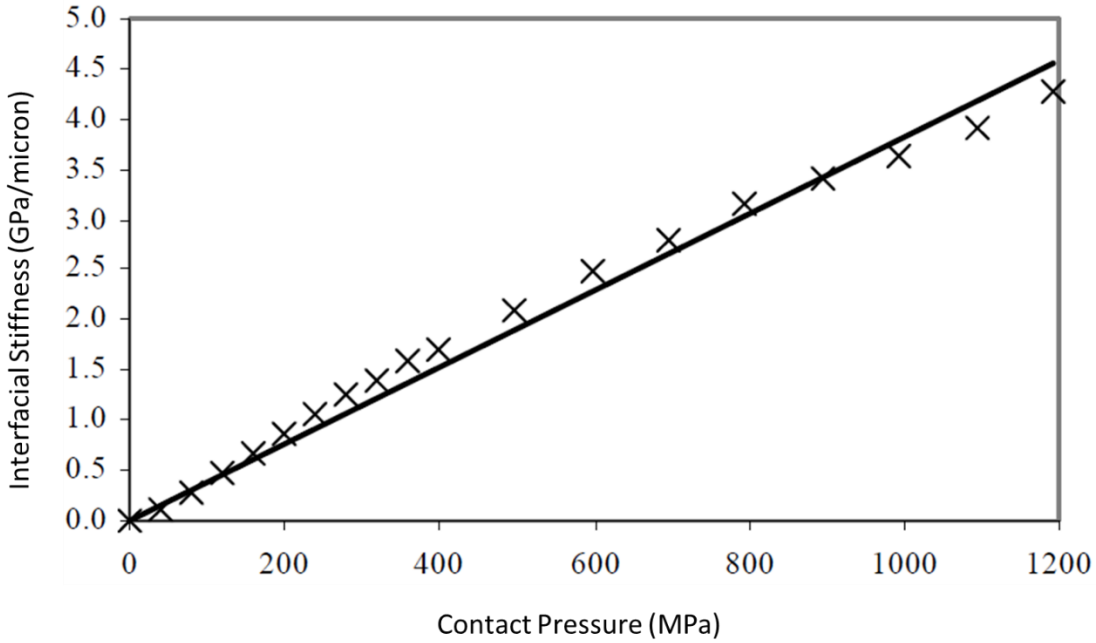

Figure 3.9 Contact Pressure Calibration Curve [26]

It should be noted that the calibration tests were carried out by using two cylinders with surface roughness same as that of wheel and rail specimens respectively, there are also some examples in the literature where calibration tests were carried out with matched combined roughness.

40kN, 60kN and 80kN loads were applied on un-used wheel/rail contact pair and the contact pressure maps are shown in Figure 3.10.

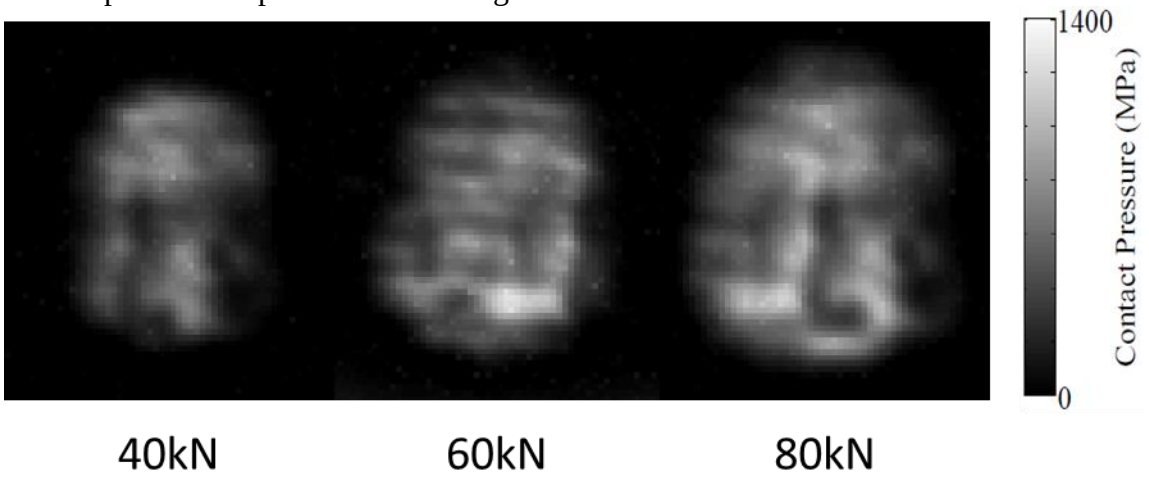

Figure 3.10 Contact Pressure Map from Ultrasound Measurement [26]

The maximum pressures were compared with Hertzian theory as shown in Table 3.1.

Load (kN)	Hertz pressure (MPa)	Maximum measured pressure (MPa)
40	787	1020
60	901	1184
80	992	1296

Table 3.1 Maximum Contact Pressure Comparison with Hertz

Contact pressure maps for three cases under the load of 65kN were compared, big differences were found among these three. The sand-damaged contact patch is more fragmented and the contact spread compared with the un-used case, peak contact pressure being slightly lower; the worn thread contact patch appears to be more circular and the real contact area becomes larger than un-used one in global scale, but locally the contact is fragmented which leads to higher peak contact pressure. A double contact was found in the worn wheel/rail contact with one on the thread and the other on the flange. The double contact patch shows good agreement with the Finite Element simulations by Telliskivi and Olofsson [17] (see Figure 3.8).

Similar research into wheel/rail contact using ultrasound reflectometry was done by Pau [27], ultrasonic focusing probes with different frequencies were used on a series of wheel-rail contacts with different roughness pair to discover portion of the real contact area (RCA) in the nominal contact are. Decreasing real/nominal contact area ratio was found as the surface roughness went up, as it can be seen in Figure 3.11.

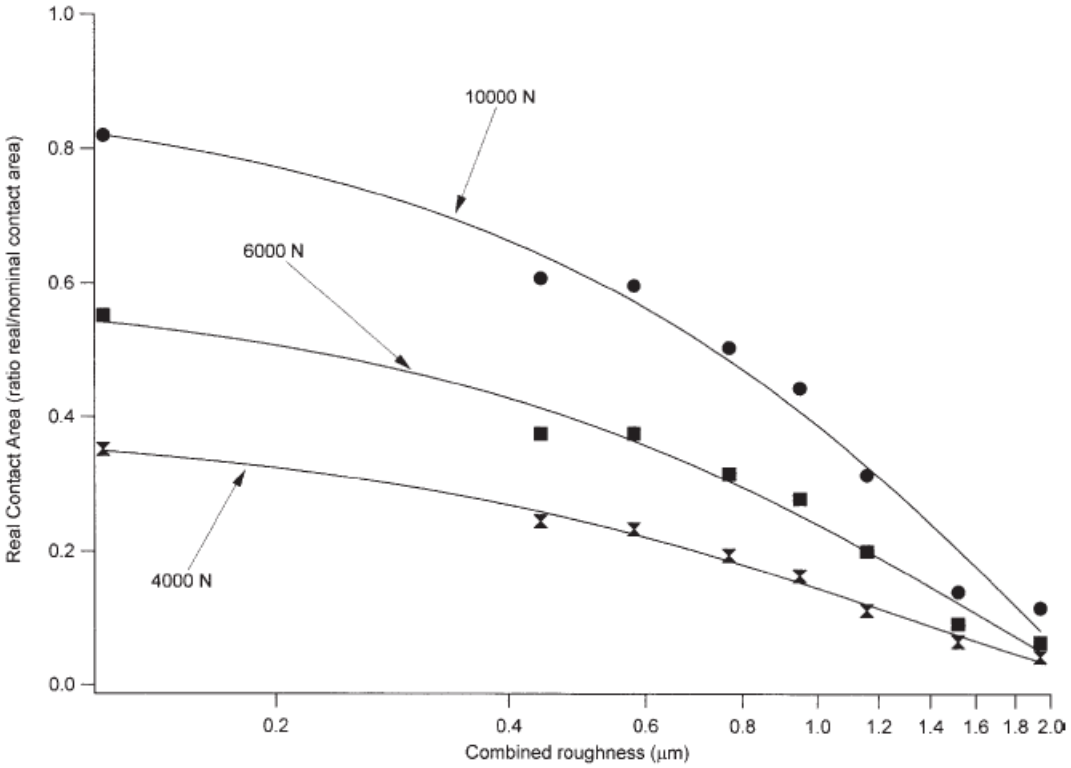

Figure 3.11 Variation of the Real/Nominal Contact Area Ratio vs Combined Roughness for Three Levels of Load [27]

3.5 Summary

In this Chapter, the development of contact mechanics are discussed. Theories for solving contact problems including Hertz, CONTACT and FASTSIM etc. are introduced. Previous research work on characterizing the wheel-rail contact using finite element method and ultrasound has been talked about. Results were compared with classic Hertz and CONTACT methods. The contact patches as well as contact pressures match well with theoretical predictions in terms of wheel tread-rail head contact, but

are rather different for flange contact. Due to the complexity of dynamic contact characterization, most research are focused on static contacts. Therefore, it is of great novelty to develop a real-time measuring technique for characterising dynamic contacts.

Chapter 4:

Ultrasound Principles

4.1 Introduction

In this chapter transmission and propagation of an ultrasonic signal through materials are described. Structures and properties of materials that influence the transmission are discussed. The principles of ultrasound reflectometry at contact interfaces are dissertated and the concepts of the spring model and interfacial stiffness are introduced. Through these principles, it is possible to use ultrasound as a measurement tool for analysing machine element contacts.

4.2 Ultrasound Transmission

Sound waves are mechanical vibrations of particles of a propagating host media. Generally a host medium can be regarded as many small particles bonded together with elastic springs. This model can explain propagation of sound waves in materials although it is a simplified one. When a wave is excited, particles on one side are vibrated and elastic forces are transmitted through these springs so that particles on the other side start vibrating as well. In this way sound waves pass through the host medium.

If the bonds between particles are rigid, any mechanical movements will be transmitted from one end to the other end instantly, and the whole medium will oscillate simultaneously. In elastic models, mechanical vibrations from one particle to a neighbouring one needs time, which results in a phase shift between two particles along the wave transmitting direction.

Different types of sound waves can be propagated in elastic host media, such as transverse waves and longitudinal waves. Transverse waves indicate that the oscillating direction of vibrating particles is perpendicular to the transmitting direction of the wave, and longitudinal waves refer to oscillating direction being parallel to transmitting direction. In this study longitudinal ultrasound waves are used. Therefore, materials are divided into extension and compression zones of particles as sound waves pass through, as shown in Figure 4.1.

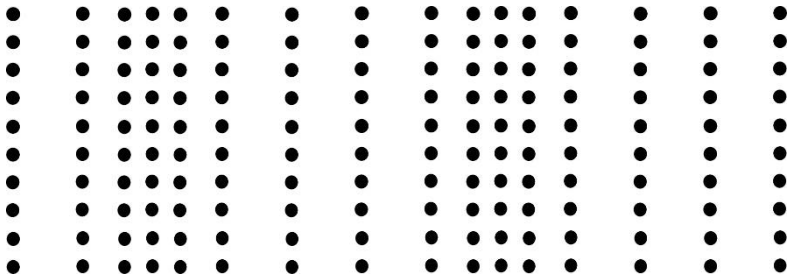

Figure 4.1. Propagation of a Longitudinal Sound Wave through an elastic media

4.3 Material Properties

4.3.1 Speed of Sound

The rate at which the waves travel through a material is determined by the elasticity of the material. Therefore speed of sound is different in different materials. And there is a relationship below:

$$c = f\lambda \tag{4.1}$$

where c is the speed of sound; f is the frequency and λ is the wave length.

4.3.2 Acoustic Impedance

Acoustic impedance is a parameter that describes the resistance of a material to sound waves and determines the behaviour of a wave that is reflected at the interface. It is given by the relationship below:

$$z = \rho c \tag{4.2}$$

where z is the acoustic impedance; ρ is the density of material and c is the speed of sound.

4.3.3 Attenuation

As the ultrasonic signals propagates in the media, the signal strength will reduce gradually, which is noted as attenuation. Absorption and scattering are two factors of the ultrasound attenuation.

As it was introduced in Section 4.2, ultrasonic signals can be propagated in materials due to mechanical vibrations of elastic bonds between particles. Theoretically if only elastic forces are considered, the ultrasonic signals are fully transmitted through the materials and no energy is lost. But in real cases, resistive friction exists when particles

vibrates. Part of the mechanical energy is transferred to heat in the process of overcoming friction. In this way the ultrasonic signals are absorbed by the medium and the strength is reduced. The absorption is not only determined by inner properties of materials but also by the frequencies of ultrasonic signals. For a given material, the absorption tends to increase as the frequency goes up. This is because with higher frequencies, the particles vibrate faster, which leads to a growth of friction and heat conversion.

The scattering is caused by diffuse reflection of sound waves at interfaces. The interfaces not only refer to boundaries between different materials but also those inside the materials. Due to inhomogeneity of material structures which the ultrasonic signals are travelling through, the speed of sound as well as the density can change in these regions. Inhomogeneities in the material structure come from voids and inclusions in the material bulks or grains boundaries in the crystalline structure of materials. Once the ultrasound waves strike boundaries of voids or grains, the signals will be partially reflected and partially refracted, resulting a loss of signal strength. The scattering effect caused by voids and inclusions is largely related to the size and orientation. But generally the larger the void or inclusion is compared to ultrasonic wave length, the greater the signals will be scattered. This also applies to the grains, when the size of the grains is less than 1 percent of wavelength, no signal is scattered. However, when the size grows to about same as wavelength, most signals will be scattered. Higher frequency means shorter wavelength for a given material, so the scattering also grows as frequency increases. Therefore the total attenuation increases with frequency.

Energy loss in absorption can be compensated for by enhancing the strength of original signals, but this is not applicable for solving the problem of scattering. As the scattered signals will remain propagating in the material bulks, many small sound waves are generated. These waves become background noise of the material which is proportional to the original signal. If the energy of the original signal increases, the magnitude of noise also rises up.

4.4 Huygens Principle

When a beam of ultrasound signals is pulsed from a transducer, the ultrasonic beam is actually formed from interaction of a number of elementary waves. These elementary waves are emitted from several regularly arrange nodes, which act as point resource. The Huygens Principle indicates that for each individual point resource, a wave is emitted and spread away spatially isotropic as a sphere [28]. A 2D schematic image is shown in Figure 4.2 explaining the ultrasonic wave propagation principle, the front face is divided into 10 nodes with equal spacing. The 10 spherical wave fronts form a line and propagates from bottom to top. The more nodes a transducer contains, the closer the wave fronts form like a straight line. The 3D situation is a similar case, the nodes

are distributed in a plane and the wave front form a planar ultrasonic wave. The wave front can again be divided as a number of point source and this process is repeated. The wave is propagated in this way.

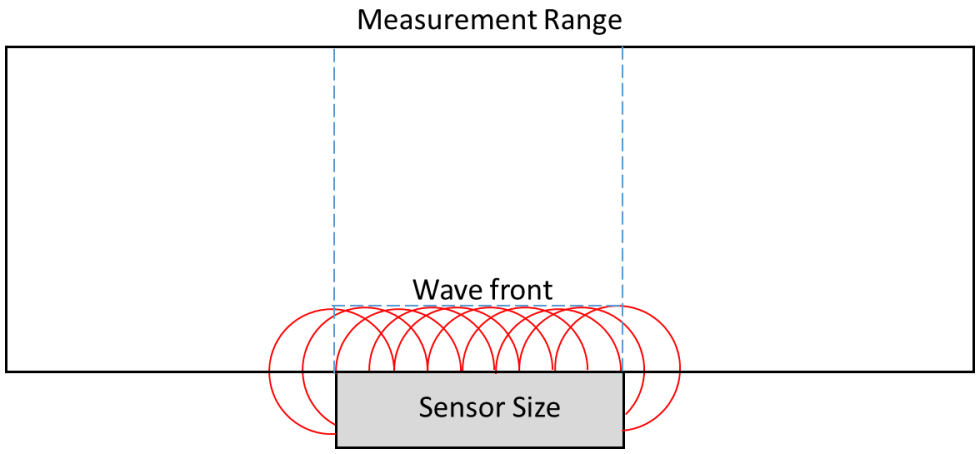

Figure 4.2 Schematic of the Ultrasonic Wave Propagation

From Figure 4.2 it can also be seen that for nodes near the edge of the sensor, the waves emitted are dissipated outward and some of the signals reflected from the place outside the measurement range will not be received by the transducer.

4.5 Ultrasound for Contact Measurements

4.5.1 Ultrasound Reflection from Rough Surfaces

All manufactured surfaces have a roughness. On the surface there are tiny peaks which are known as asperities. When two bodies are in contact with each other, it is those asperities that are pressed together. Therefore, the actual contact area is far smaller than the nominal contact area. As ultrasonic waves move smoothly in dense material (steel) and not that well in less dense material (for example, air), the majority of the ultrasonic signals will be reflected back at the steel-air interface and fully transmitted at steel-steel interface (as shown in Figure 4.3) [22].

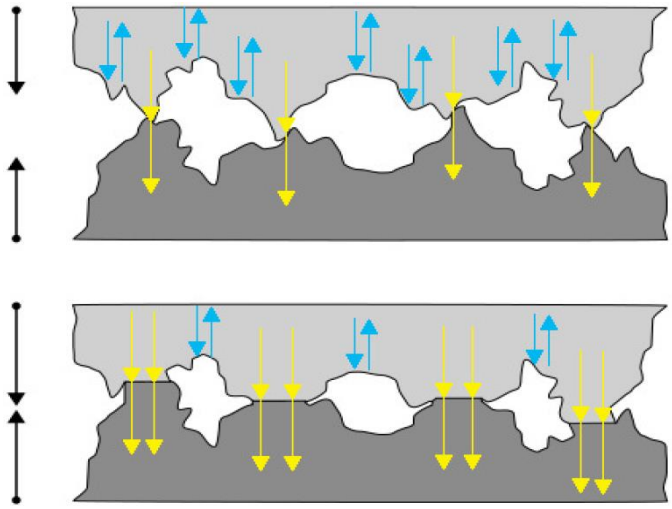

Figure 4.3 Schematic Image of Ultrasonic Signals Behaviour at Different Interface

It can be seen that as the compressing force increases, the contacting asperities start deforming which leads to a larger actual contact area and a greater portion of transmitted ultrasonic signals and smaller reflected signals. Thus it provides the possibility to look into contact situations between two solids by monitoring the reflected signals. Hereby a reflection coefficient *R* is introduced.

Drinkwater et al. investigated the *spring* model and its applicability to ultrasonic reflection data from a rough surface interface [23]. If the ultrasonic wavelength is relatively long compared with length of air gaps, then the interface can be regarded as a distributed spring. Kendall & Tabor discovered that the reflection is dependent upon the spring behaviour of the interface and the reflection coefficient could be defined by following relationship [21]:

$$R = \frac{\sqrt{(\omega z_1 z_2)^2 + K^2(z_1 - z_2)^2}}{\sqrt{(\omega z_1 z_2)^2 + K^2(z_1 + z_2)^2}} \tag{4.3}$$

where $\omega = 2\pi f$ is the angular frequency of the ultrasound, z_1 and z_2 are acoustic impedance of the two contacting materials respectively, *K* (GPa/μm) is the interfacial stiffness which increases as the applied load increases.

If z_2 is comparatively small and the $(\omega z_1 z_2)^2$ part is much smaller than $K^2(z_1 - z_2)^2$ and $K^2(z_1 + z_2)^2$, then the relationship reduces to $R = \frac{z_1 - z_2}{z_1 + z_2}$. If two contacting bodies are made of same or rather similar material, then it can be simplified as:

$$R = \frac{1}{\sqrt{1 + (2K/\omega z)^2}} \tag{4.4}$$

Because the materials of wheel and rail or bolted joints are all steel, material properties are basically the same or very similar, Equation 4.4 is generally used in wheel-rail contact and bolted joints scanning [29] for contact stiffness calculation.

4.5.2 Stiffness of Contact Interfaces

The contact stiffness *K* comes from the spring model of contact surfaces. It is a parameter describing the force required to push the contacting interfaces closer. Some asperities start deforming as two bodies come into contact. When the surfaces are further compressed together, more asperities are in contact, thus larger force is needed for further compression. The contact stiffness can vary non-linearly from zero when there is no contact to infinity when two surfaces are fully pressed together. It is defined as differential of nominal contact pressure against approach of the mean lines of the surfaces by Thomas & Sayles [30]:

$$K = -\frac{dp_{nom}}{du} \tag{4.5}$$

where *u* is the separation of the mean lines of roughness of the two surfaces. Figure 4.4 shows machined surfaces in contact and the spring model of contact interfaces.

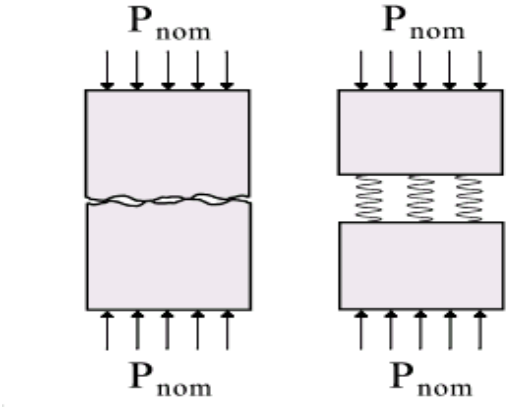

Figure 4.4 Spring Model of Contact Surfaces

The contact stiffness in reality is not only determined by contact pressure, but also by number, size and height distribution of asperities of the contact surfaces.

4.6 Validation of the Spring Model

The interfacial stiffness *K*, as defined in Equation (4.5), is independent of frequency of the ultrasound, *f*. Drinkwater et al. [23] carried out a series of experiments to validation the applicability of the spring model. Figure 4.4 shows the reflection coefficient

changes with different frequencies and a range of loads to control the variation of stiffness. It can be seen from Figure 4.5 that the reflection coefficient increases as the frequency increases, which match the prediction from Equation (4.3).

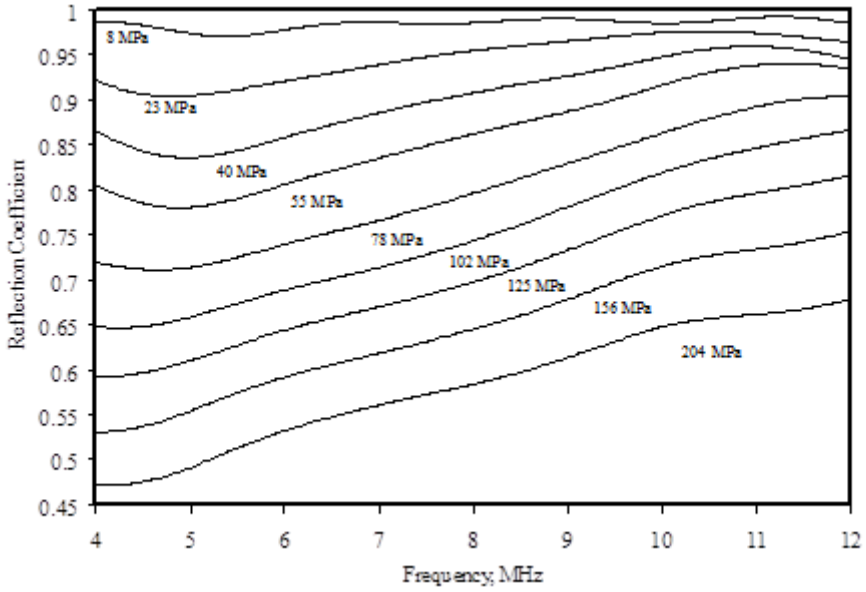

Figure 4.5 Plot of Reflection Coefficient Changes with Frequency and Interfacial Stiffness [23]

Further the values of the interfacial stiffness can be calculated from Equation (4.3) given the reflection coefficient and frequency data above. Another plot between interfacial stiffness and frequency can be seen in Figure 4.6.

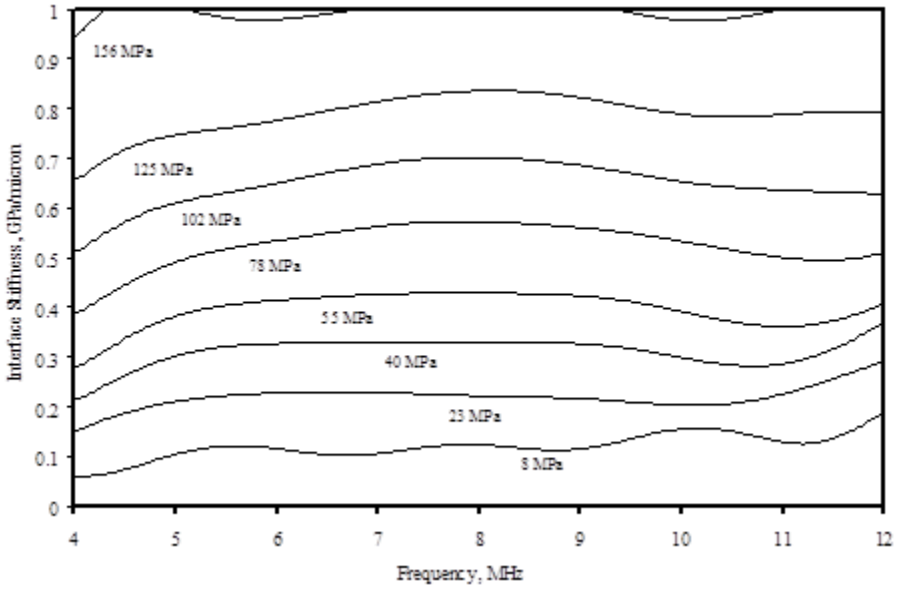

Figure 4.6 Plot of Interfacial Stiffness against Frequency [23]

As it can be seen in Figure 4.5, for frequencies varying from 4MHz to 12MHz under all range of contact pressures, the interfacial stiffness appears to be a flat line. This matches with the prediction that stiffness is independent of frequency and proves the applicability of the spring model. Drinkwater also stated that the model can be applied to measurements with ultrasonic frequencies up to 30MHz.

From Figure 4.5 and Figure 4.6 it can be concluded that measurements of reflection coefficient are influenced by the frequency of ultrasound signals, and the interfacial stiffness is independent of the frequency.

The interfacial stiffness is determined not only by the load but also by the shape and size of the asperities as well as the distribution of them. So for two contact pairs with different roughness, the interfacial stiffness can be largely different even under a same load. Hodgson et al. [24] found that for a given rough contact pair and low contact pressure, the relationship between interfacial stiffness and contact pressure is approximately linear. Therefore a calibration test is needed to obtain the proportion coefficient for measured contacts. The calibration test will be discussed in section 5.6.

4.7 Summary

In this chapter, the principles of ultrasound are described. Transmission and attenuation of ultrasound signals through materials are introduced respectively. The Huygens Principle which explains the construction and propagation of ultrasound waves is presented. The propagation of ultrasound is largely affected by the properties of transmitting media. Principles of using ultrasound reflectometry for measuring contact are also presented. The spring model together with the definition of interfacial stiffness is introduced. Validation of the model is also reviewed.

Chapter 5:

Ultrasound Methodology

5.1 Introduction

Principally contact characterization is based on the division of a reflected ultrasound signal from a contact interface by the incident signal. The reflection coefficient varies from 0 to 1 which represents full contact and no contact respectively, lower reflection coefficient indicates larger deformation of asperities and better contact. There are several points which affect the ultrasound signal. The first thing is the angle between transducer and the object interface. Ideally the interface needs to be perfectly perpendicular to the pathway of ultrasound beams to avoid scattering of the signals, the flatter the interface is, the less the ultrasonic signals will be scattered and a clearer reflected signal will be obtained. However, in real cases, for example, ball bearing contacts and a wheel-rail contact, no flat interface is expected; secondly, signals will inevitably be absorbed by materials and attenuated when passing through contacting bodies. Basically the higher the frequency of ultrasound is, the more of the signal will be absorbed; thirdly, the ultrasound beam has to be focused exactly on the interface, normally the focal length of ultrasound signal is longer than the thickness of test objectives, thus couplant is needed. Currently two kinds of couplant gel and deionized water are commonly used.

5.2 Ultrasonic Transducer

5.2.1 Ultrasonic Focusing Transducers

For ultrasonic measurements tests, longitudinal ultrasound waves are typically chosen. Ultrasonic signals of this type are usually excited by an ultrasonic transducer. The transducer contains an active piezo-electric plate. In response to an electric excitation, an ultrasonic pulse is generated from the plate. The speed of the ultrasound signal is basically same as that of normal sound, for example, 340m/s in the air, 1440m/s in the water and about 5400m/s in steel.

Figure 5.1 shows a schematic structure of an ultrasonic transducer, the piezo-electric plate lies in between two layer of electrodes, and is constrained in an attenuative damping medium and a wear plate at the bottom.

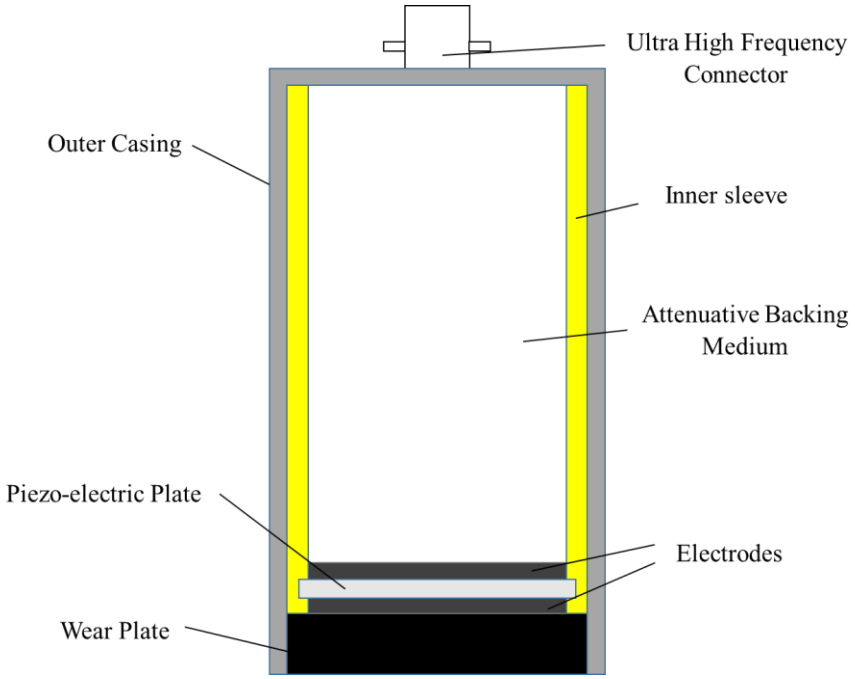

Figure 5.1. Schematic Diagram of an Ultrasonic Transducer

Due to the properties of piezo-electric materials, the ultrasonic signal emitted from the plate usually contains a range of frequencies. It can be seen from the signal displayed in the frequency domain, that different frequencies contain varied energy, the frequency with maximum energy is called centre-frequency. The energy monotonically decreases as the frequency difference increases from the centre frequency. The term bandwidth is introduced to pick up useful frequencies which contain at least 50% of that of the centre frequency, as shown in Figure 5.2.

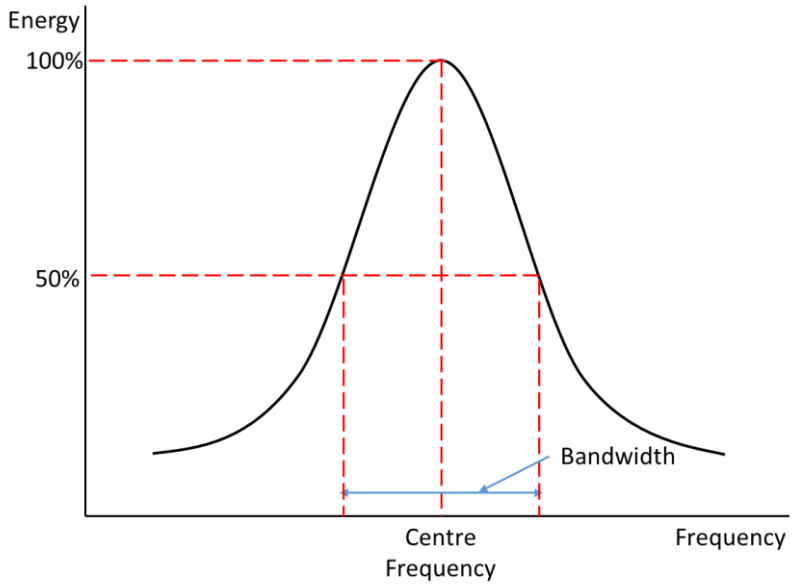

Figure 5.2 Energy Distribution of Ultrasonic Transducer with respect to Frequency

5.2.2 Ultrasonic signal focusing and coupling

As previously stated, for a certain type of material, the higher the frequency, the smaller the wavelength is. Normally the frequency used for ultrasonic measurements are in the scale of MHz. The wavelength can thus be so small that the size of particles in the host medium is relatively large. Attenuation is severe, especially when there are fast moving particles, as the pressure wave that constitutes the ultrasonic signal is interrupted by the moving particles. No air is allowed in the way that ultrasound travels as the molecules of gas move much faster than that of liquid or solid. Therefore a couplant is needed between an ultrasonic transducer and a test specimen.

Every transducer has a known focal length in water, as shown in Figure 5.4a. However, when the transducer moves over a specimen, the ultrasonic signal behaves similar as light, the wave partially reflects and partially refracts as it enters the object, leading to a change of focal length. The refraction of the signal follows the Snell's law and is determined by equation 5.1:

$$\frac{\sin\theta_1}{\sin\theta_2} = \frac{c_1}{c_2} \tag{5.1}$$

where θ_1 and θ_2 are incident and refraction angles, and c_1 and c_2 are speeds of sound of the material above and below the boundary respectively (as shown in Figure 5.3). During the test, the thickness of the top specimen is measured, and the refraction angle can be calculated from Equation 5.1, the water path length needed for focusing the signal onto objective interface can be derived. Then the transducer is adjusted to certain height as shown in Figure 5.4c

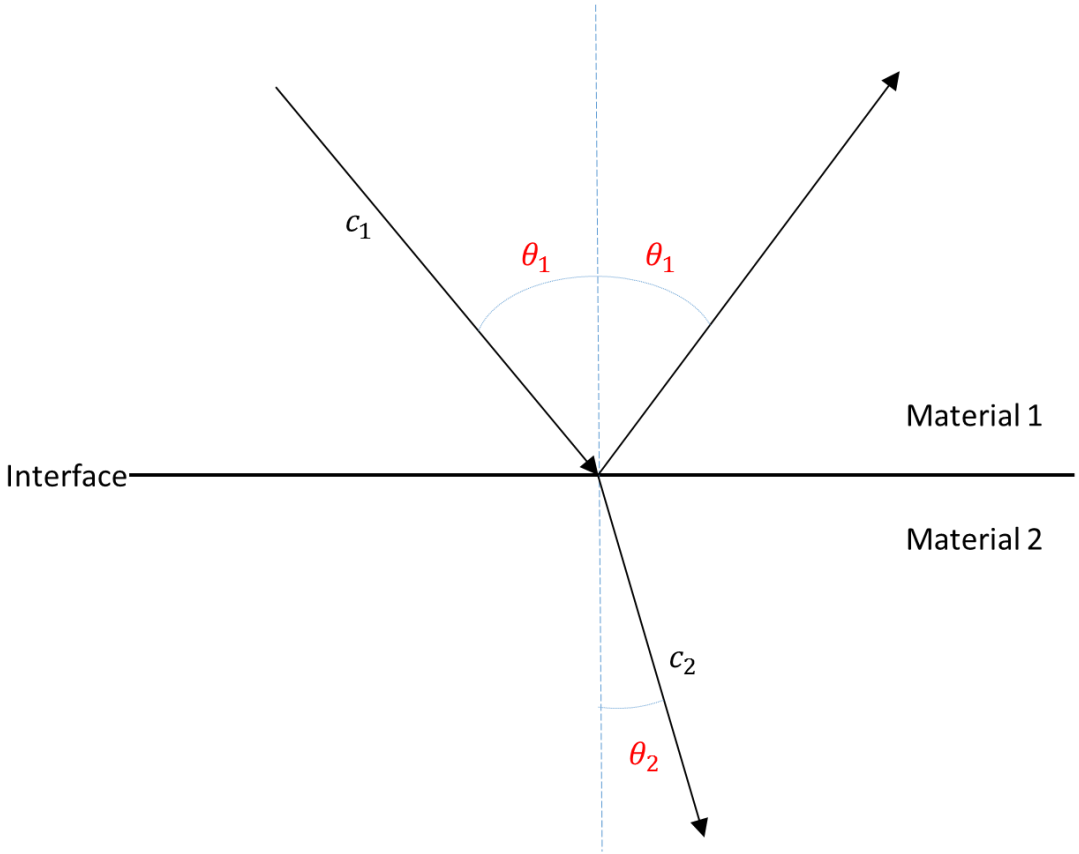

Figure 5.3 Reflection and Refraction of an Ultrasound Beam at the Interface

Normally there are several types of couplant for different test conditions: solid rubber, viscous grease and water. As mentioned above, a focusing transducer has a focal length. Ultrasonic signals need to be focused exactly at the target interface. In this case water is used so that the transducer can move freely to adjust height between transducer and object of interest (Figure 5.4). The water couplant also allows a 2-dimensional scanning measurement to be carried out by moving the transducer horizontally; as with measurements using an array, because the array is normally attached onto the test specimen, in this case viscous grease or honey is used as the couplant but the magnitude of the signal will be affected due to change of couplant thickness. This is particularly obvious with normal load applied; solid rubber as a couplant does not have this problem, but will lead to severe attenuation of signals and thus can only be used when signal noise ratio is high enough so that large attenuation is acceptable.

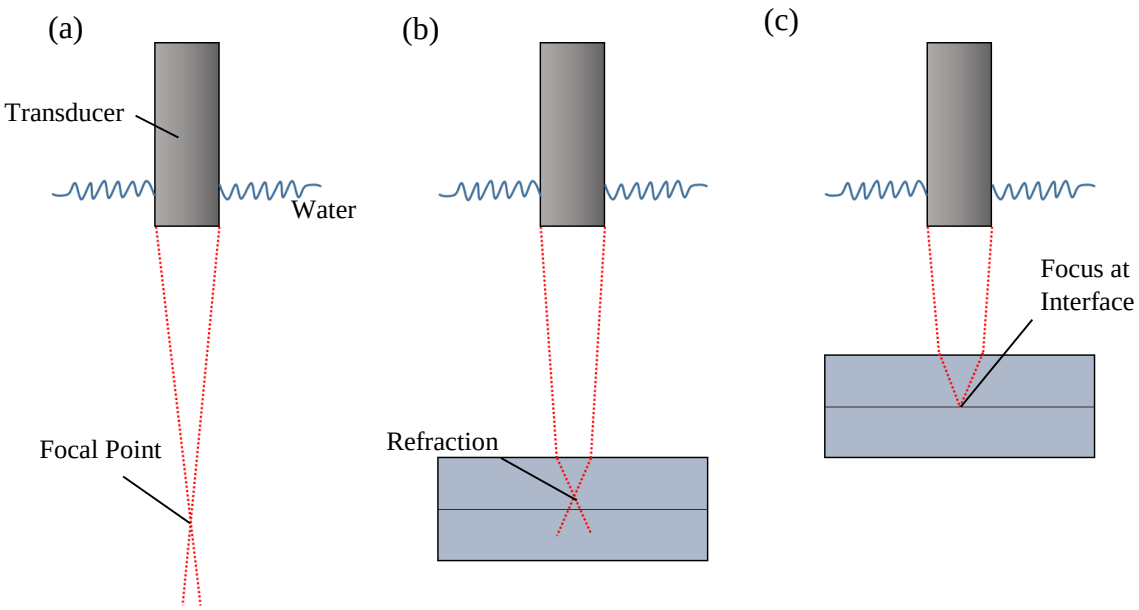

Figure 5.4 Transducer Focusing (a) Focal Length in Water; (b) Refraction at a Boundary; (c) Focusing at the Interface.

5.2.3 Ultrasonic Scanning Array

For the dynamic test developed in this work, a 64-element ultrasound array (Figure 5.5a) together with a multiplexor (Figure 5.5b) was used. An ultrasonic pulsar is integrated in PC which can pulse 8 beams of ultrasound at one time, this means only 8 elements (one channel) of the array are scanning one time. The multiplexor is therefore used for switching channels (Figure 5.5c). Once the switching speed is enough fast compared with related velocity between contacting particles of two bodies, it can be regarded that the array is pulsing 64 elements at one time. The array is normally placed on a flat plane which should be parallel to the objective interface, so that the reflected signals can be to the largest extent received. Pulse rate of the array is normally 10kHz and can be higher. It should be noted that because the array is working by switching channels, and the sampling rate is enough for measuring dynamic wheel-rail contacts with current experimental rolling speed or even far higher rolling speed. It is the switching speed that limits the quality of results.

(a) (b)

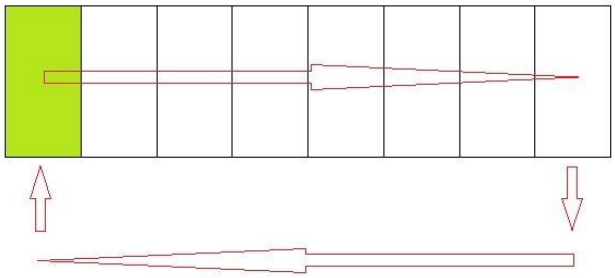

(c)

Figure 5.5 (a) Ultrasonic Array; (b) Multiplexor; (c) Switching Cycle

Unlike the focusing transducer used for static scanning tests, the scanning array pulses signals divergently. As shown in Figure 5.6, each element pulses a beam of ultrasonic signals radiantly. The reflected signals from the interface either dissipate outside the scanning area or are received by the elements. Because of this radiance pulsing mechanism, reflected signals received contain information of averages of a line rather than a spot. And therefore the array is scanning an area larger than the physical size of the array itself. However, the final pressure distribution is plotted according to the array length, causing the contact patch detected will be slightly larger than actual one. In terms of the array, liquid grease or solid rubber is commonly used as couplant. The solid couplant is placed between the array and the specimen, which can be regarded as an extra contact layer, and signals are attenuated passing through the couplant. Besides, there are air gaps between the couplant and the specimen as well as the couplant and the array, and this leads to further attenuation. The liquid grease does not have this problem, but the issue is that the thickness of the couplant cannot be kept even throughout the contact area between the array and specimen. This leads to difficulty in capturing reflected signals near a fixed time delay.

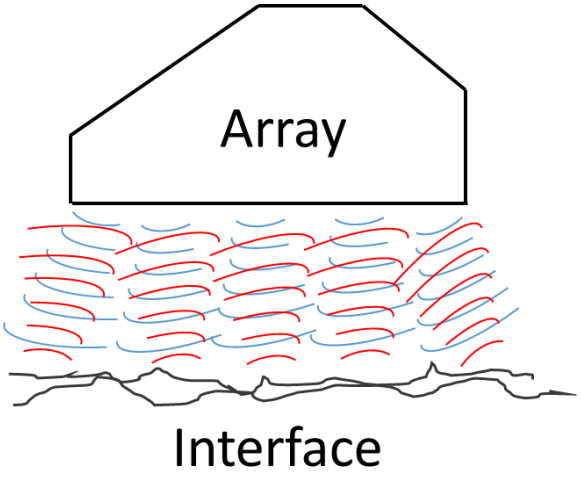

Figure 5.6 Ultrasonic Array Scanning

5.3 Static Measurements Method

5.3.1 Test Set-up

The basic set-up consists of a scanning tank, an oscilloscope, an ultrasound pulsar and receiver (UPR) and a computer, as shown in Figure 5.7. The UPR pulses constantly, which means that the transducer emits and receives ultrasonic signals steadily. The pulsing rate is controlled by programs in the PC. The UPR is connected to the oscilloscope so that both emitted and reflected signals can be displayed. The signals are recorded and processed in the PC. With software and hardware upgraded, the UPR and the oscilloscope are both integrated into the PC.

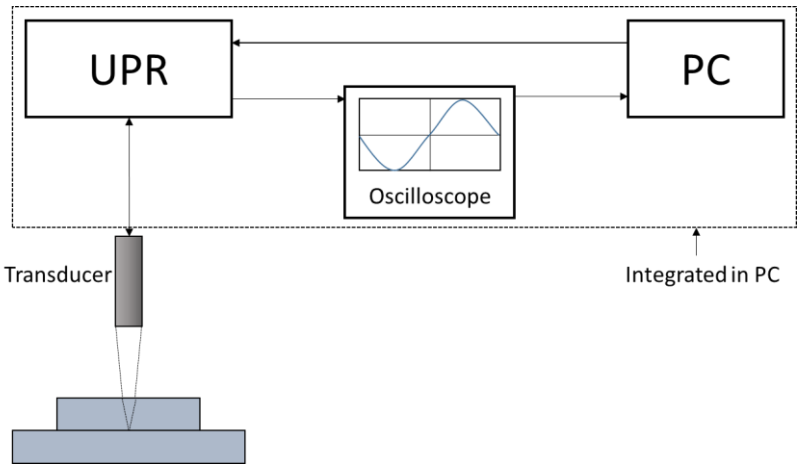

Figure 5.7 Test Set-up for ultrasonic measurements of an interface

The ultrasound scanning measurements for a static contact are carried out using scanning equipment. Figure 5.8 shows schematic structure of a scanning tank. The scanning tank allows the ultrasonic transducer to move in three directions, x and y movements are automatically driven so that the transducer is able to scan over an area; z direction represents height and can be manually adjusted so that the transducer can focus exactly on the contact interface. During the tests, the specimens are placed on the bed of the tank right under the scanning probe. A water bath is mounted above the specimen for focusing signals.

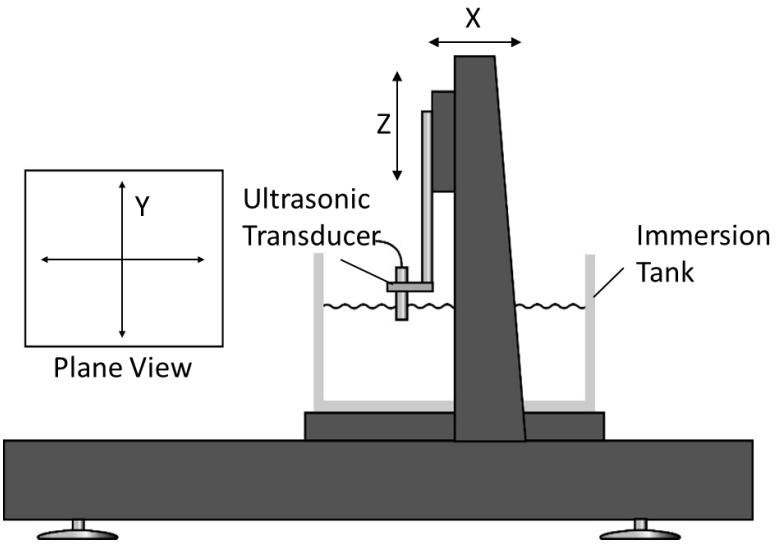

Figure 5.8 Schematic Image of Scanning Tank

Two loading frames are used for different tests. A stainless steel loading frame is used for high load test purposes (wheel-rail, steel ball-on-flat). A hydraulic actuator is used for applying vertical load, and a series of reflected voltage maps under different loads can be acquired. Since the hydraulic actuator is designed for applying instantaneous load, but not for maintaining load, a valve is attached onto the actuator as shown in Figure 5.8.

Figure 5.8 Loading Frame for High Load Test

Another smaller loading frame (shown in Figure 5.9) is used for low load cases. Three built-in springs are used for load application, and a lifting mechanism is used to compress the springs. The springs are pre-calibrated by loading-up with known masses and measuring the compression with callipers.

Figure 5.9 Loading Frame for Low Load Test

When carrying out tests, the transducer is sunk in the water couplant and signals are pulsed in the z direction. As mentioned in section 5.2, each focusing transducer has a focal length. The focal length changes when signals pass through another material. By measuring the depth of water couplant and thickness of the contact body, the new focal

length can be calculated through Equation 5.1. The probe is then mounted around the optimum height according to the calculation result. The height can be micro-adjusted in the z direction for the best signal reflection. The original signal and all the reflected signals are displayed in the oscilloscope according to time latency. It can be seen that the reflected signal from the water-steel interface as well as multi-bounce signals are all shown on an oscilloscope. By amplifying and extracting information (normally peak-to-peak value) from received signals, experimental data can be recorded in digital format in a PC. During the scanning process, the transducer moves in the x and y directions and consequently a 2-D reflected voltage map from the contact interface can be plotted over the x-y plane, as shown in Figure 5.10a. The scanning tank has a range of 500mm, and has an optimum resolution of 0.025mm along the x axis; the resolution along the y axis depends on the pulsing frequency of the UPR.

It should be noted that the PC scans and records data once every time the transducer keeps still before moving to the next position, leading to a consecutive line of measurements. The data are then arranged according to their x and y coordinates and plotted as a map. Each individual data acts as a pixel of the plot, and each single pixel is the same size as the focusing spot. The resolution mentioned above marks the distance between the centres of two neighbouring pixels. Therefore, if the size of the resolution is larger than the diameter of the focusing spot, there will be overlaps between two rows or columns of measurements; otherwise there will be gaps. Although both situations cannot ideally reveal the actual contact, it is principally thought to get higher resolution for more information and a smoother plot. This in turn increase the scanning time of a single measurement.

Due to focus spot size limitation, outcome resolution is restricted. Incident signals information can be acquired by scanning over the same area on the surface of the test objective without contact, where all ultrasound signals are reflected, these reflected signals can be regarded as incident signals (Figure 5.10b). By carrying out reference experiments, signal attenuation and influence from the profile of the test object will be eliminated. Finally, through dividing the 2-D reflected voltage map by incident voltage map, a reflection coefficient map can be obtained (Figure 5.10c).

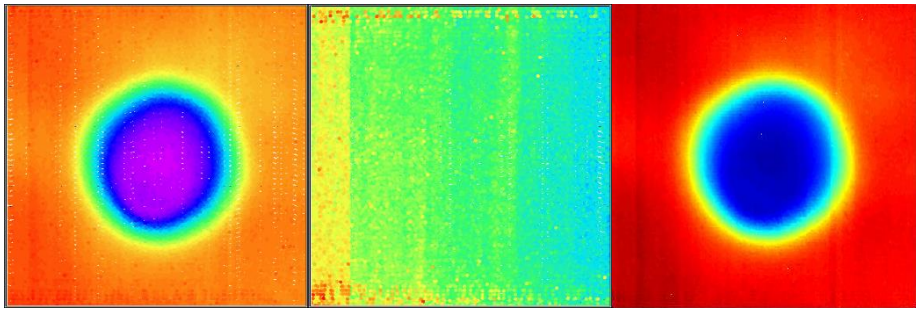

(a) (b) (c)

Figure 5.10 (a) Reflected Voltage Map; (b) Reference Voltage Map; (c) Reflection Coefficient Map

5.4 Quasi-Static Measuring Method

The method described in this section is noted as 'Quasi-Static' because the measurements were taken over static contacts, and a series of static measurements were taken in different positions using the ultrasonic array, the 2-D plot of the contact area is in the same format as for dynamic measurements. This method was mainly used as a pilot study for dynamic tests. The array is normally mounted on one contact body with the pulsing face parallel to the contact interface so that the reflected signals can be to the largest extent received. When taking measurements, the array starts pulsing towards the contact interface and receives reflected signals while one contacting body moves over the other. For a flat contact, when no contact is detected, the emitted signals from the array are almost 100% reflected back at the interface; as the body moves into the array scanning zone, signals at the interface are transmitted through the contacting asperities, resulting a drop of the amplitude of reflected signals. Since the array pulses signals continually, a 2-D image of reflected voltages against time can be plotted consequently. Drops of reflected signal strength also occur when the contact interface is curved. A reference measurement is used to eliminate influence from profiles. The reference can be acquired by carrying out another test without contact under the same conditions or directly using scanning data from the non-contact region.

A pilot study using the array has been undertaken by carrying out a quasi-static wheel/rail contact test. The optimum position to mount the array has been simulated using finite element software and a hole was machined in the rail for placing the array. The rail was moved manually under the wheel, separate measurements were taken at different positions, resulting in a 2-D map showing the contact patch, which is shown in Figure 5.12 [31]. The rail was moved over 20 spots with same distance between neighbouring two spots, a full cycle of 64 element measurements were taken (in Figure 5.12, 2 channels of elements measuring out of contact area were taken away for ease of viewing, therefore there are only 48 columns in the figure). The test rig is shown in Figure 5.11.

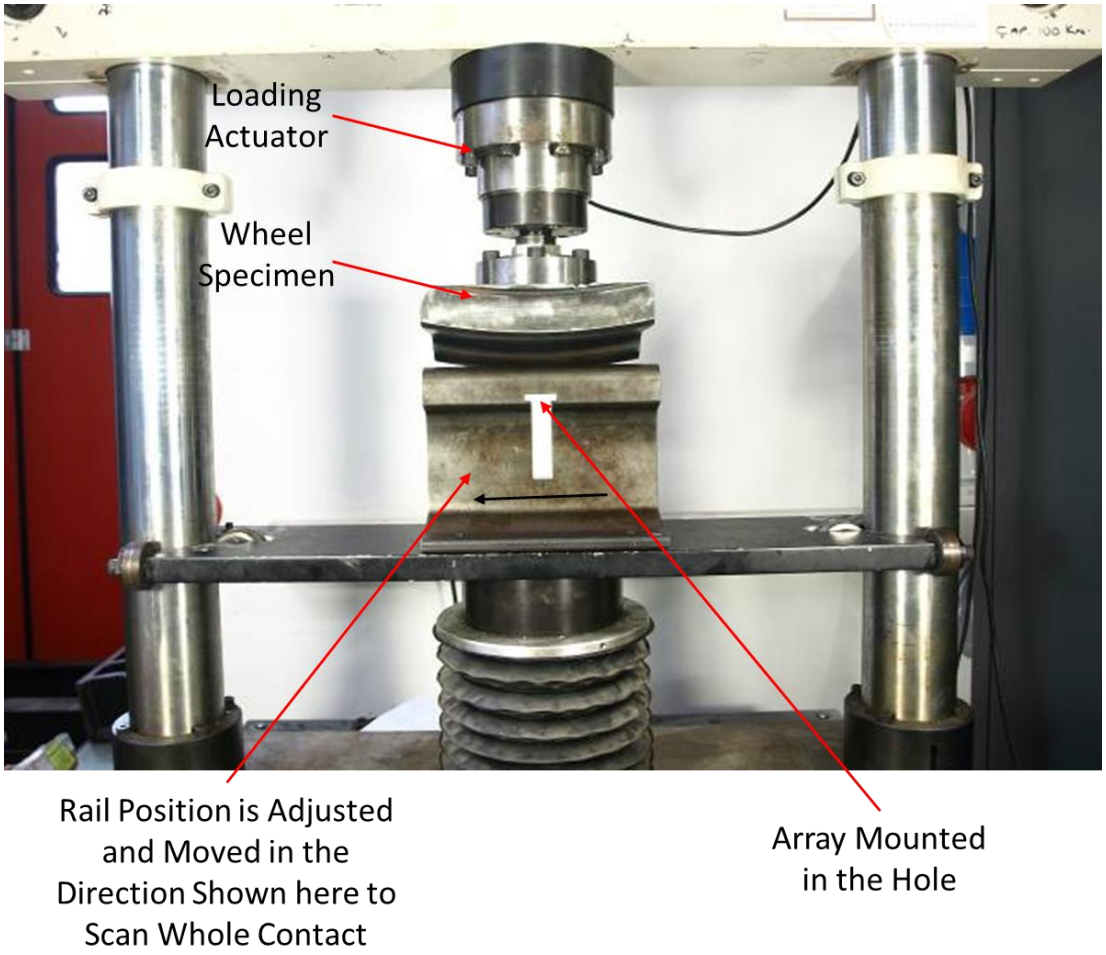

Figure 5.11 Wheel and Rail Section Mounted In Static Loading Frame Showing the Section Removed from the Rail [31]

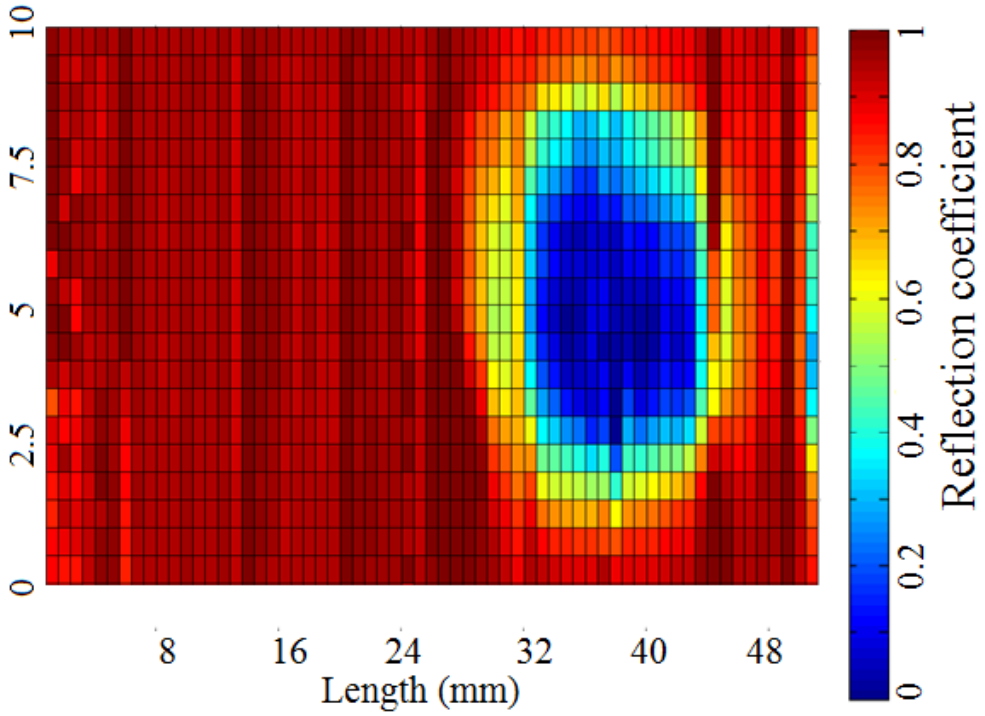

Figure 5.12 2-D Reflection Coefficient Map of Contact [31]

5.5 Dynamic Measuring Method

The dynamic test is basically similar to the quasi-dynamic one in terms of wheel-rail contact. Normally the array should be located on the static contact body for steady measurements, but there are exceptions according to actual situations. As the contact conditions of machine elements other than wheel and rail vary from each other, the array mounting may adjust to specific test set-up. In some cases, the array can be mounted on the moving bodies. But in all situations one principle should be followed, which is the surface for mounting the array must be flat and fully fitting the array, and the scanned contact patch should be to the largest extend perpendicular to the pulsed ultrasound signals.

5.6 Calibration Test

During the actual scanning test, reflection coefficient can be derived from the original signals and reflected signals. Thus interfacial stiffness is acquired. Yet stiffness is not simply dependent on contact pressure, it also depends on the number, size and distribution of asperities on contact surfaces. But for a given contact pair with certain roughness, the relationship between stiffness and contact pressure is fixed. Therefore, a calibration test is always essential. The calibration test uses two contact specimens of the same material and of the same surface roughness. A given load is applied to a known contact area, a linear relationship between interfacial stiffness and contact pressure could be determined. The calibration test shown in Figure 5.13 is carried out in a loading frame; the load is applied with a hydraulic jack.

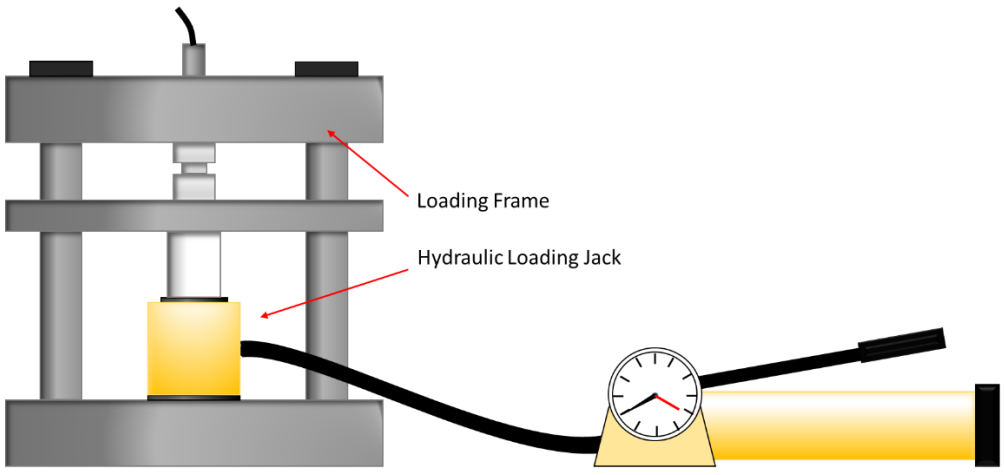

Figure 5.13. Diagram of the calibration specimens and loading equipment

An example loading relationship for two polished EN24 steel specimens can be seen in Figure 5.14 [26].

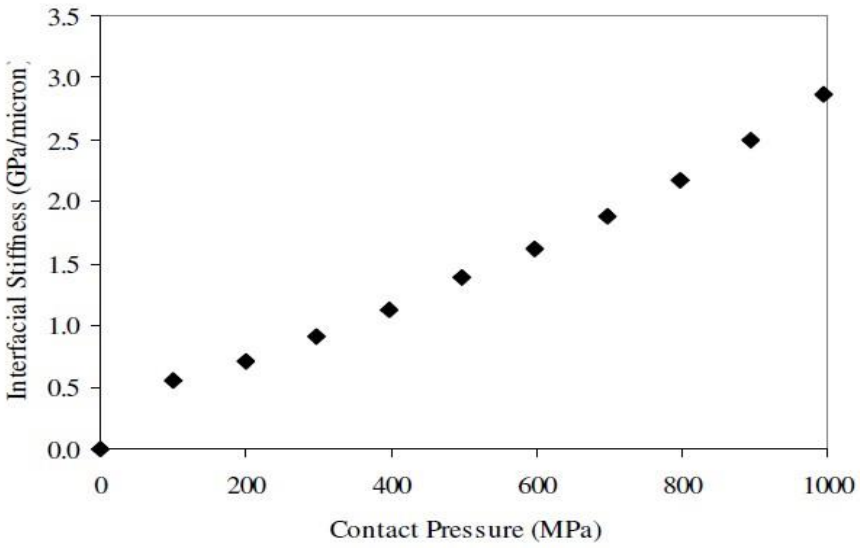

Figure 5.14 Calibration Curve Relating Interfacial Stiffness to Contact Pressure [26]

5.7 Summary

In this chapter basic test apparatus and test rigs for static contact measurements and dynamic contact measurements are introduced. An ultrasonic focusing transducer used for static measurements and a scanning array used for quasi-static and dynamic tests are introduced, and the working principles are described. The test set-up for different contact cases are presented. Basically the transducer is used for static contact measurements and can provide high resolution results. The scanning array is used for dynamic contact measurements, but the resolution is restricted by the pulsing speed of the array and physical arrangement of ultrasonic elements. Under the current test conditions, resolution of measurements are normally not higher than static ones. So the static results are also used as a validation of the dynamic measurements to prove the applicability of the new scanning method developed in the work.

Chapter 6:

Ball-on-Flat Contact

6.1 Introduction

In this chapter, a ball-on-flat contact is investigated using ultrasound reflectometry. The ball-on-flat contact is a relatively simple and basic contact, and ball bearings are widely used in motors, turbines, and other mechanisms for reducing the friction between rotating axes and supporting frames, which makes it an ideal case for pilot study of the ultrasonic array. As mentioned in Section 5.7, measurements from the array do not have as high a resolution as those from the ultrasonic transducer used for static tests, common steel ball bearing contacts, most of which no bigger than a 1mm diameter circle, cannot be easily detected by the array. Therefore, the specimens were a Nitrile ball and a piece of Perspex plate instead of normal steel specimens to obtain a larger contact for detection purposes.

A simple ball-on-flat contact system is chosen as the test objective in this paper for validating the applicability of the new scanning array since the ball-flat contact system is straight forward and has been thoroughly researched into, so that the dynamic scanning results can be easily calibrated by theoretical predictions, finite element analysis and static ultrasound scanning outcomes. Considering the resolution limitation of the 64-element ultrasonic array and the small scale of the test rig, a nitrile ball is used in contact against a perspex plate to get a relatively large contact patch which can be distinguished by the array. The material properties of Nitrile are to some extent different from those of Perspex in terms of the speed of sound and density, which cannot be ignored, as the differences would affect final contact pressure calculations.

6.2 Properties of Samples

A 13mm radius nitrile ball was used in contact against perspex plate. Properties of nitrile and perspex are listed in Table 6.1

	Density (kg/m³)	Speed of Sound (m/s)	Young's Modulus (MPa)
Nitrile	1.2	1600	5
Perspex	1.18	2730	3200

Table 6.1 Properties of Nitrile and Perspex

From Table 6.1 it can be seen that the Young's modulus of these two materials are relatively small compared to common metals, especially that of Nitrile. Therefore large and nonlinear deformation is expected in the tests.

6.3 Test Conditions

6.3.1 Nitrile Ball-Perspex Static Tests

In static tests, the nitrile ball was placed in a spring loading frame with a perspex disc fixed on the top and a holding plate in the middle (Figure 6.1). The load is applied through three compression springs. The springs have been pre-calibrated and stiffness been calculated. By compressing the whole loading frame for a measured length loads can be precisely applied. A container was made and mounted on top of the frame to hold water couplant. A 10MHz ultrasonic scanning probe was sunken in the water and it can move in three directions freely.

From Table 6.1 it can be seen that the acoustic impedance of Perspex is larger than that of Nitrile, according to equation 3.3, the magnitude of reflected signals is small. Although the magnitude can be enlarged with increased voltage gain, noise signals caused by scattering effect inside the transmitting materials and other electrical interference are amplified as well. This adds difficulties in actual data acquisition and post-processing.

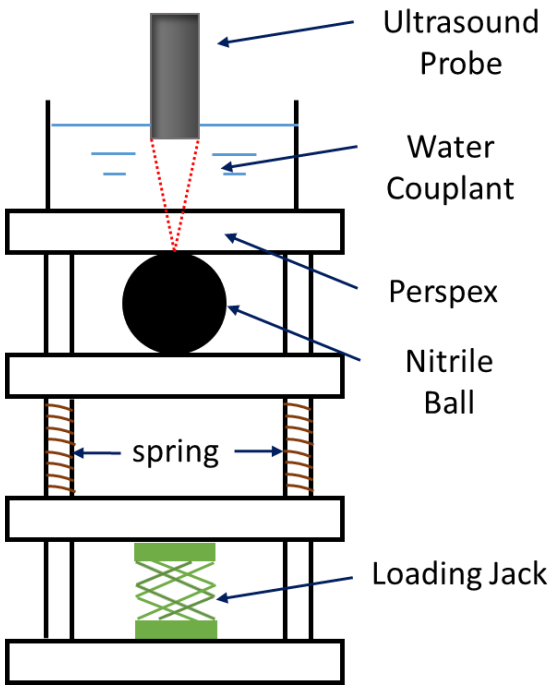

Figure 6.1. Static Spring Loading Frame

6.3.2 Nitrile Ball-Perspex Dynamic Tests

The dynamic tests were split into two parts, contacts of a Nitrile ball rolling and sliding over Perspex were scanned with a fixed ultrasonic array and the contact of steel ball rolling over steel groove with a rotating array. The aim of the test was preparation for further dynamic test on full scale wheel-rail rolling contact, and pilot study of applicability of the ultrasonic array in characterizing different contacts under various conditions.

6.3.2.1 Rolling case

The dynamic test used exactly the same Nitrile ball as that in the static test. The ball was placed on a steel plate which could move in the longitudinal direction and was loaded up against a “fixed” plate. A motor drove the steel plate which caused the ball to roll. A schematic image of the test rig is shown in Figure 6.2.

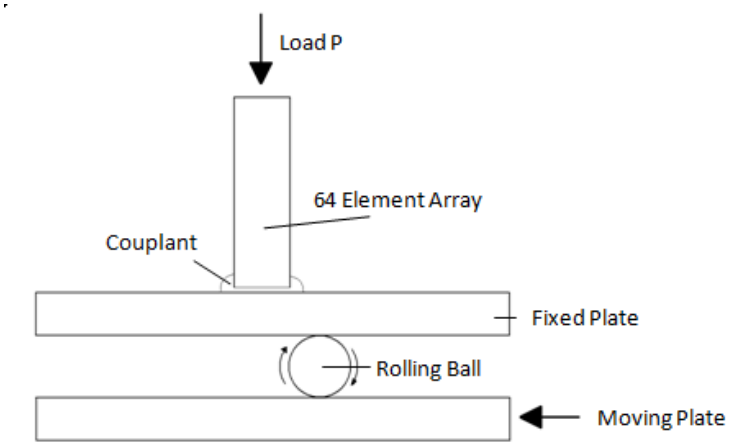

Figure 6.2 Ball-on-Flat Dynamic Test

The speed of the motor could be switched from 3mm/s to 7mm/s and a series of loads were applied from 2N to 10N.

The 64-element ultrasound scanning array as described in Chapter 4 was mounted on the fixed Perspex plate. The array was linked with a multiplexor and computer. Ultrasound signals were pulsed from 8 elements each time and reflected at contact surface. Once the switching speeds of the pulsing channels are fast enough, it could be regarded as a 64-element measurement was taken simultaneously. Reflected signals were stored in PC and analysed in Labview. During the period of these tests were taken, the pulsing speed is not fast enough so the whole tests could only be carried out at a relatively low speed.

6.3.2.2 Sliding case

The sliding test set-up was basically the same that for the as rolling case, but the ball was fixed onto the bottom plate with a clamp. When the bottom plate moved, the ball went with the plate. Since the nitrile ball was clamped, it was 100% sliding along the top perspex plate.

It should be noted that under the same speed of the bottom plate, the resulting relative speed between ball and plate in rolling case is half of that in the sliding case. Therefore with same testing time, contact patch data captured in the rolling test is twice that as in sliding case, actually the contact size in both cases should be the same.

6.3.3 Steel Ball-in-Groove Dynamic Tests

The ball-in-groove dynamic test was carried out on a steel plate mounted over three steel balls. As can be seen in Figure 6.3, the balls are symmetrically distributed under the plate and kept in position with ball holders. Bearings are mounted inside the ball

holders so that the steel balls can rotate freely. A shallow groove was machined on the plate along the contact region with steel balls. The radius of the groove was 10.5mm and the radius of the balls was 11mm. Two tiny holes were drilled through the plate for clamping the ultrasonic array. The array rotates with the plate, when the array moved into the contact region, amplitude of reflected signals of involving elements droped and a contact was captured.

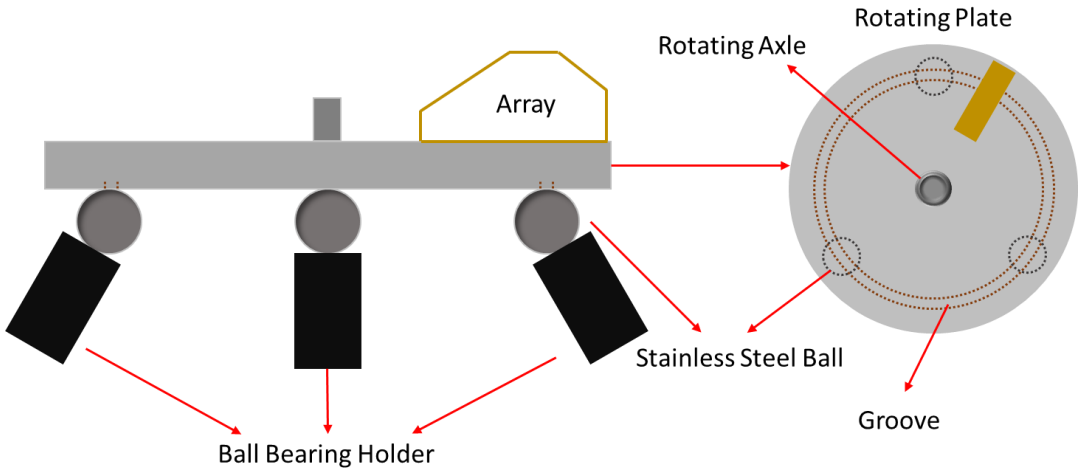

Figure 6.3 Steel Ball Groove Contact Test

6.4 Data Acquisition and Post-processing

For all the static and dynamic ball-on-flat tests, the reflected signals from the interface were received by the ultrasonic transducer or the array and peak to peak values of the signals were recorded. In static tests, data was saved in a long line format continuously, each value has its own corresponding x and y coordinates. A 2-D reflected voltage map can be obtained by rearranging the values according to the coordinates (as shown in Figure 6.4a). In dynamic tests, because the array is divided into 8 channels, the channels pulse and receive signals one after another. In one cycle, each channel pulsed multiple times before switching to the next one, and each time 8 values from the channel were recorded in a row. Averages of all rows from one channel in one cycle were taken (the first and the last row were neglected because reflected signals fail to contain contact information during channel switching period). A 2-D reflected voltage map can be obtained by rearranging all the averages of a single cycle into one row and duplicate the process to all cycles.

Therefore, in static tests, initial resolution of the results depends on the minimum steps of the scanning tank along x and y directions. In dynamic tests, the resolution of longitudinal direction (direction of relative motion) depends on the time spent in one cycle, which is related to the velocity of the contacting bodies and the switching speed, and resolution of the lateral direction is fixed to 64 as the number of array elements.

Once the reflected voltage maps were acquired, the reflection coefficients can be calculated with a reference. Considering the properties of ball-on-plate contact, where the plate is flat in all directions, so only a reference point is enough. The reference point

can be chosen from the region not in contact in the 2-D reflected voltage map. According to Equation 3-3, reflection coefficients were calculated by dividing the reflected voltage map against the reference point. And the reflection coefficient map was plotted (as shown in Figure 6.4b), here the matrix was interpolated for better viewing. The acoustic impedance of Nitrile and Perspex can be calculated through Equation 4-2, and maps of contact stiffness can be plotted according to Equation 4-3.

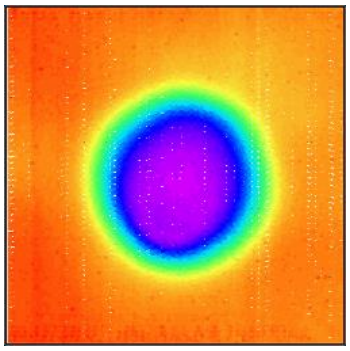

(a)

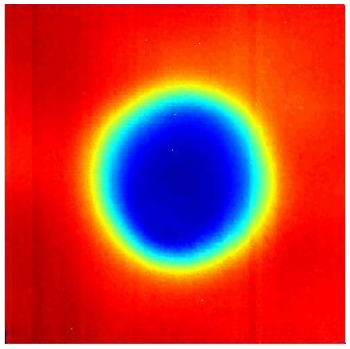

(b)

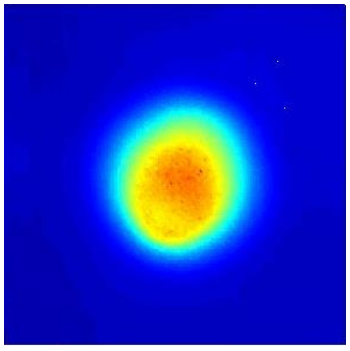

(c)

Figure 6.4 Reflected Voltage, Reflection Coefficient and Contact Stiffness Maps

6.5 Test Results

6.5.1 Nitrile Ball-Perspex Static Contact Result

A series of loads from 10N to 50N with 10N steps were applied. The scanning area is 10mm by 10mm square. The resulting reflected voltage distribution maps are shown in Figure 6.5. Maps of reflection coefficient and contact stiffness are shown in Figure 6.6 and Figure 6.7 respectively.

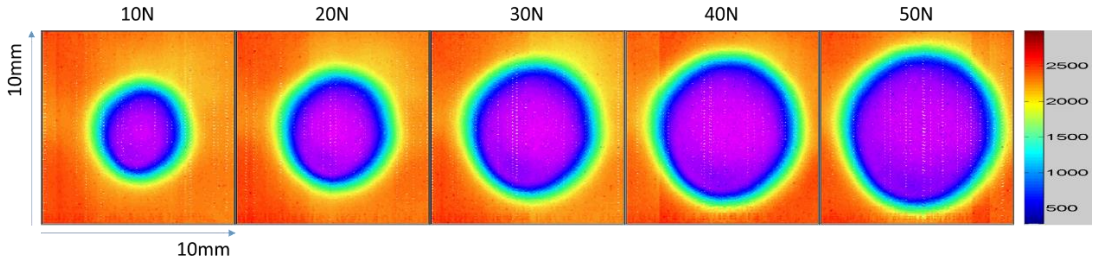

Figure 6.5 Reflection Voltage Map of Static Ball-on-Flat Contacts

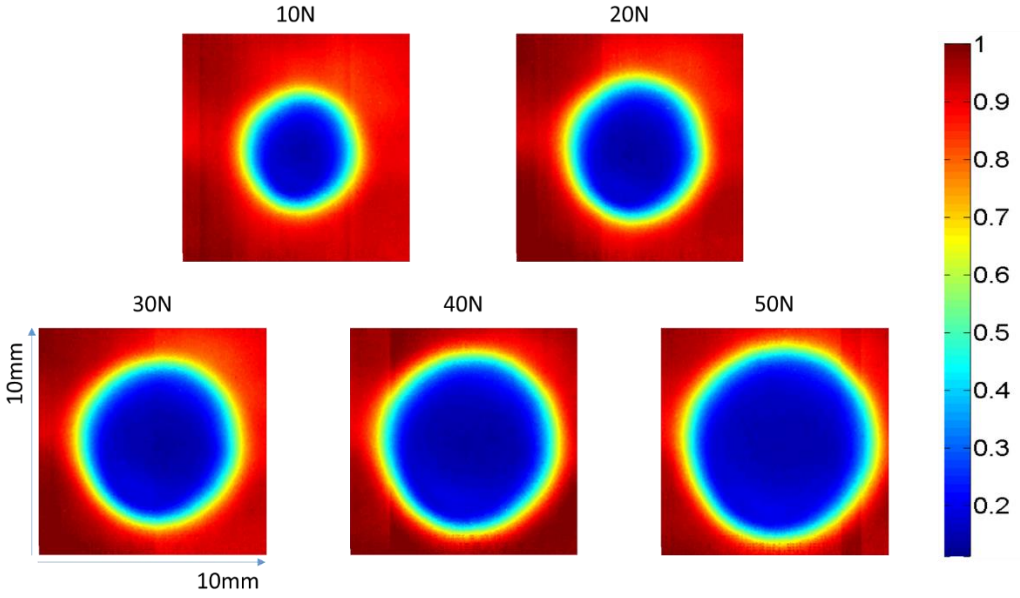

Figure 6.6 Reflection Coefficient Map of Static Ball-on-Flat Contacts

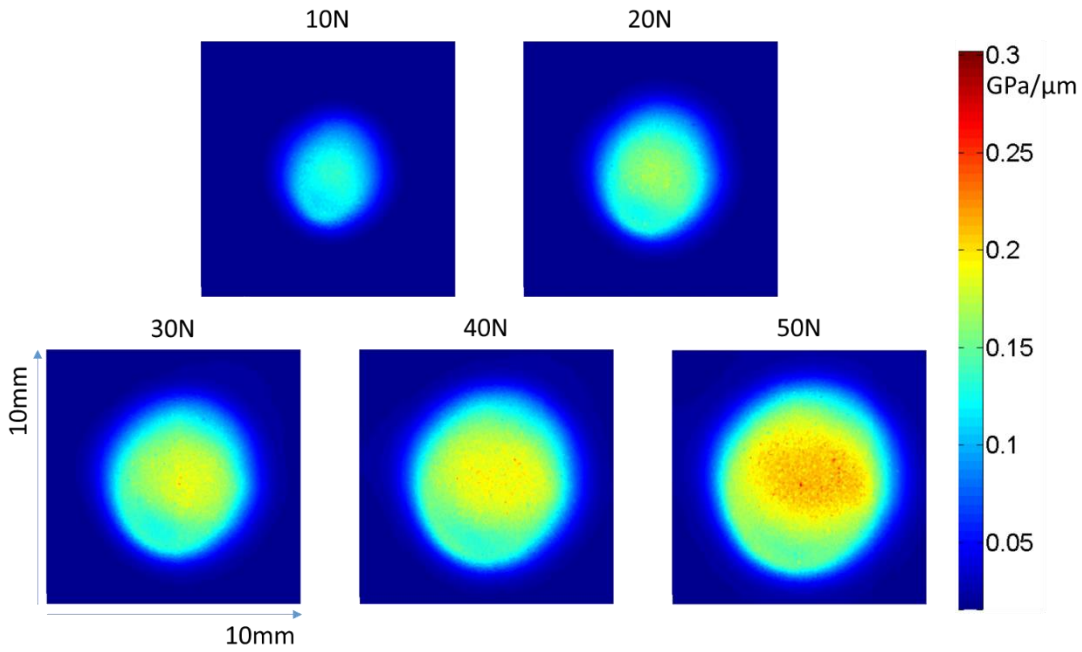

Figure 6.7 Contact Stiffness Map of Static Ball-on-Flat

6.5.2 Calibration

A calibration test was carried out by using the same loading frame and Perspex plate in contact with a 3mm radius 1mm thick Nitrile disc. The Nitrile disc was cut off from a 1mm thick Nitrile sheet. The Nitrile calibration sample cannot be too big so that the calibrating contact pressure can cover the range where pressures of original ball-flat tests. What is more important, due to properties of Nitrile, a large sheet of Nitrile may squeeze and corrugate when in contact, leaving some parts in contact and some areas not in contact. Besides, since Nitrile will deform nonlinearly in the contact especially around the edge due to insufficient constraints, no flat contact is expected near the edge. On the other hand, the sample cannot be too small, otherwise the sample will distort and deform irregularly during contact.

In the test, loads were applied from 10N to 50N. Reflection coefficient maps are shown in Figure 6.8. It is impossible to obtain complete plane-to-plane contact in calibration test. Even with the calibration specimen used here, the edge effect is still inevitable. From Figure 6.8 it can be seen that reflection coefficients around the edge are higher than those in the middle. Through equation 4.4, contact stiffness can be derived from reflection coefficients, and stiffness maps were plotted as shown in Figure 6.9. The irregularities can be seen more clearly in contact stiffness maps. To extract valid calibration information from the data, the contact area is divided into several regions according to stiffness values. Values in a same region are close to each other, averages are taken in each region. The contact pressure for calibration is approximated by dividing the load with whole contact area.

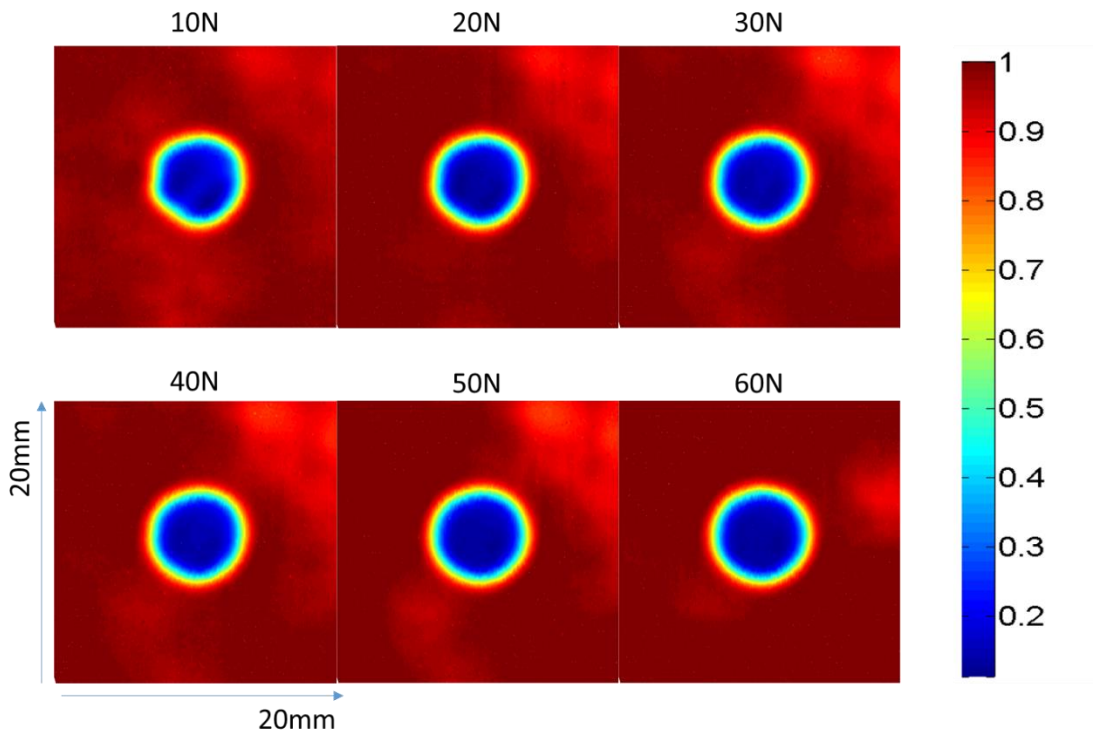

Figure 6.8 Reflection Coefficient Map of Calibration Test

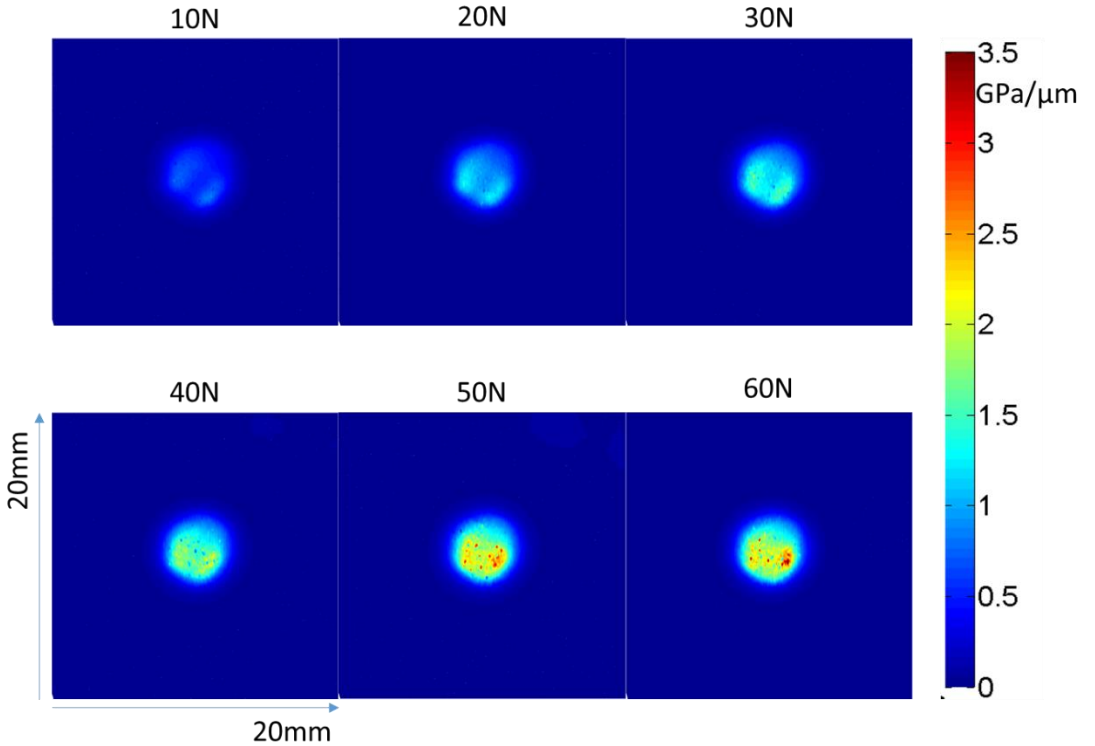

Figure 6.9 Contact Stiffness Maps of Calibration Test

A calibration curve can be plotted between contact pressure and interfacial stiffness, as shown in Figure 6.10. As it can be seen from Figure 6.8 and Figure 6.9, even though

the scanning objective is a flat plate against a flat disc, due to the flexibility of nitrile, the flat-flat contact in this case is not an even circle, but behaves more like a ball-on-flat contact. Since the calibration test is influenced by a lot of factors. The calibration curve acts more like a reference rather than being used for precise calculations.

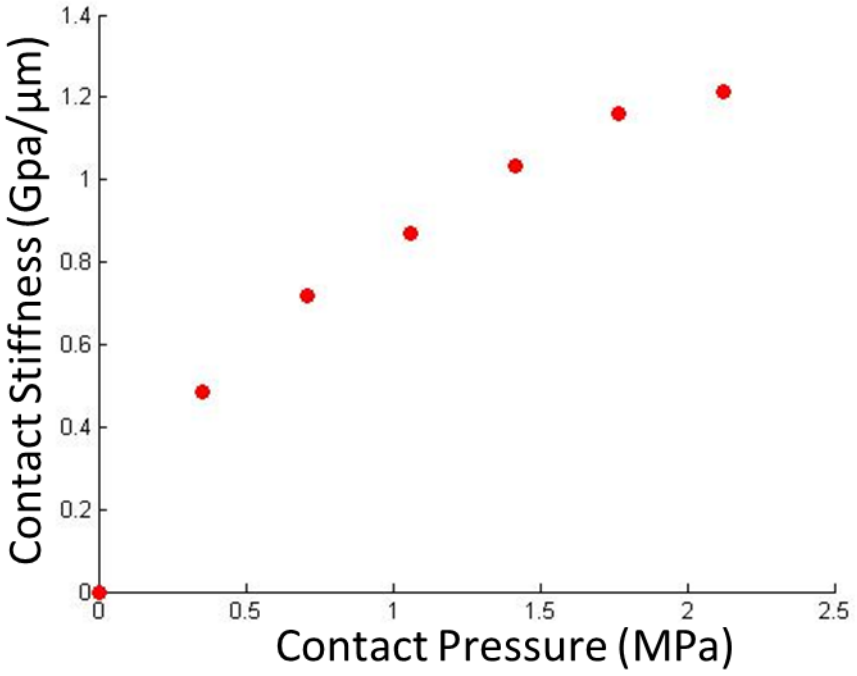

Figure 6.10 Calibration Curve of Nitrile-Perspex Contact

From the calibration curve shown in Figure 6.10 it can be seen that the relationship between contact pressure and contact stiffness is non-linear. The growing rate of contact stiffness turns to be lower under higher contact pressure, which meets the expectation that contact stiffness is more difficult to grow as load increases.

6.5.3 Nitrile ball-Perspex Dynamic Test Result

The resolution of the measurement in the X-axis was 0.7mm, which was determined by the physical size of the elements in the array. The Y-axis resolution was dependent on rolling velocity of the ball and element pulsing repetition rate.

Reflection coefficient maps in rolling case under different load and speed are shown in Figure 6.11.

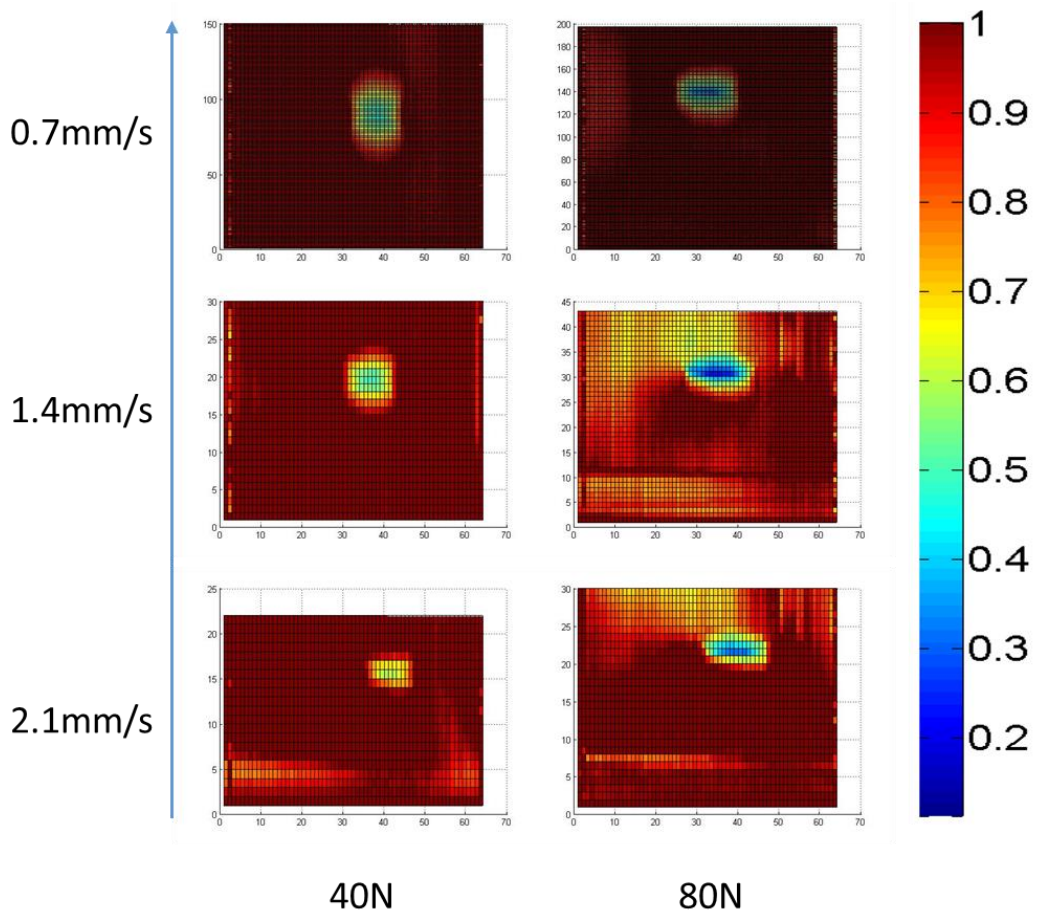

Figure 6.11 Reflection Coefficient Images of Nitrile Ball on Perspex Plate Dynamic Contacts at Different Loads and Speeds (The Arrow Indicates Rolling Direction)

Reflection coefficient maps in rolling case (left) and sliding case (right) with 20N load applied are shown in Figure 6.12

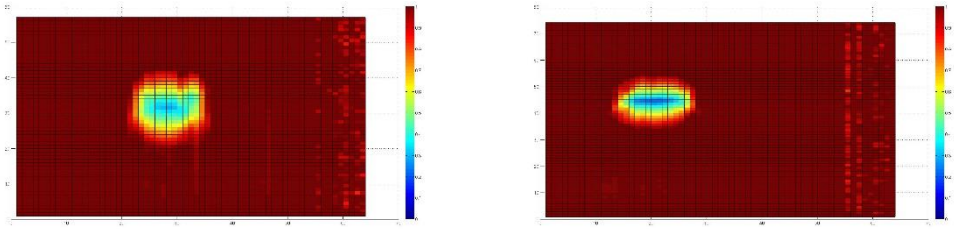

Figure 6.12 Reflection Coefficient Images of Nitrile Ball on Perspex Plate Dynamic Contacts at Different Loads (Left: rolling Right: sliding)

6.5.4 Nitrile Ball-Perspex Dynamic Test Result

A comparison was made between measurements from dynamic nitrile ball-on-flat rolling tests and static ball-on-flat tests. The rolling speed of the compared dynamic

tests was 0.7mm/s, and the load was applied from 10N to 50N to match the static tests. Contact stiffness maps of the dynamic tests are shown in Figure 6.13.

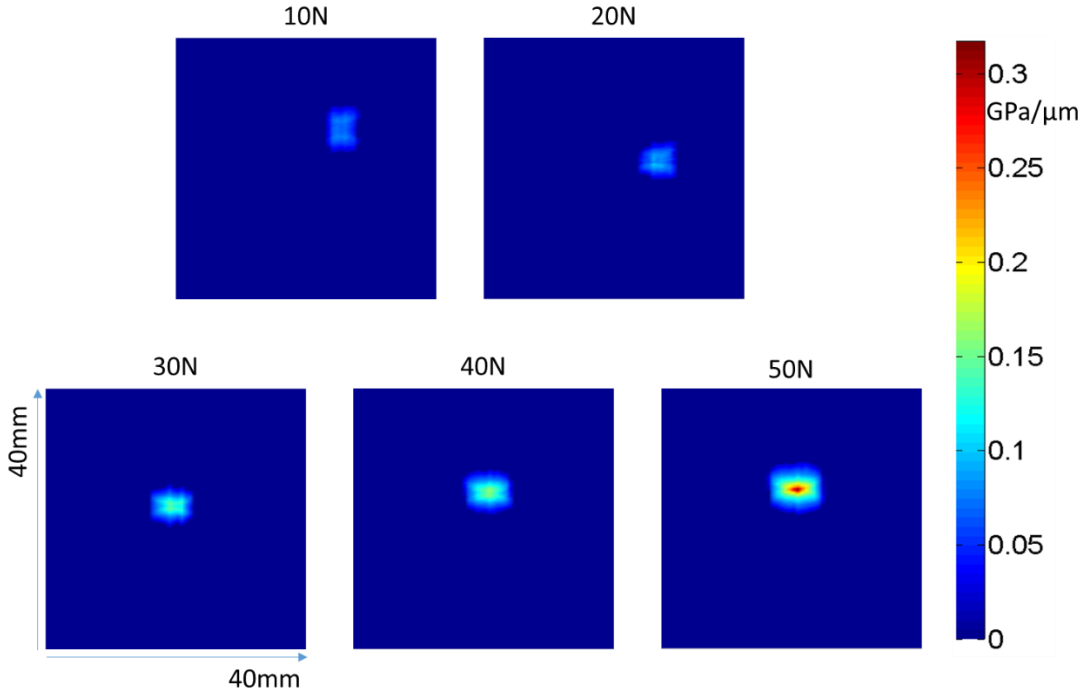

Figure 6.13 Contact Stiffness Maps of Nitrile Ball-on-Flat Rolling Test

According to Figure 6.7 and Figure 6.13, a graph was plotted in terms of maximum contact pressure against load for both static and dynamic tests (as shown in Figure 6.14). It should be noted that theoretically in static tests, the reflection coefficient should not be lower than $(z_1 - z_2)/(z_1 + z_2)$. However in actual tests, there are some points of data going below the bottom limit due to oscillation of the test rig, tiny inclination of the ultrasonic transducer or random electric interference, etc. These points were replaced by values close to but above the bottom limit. From Equation 4.3 it can be derived that incredibly high contact stiffness and contact pressure were calculated from these points. Therefore, the maximum contact pressure chosen from the static ball-on-flat tests were averages of a small area in the contact centre rather than a single point, in order to avoid unreal results. Comparison of contact sizes was made between static and dynamic tests as well, contact sizes from static tests are calculated according to Figure 6.5, and sizes from dynamic tests are based on the number of elements that detected contacts. The graph is shown in Figure 6.15.

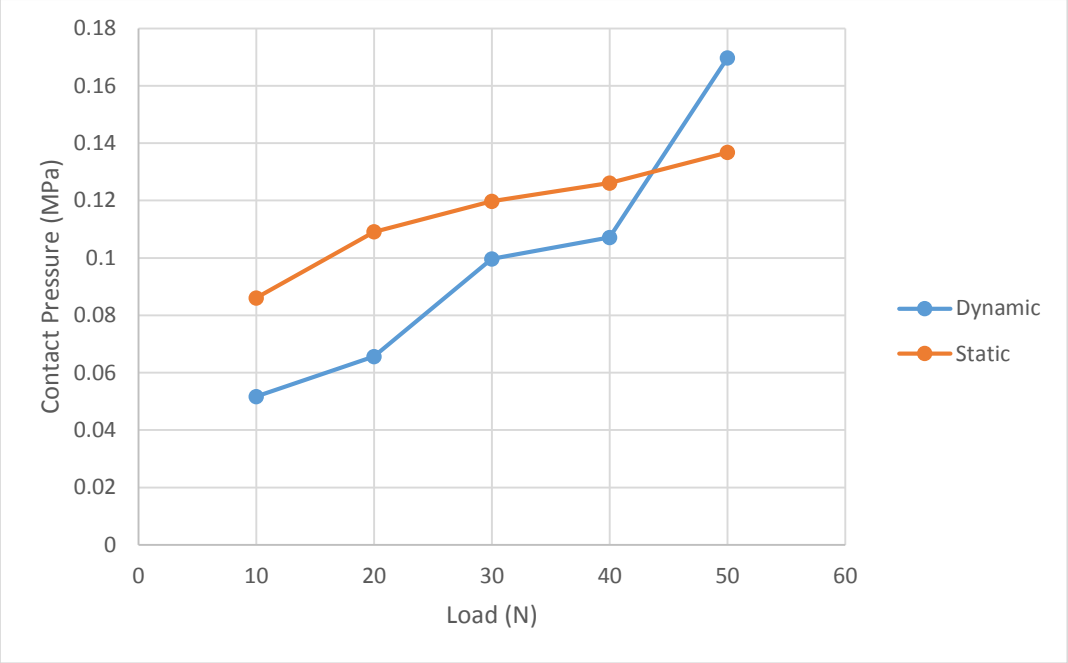

Figure 6.14 Maximum Contact Pressure of Static and Dynamic Ball-on-Flat Tests

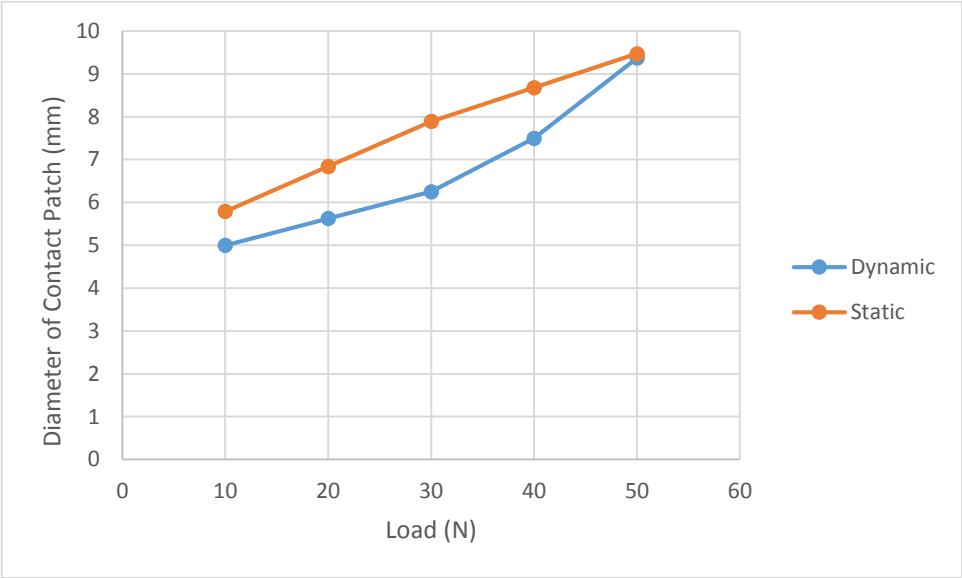

Figure 6.15 Contact sizes of Static and Dynamic Ball-on-Flat Tests

As the static and dynamic tests on ball-on-flat were carried out with Nitrile ball and Perspex plate, and the non-metal contacts characterization with ultrasound, especially materials with relatively different acoustic impedance, therefore no previous research on similar contacts has been done. Because of the non-linear property of Nitrile, the Hertz theory cannot be used as a comparison either. Further finite element simulation could be planned in future work for comparison.

6.5.5 Steel Ball-in-Groove Dynamic Test Result

Since the rig is not specially designed for this test, no loading system was available. Masses were directly placed on the plate. Figure 6.16 shows one full cycle of dynamic test. Because the steel ball bearing contact is hard to detect for the array, the plate is rotating at a relatively low speed, the line velocity at the groove position is 1.2mm/s.

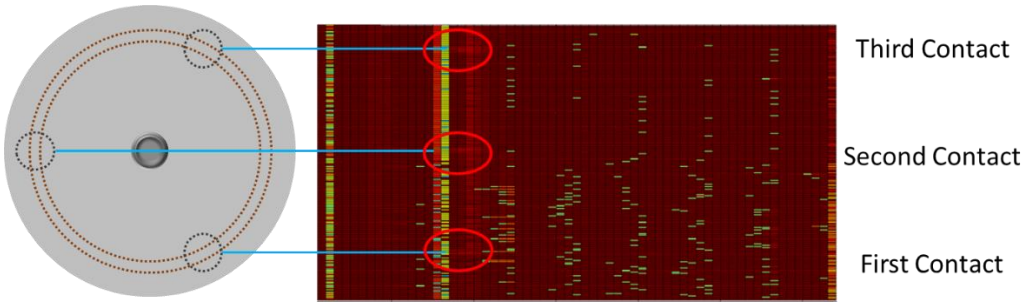

Figure 6.16 Reflection Coefficient Map of Steel Ball-in-Groove Dynamic Contact Test

Figure 6.17 shows the zoom-in plot of the zone of interest. From the figure the contact patches can be observed more clearly. Because the radius of the ball is larger than that of the groove, so it can be seen that there are two concentrated contacts at two sides of the groove for each ball respectively.

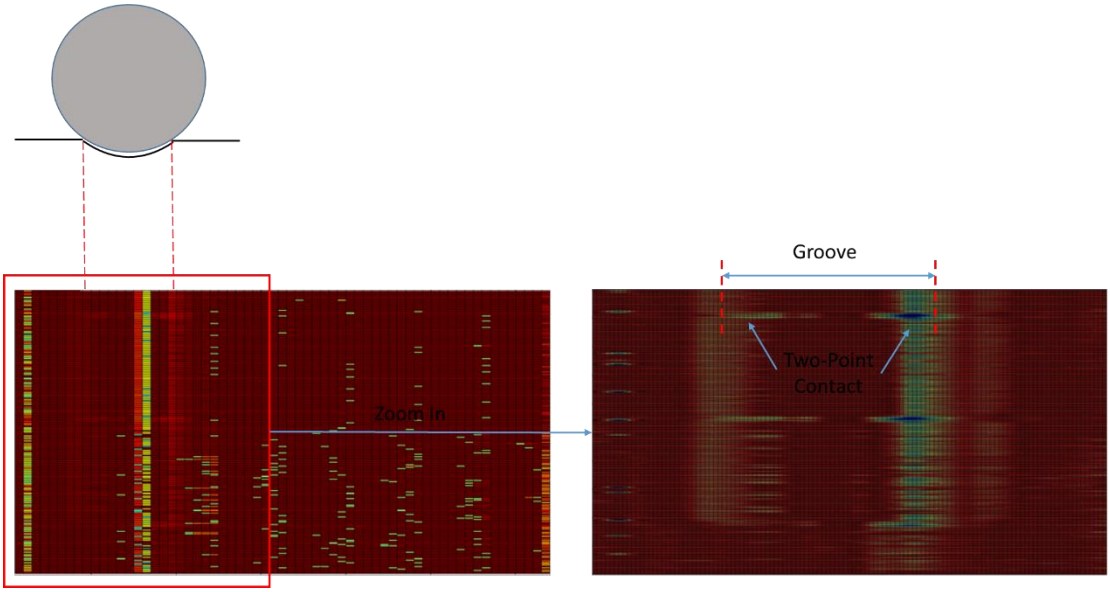

Figure 6.17 Zoom-In Reflection Coefficient Map of Steel-Groove Dynamic Contact Test

Static tests were carried out measuring a steel ball in contact with a grooved plate with same radius as a validation. As it can be seen from Figure 6.18, the two point contact is also observed in static measurements.

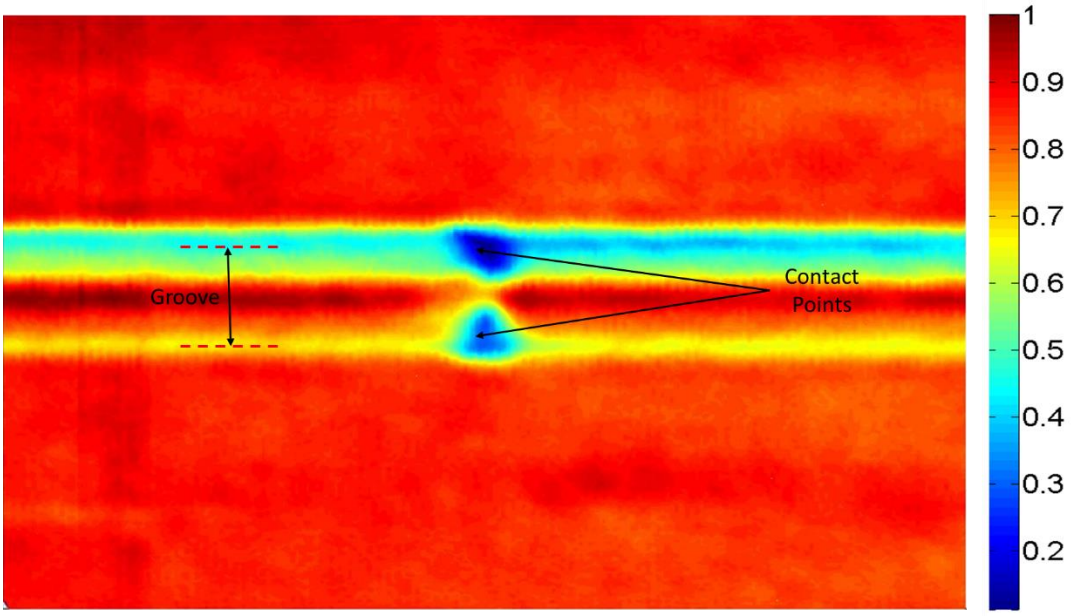

Figure 6.18 Static Measurements of Steel-Groove Contact

6.5 Discussion

Results from the static Nitrile ball-on-flat tests show a steady growth of contact patch with increasing load. Because of the properties of Nitrile, the contact behaves non-linearly, which makes the measurements look more irregular in terms of contact stress distribution. Calibration tests were carried out in an attempt to establish the exact contact stresses, but the calibrating process itself cannot avoid uneven contact even with a quite small nitrile calibration disc, a calibration zone rather than a calibration curve was plotted. Although the contact pressure calculations are debatable, the contact size can be easily obtained from the measurements. The tests also points out a new research direction in characterizing non-linear contact using ultrasound since most previous ultrasound scanning work is done on metals.

The circular contact is captured by the array clearly in dynamic tests, and the growth of the contact patch and contact pressure can be observed through drops of reflection coefficients with increasing loads. As it was expected, the higher rolling speed led to a lower quality result. In the 3.5mm/s case, only a few pixels are captured indicating contacts and the contact shape can hardly be recognized as a circle. From the comparisons between pure rolling contact measurements and pure sliding contact measurements, no significant differences were found in terms of contact shape. The pressure distribution which ought to be quite different from each other, did not vary much here due to the limitation of the resolution. But it is promising that with better

equipment and relevant software developed, the recognition of rolling or sliding contact can be more apparent and straightforward.

A comparison was made in terms of maximum contact stiffness between static and dynamic ball-on-flat measurements. From Figure 6.14, contact pressure from dynamic tests are generally lower than static measurements except the one under 50N load. Growing rate of the pressure are basically the same from both tests, except for the 50N load test in dynamic test. A dramatic increase in maximum contact stiffness was observed. In dynamic tests, the resolution along the rolling direction is 250 at the lowest speed, and the resolution along the array scanning direction is fixed at 64, both of which are far lower than that of static tests. A single point of measurement in dynamic tests represented a much larger area of contact compared with static tests. This led to all the contact information especially the asperities contact pressure which normally are higher than averages in local area were replaced by one data. So this explains why peak pressures from dynamic tests were generally lower than static measurements. Meanwhile, due to the limited resolution, results are more easily influenced by the environment or unpredictable signal fluctuations in dynamic tests, there were one or two measurements going over high or over low as the peak pressure measured under 50N load. Contact sizes from dynamic tests match well with those from static tests according to Figure 6.15, with being a little smaller. This can also be explained by the resolution difference between the two methods. Because of the low resolution in dynamic tests, some contact information close to the boundary of contact area cannot be reflected in the 2-D map. If measuring larger contacts, the influence from the resolution limitation would be less.

Although the new developed scanning method has its limitation in detecting small contacts, the results shown in Figure 6.11 and Figure 6.12 provides some useful information from the steel ball-in-groove contact. The contact positions of the three balls are correctly recorded, and the two-point contact, although a little bit faint, can also be observed. The dynamic measurements match well with scanning results of static tests. The tests carried out here prove the wide applicability of the array. In some cases where the array needs to be mounted on the moving bodies, the measurement can still be taken normally.

6.6 Summary

In this chapter, the interface of a ball in contact with a plate is investigated. Both static and dynamic contacts were tested. The static measurements were taken over a nitrile ball against a perspex plate, where non-linear contacts were observed. The new developed method was applied here investigating ball rolling and sliding over a flat

surface. Results are compared between static tests and dynamic tests. Results from dynamic tests using the new technique, although being a little lower, match the static measurements in the whole view. A steel ball-in-groove contact was also investigated with a rotating array mounted on the top, the contact patches were although small and faint, were still detectable using the array. Limited by resolution, the new scanning technique cannot extract contact information as accurate as the static method, and it is more sensitive to influencing factors. But generally speaking, the new technique has been proved to be a relatively stable method which can provide enough contact information and can be applied to a wide range measuring environment, especially in larger contact area cases such as a wheel-rail contact, which is introduced in Chapter 8.

Chapter 7:

Wheel-Rail Static Contact

7.1 Introduction

In this chapter, the static contact of a pair of wheel and rail specimens is characterized using ultrasound reflectometry and finite element method respectively. Results from both methods are compared with Hertz theory. Although the final aim of the project is to characterise the dynamic wheel-rail contact in real time, but prior to that, it is necessary to understand the static wheel-rail contact. In Chapter 6, the static ultrasound scanning technique has been used for measuring ball-on-flat contact. In this chapter, the scanning method was used on characterising contacts with more complicated profile and higher loads. The research work done in this chapter can be both used as preparation and validation of the further dynamic tests.

7.2 Test Specimens

The test specimens were a piece of worn rail head specimen and wheel specimen cut from an actual wheel. The wheel specimen was a cut off from a R7 whole wheel, and the rail head specimen was a cut from a BS113A rail section with a sand damaged head. The radius of the rail head is 300mm and the wheel radius is 450mm. The length of the rail specimen is 75mm and the wheel specimen is 100mm long, and width of the wheel and rail is 80mm and 69mm respectively. Photos of test specimens are shown in Figure 7.1.

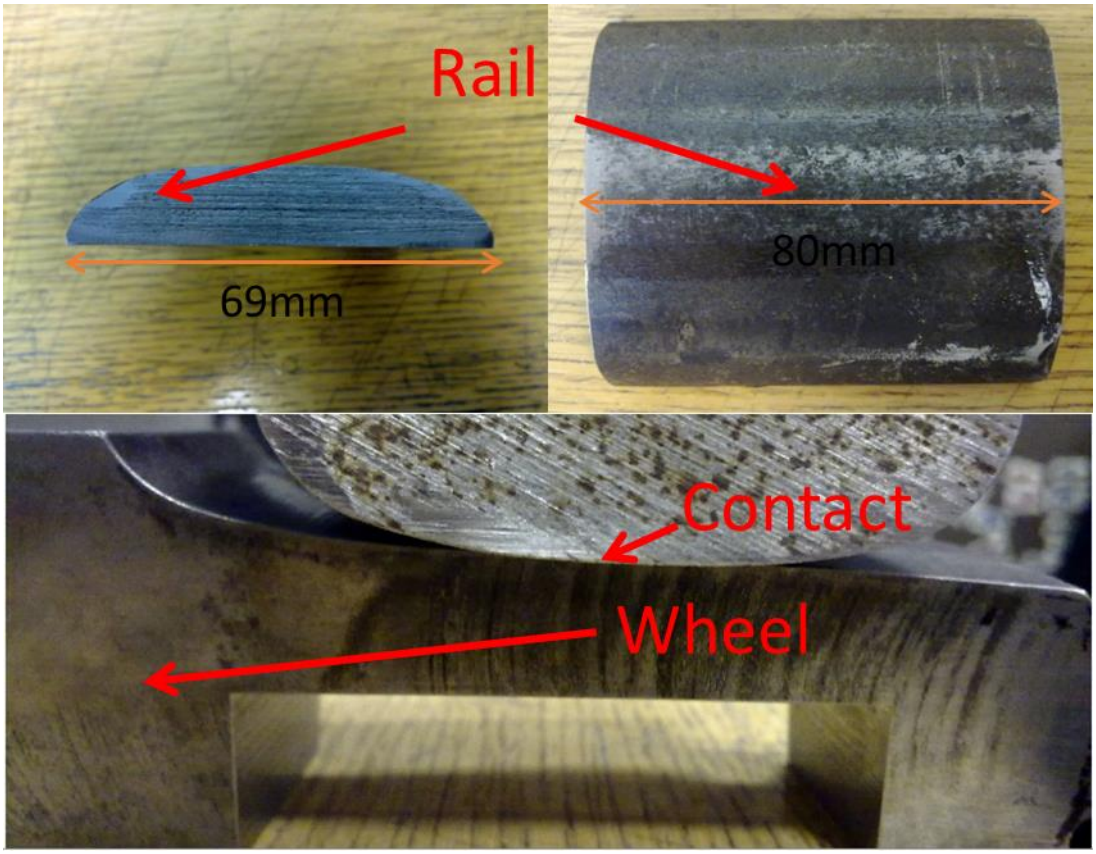

Figure 7.1 Photos of Wheel and Rail Specimens

7.3 Wheel/Rail Static Test

The static wheel-rail contact scan was taken on the scanning tank described in Chapter 5 (see Figure 5.4). The wheel and rail specimens were loaded up in the loading frame with a distilled water bath above; the rail was fitted into a groove in the loading frame. The water bath was used to focus the ultrasound signals and to reduce attenuation. It is necessary to use distilled water so as to prevent rust of the rail specimen. Measurements were taken as the focusing transducer scanned over the rail bottom. To make sure the rail head is in contact with the wheel tread, a slant was used. A schematic image of wheel/rail static test is shown in Figure 7.2

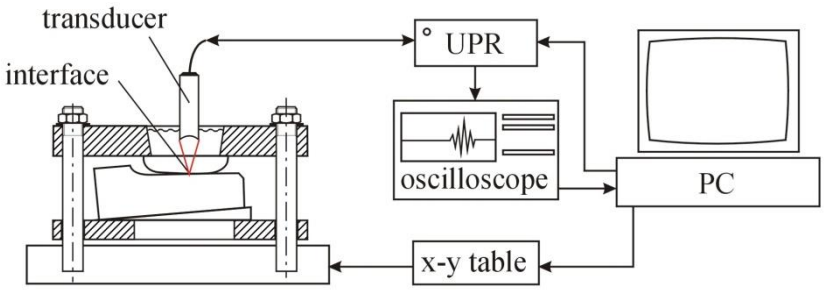

Figure 7.2 Schematic image of Wheel/Rail Static Ultrasound Measurements

A series of loads from 40kN to 65kN were applied. A hydraulic jack was used to apply the load. Reflected voltage images acquired from static measurements are shown in Figure 7.3.

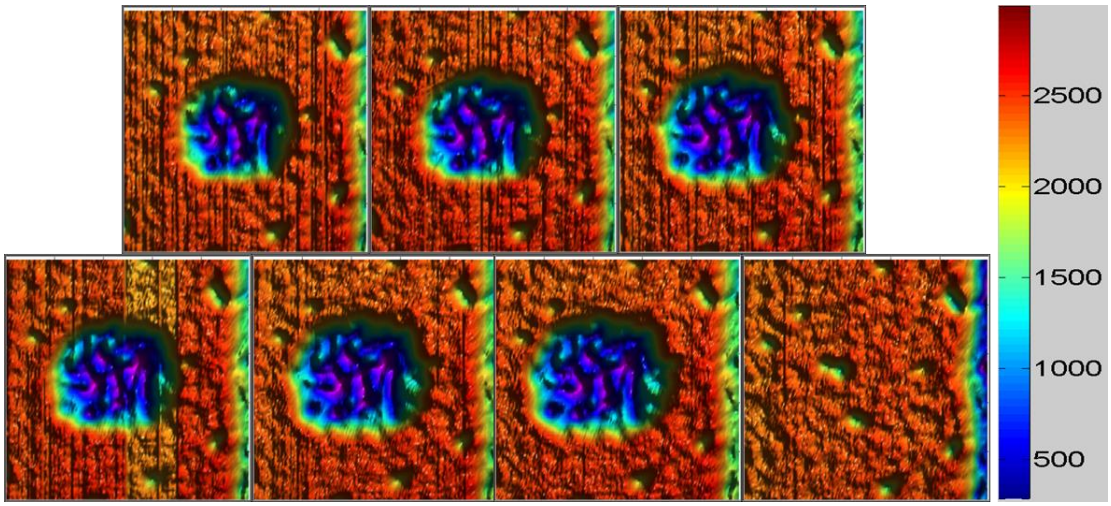

Figure 7.3 Reflected Voltage Distribution of Wheel-Rail using Ultrasound Reflectometry (from left to right: 40kN, 45kN, 50kN, 55kN, 60kN, 65kN and reference)

7.4 Finite Element Analysis for Wheel/Rail Contact

A 3-D wheel-rail model was developed in ANSYS. Dimensions of the wheel and rail profiles were taken from the ultrasound test specimens. Both wheel and rail materials were set to be structural steel. The wheel tread was set as the contact surface and the rail head was the target surface. Contact behaviour was symmetric; algorithm for solving the contact problem was pure penalty, as mentioned in Section 3.3, some penetration is allowed for the initial contact pair. The mesh was refined in potential contact regions. The whole model had 123015 elements. The elements for modelling contact pairs are CONTAC48, this type of element uses a penalty approach to model contact. The surface behaviour was set to ‘adjust to touch’, when one surface came into contact with the other, a spring of stiffness was put numerically between the two. 3-D and meshed models are shown in Figure 7.4. The bottom of the wheel section was constrained with fixed and the load was applied perpendicular to the top section of the rail. In order to avoid large displacement of the rail, the rail model was constrained and only free to move in the normal direction.

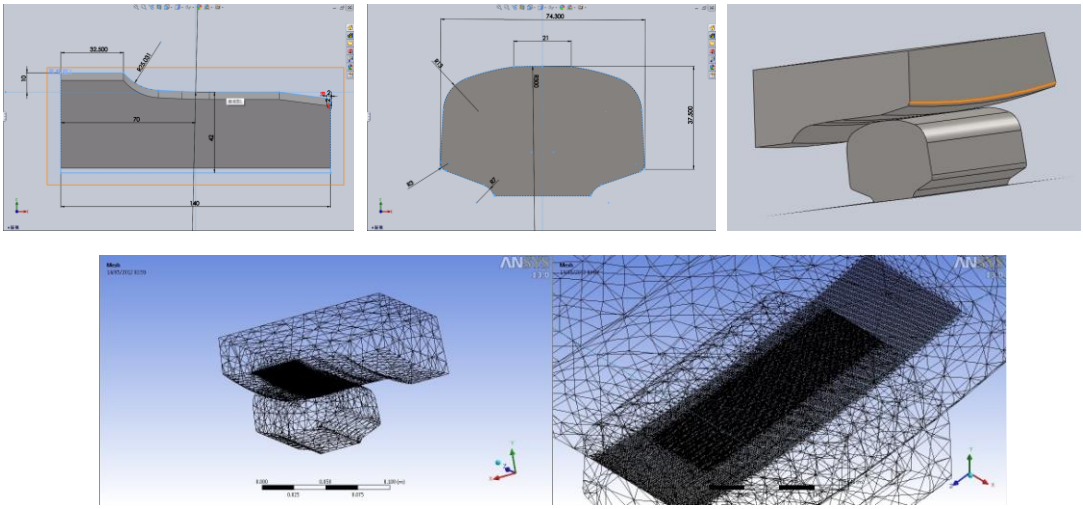

Figure 7.4 Finite element models of wheel/rail contact

7.5 Results and Discussion

7.5.1 Ultrasound Scanning and Finite Element Simulation Results

Similar steps were taken as in the ball-on-flat tests. What is different is that a reference map is essential here due to the curved profiles of the contacting surfaces. The reflection coefficient matrix could be acquired from dot division of the reflected voltage matrix and reference matrix, and then contact stiffness could be obtained by applying Equation 4.4.

During the test, it could be seen that there were apparent scratches and pitting on the rail specimens, which is a sand damaged specimen. According to calibration test done by Marshall et al. [26], the empirical equation to best fit the calibration data is P=263K. Figure 7.5 shows the calibration curve for sand damaged specimens.

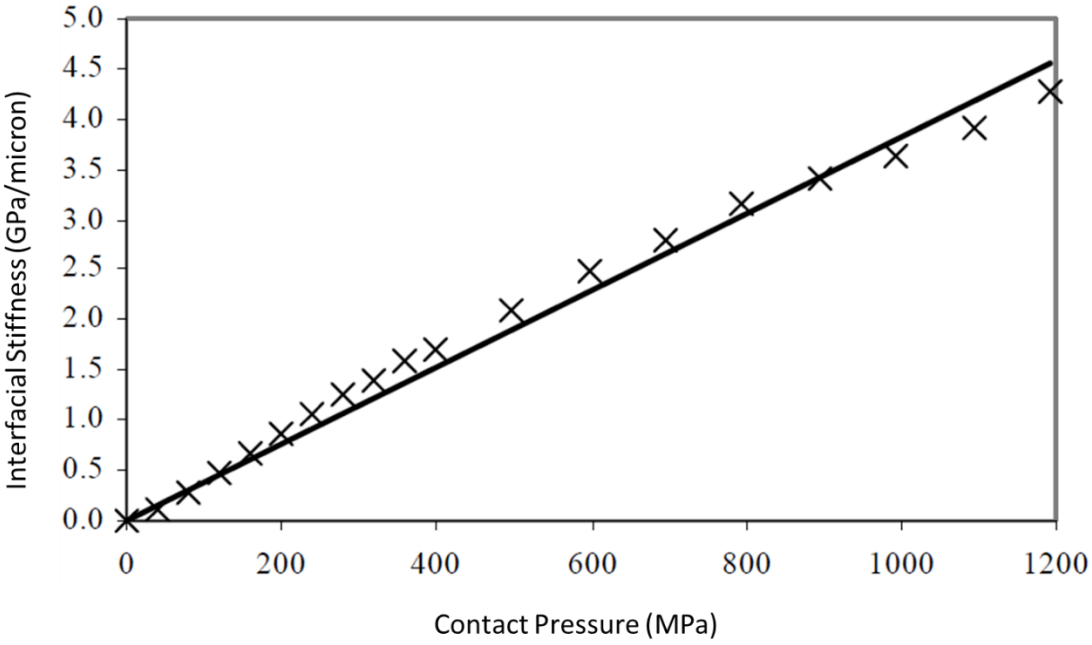

Figure 7.5 Sand Damaged Interfacial Stiffness-Contact Pressure Calibration [26]

Reflection coefficient maps are shown in Figure 7.6 and contact pressure distributions under all loads are shown in Figure 7.7

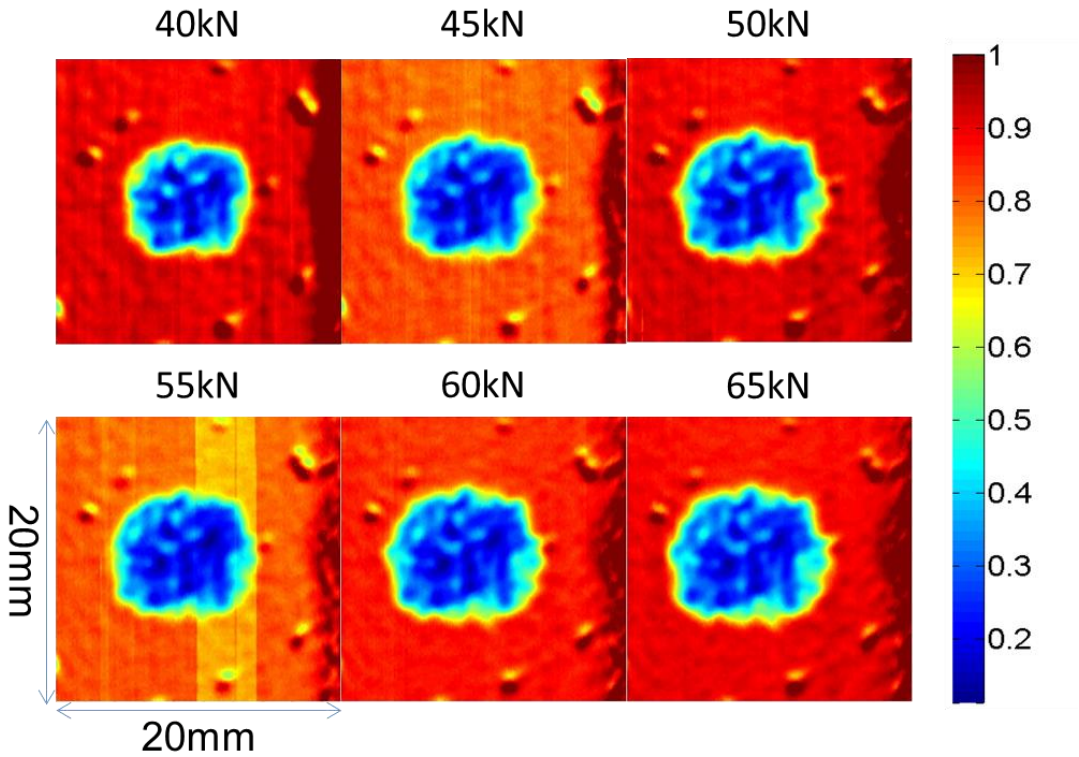

Figure 7.6 Reflection Coefficient Maps of Wheel-Rail Static Contact

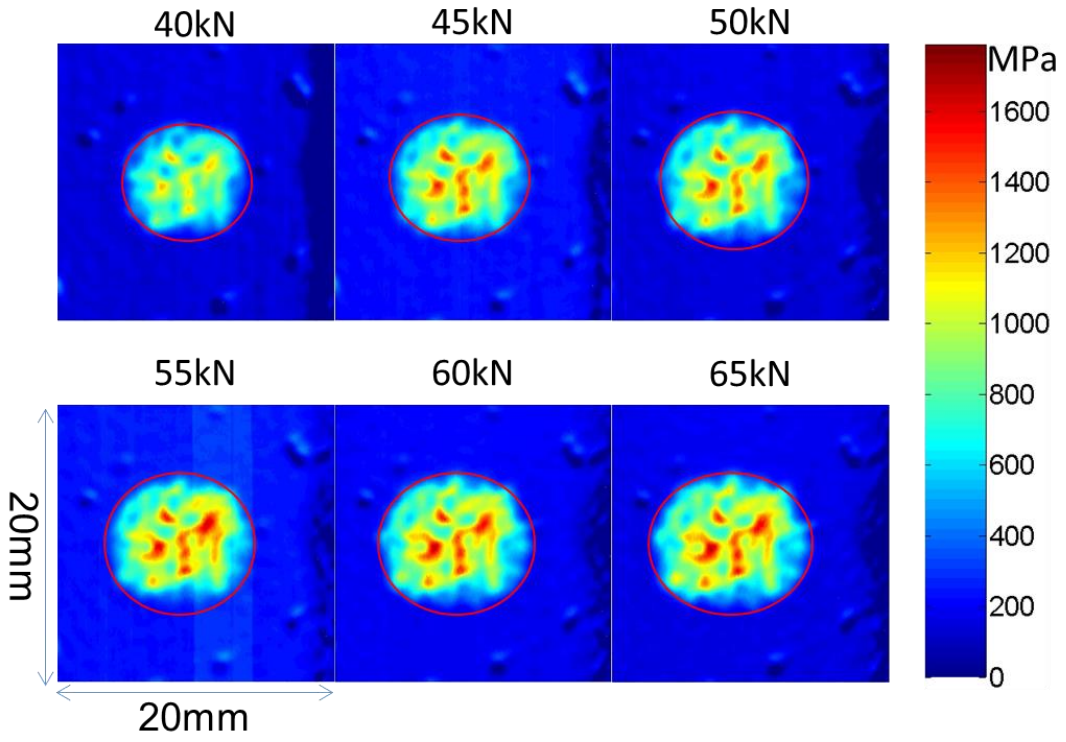

Figure 7.7 Contact Pressure Distributions of Wheel-Rail Static Contact

The simulations from FE are shown in Figure 7.8

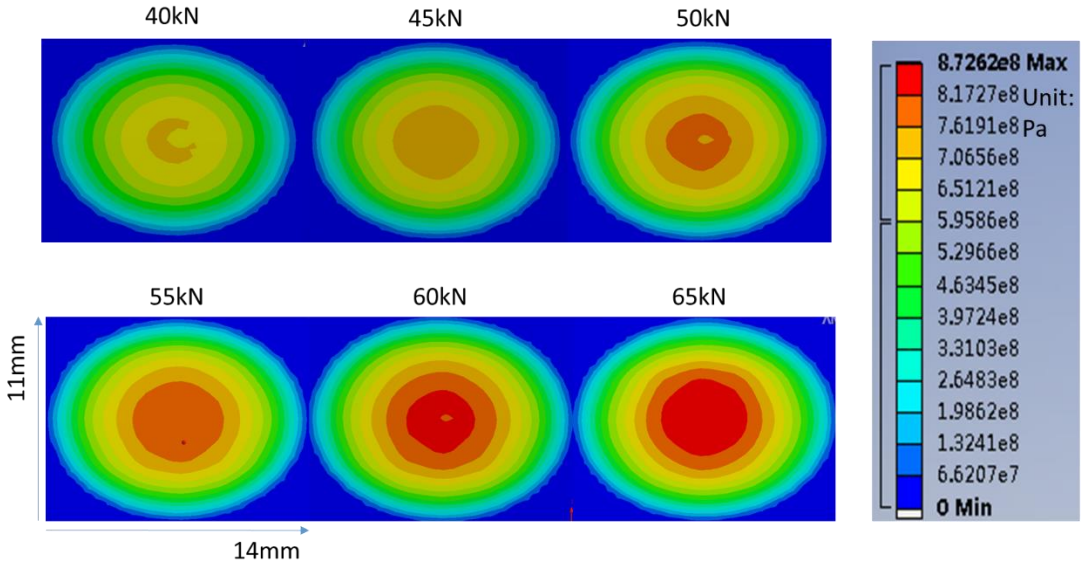

Figure 7.8 FE Simulations of Static Wheel-Rail Contact

7.5.2 Results Comparison

A comparison with finite element model, Hertz theory and ultrasound reflectometry was made. Maximum contact pressure of the series of loads from different methods is tabulated in Table 7.1.

	Loads (kN)	40	45	50	55	60	65
Maximum Contact Pressure (GPa)	Hertz	0.915	0.953	0.987	1.018	1.048	1.077
	Ultrasound	1.256	1.520	1.521	1.648	1.678	1.786
	Finite Element	0.693	0.734	0.772	0.807	0.841	0.873

Table 7.1 Max Contact Pressure of Wheel-Rail Contact Using Hertz, Ultrasound Reflectometry and Finite Element Analysis

Contact patch semi-axes are tabulated in Table 7.2.

	Loads (kN)	40		45		50		55		60		65	
		a	b	a	b	a	b	a	b	a	b	a	b
Contact Geometry (mm)	Hertz	5.3	3.9	5.6	4.1	5.8	4.2	6.0	4.4	6.2	4.5	6.3	4.6
	Ultrasound	5.1	3.2	5.4	3.5	5.6	3.7	5.7	3.9	6.0	4.1	6.0	4.3
	Finite Element	5.3	4	5.4	4.1	5.5	4.2	5.7	4.3	5.8	4.4	5.8	4.5

Table 7.2 Ellipse Semi-axes of Contact Patch of Wheel-Rail Contact Using Hertz, Ultrasound Reflectometry and Finite Element Analysis

Further, mean contact pressure of three methods are compared in Table 7.3

	Loads (kN)	40	45	50	55	60	65
Maximum Contact Pressure (GPa)	Hertz	0.610	0.635	0.658	0.679	0.699	0.718
	Ultrasound	0.719	0.803	0.827	0.851	0.879	0.892
	Finite Element	0.606	0.647	0.689	0.714	0.748	0.792

Table 7.3 Mean Contact Pressure of Wheel-Rail Contact Using Hertz, Ultrasound Reflectometry and Finite Element Analysis

7.5.3 Discussion

According to Table 7.1, for all three methods, the maximum contact pressure grew as the load increased, the growth was relatively steady in Hertz predictions and FE simulations, and ultrasound measurements were covering a wide range of pressures overall. Besides it could be seen that maximum contact pressure from the ultrasound technique is always the highest at all loads applied and pressure from FE simulations is always the lowest. This is because in ultrasound measurements, it was the asperity contacts that were measured, and the asperity contacts were much smaller than nominal contact area, leading to stress concentrations around the peaks, which were higher than average pressure and were detected by the ultrasound. But in Hertz predictions and FE simulations, the wheel and rail surfaces were treated as absolutely smooth, which means no asperity contacts exist and the entire nominal contact area were used to calculate the contact pressure. It should be noted that although surface roughness can be simulated in FE, but it would take an enormous amount of time and work, which is beyond the topic of this thesis. Here the FE is used as a validation of the ultrasound method. Meanwhile, compared with other two methods, the ultrasound measurements were suffering more influences and each single measurement taken had more or less randomness, therefore the peak pressure under 45kN were very close to peak pressure under 50kN and did not fit the growing trend quite well, but the overall pressures were lower than results under 50kN load. On the contrary, the Hertz predictions are analytical solutions and the FE simulations were using one algorithm. In both methods the normal load was the only changing parameter, so the pressure growth were more steady and regular. Plus, the pressures from FE under all loads were lower than Hertz, this is because in FE simulations, a small amount of surface penetration took place.

As with the nominal contact size, elliptical semi-axes obtained from three approaches were all growing steadily. Because the randomness issue in peak contact pressure measuring for the ultrasound method did not affect much in nominal contact area determination, the contact area growth was also smooth as the rest two methods. The contact sizes from ultrasound measurements were slightly smaller than those from Hertz, and sizes from FE were around 15%, this can also be explained by the surface penetration in FE. When one surface penetrated a little into another, a larger area would be regarded as a contact region. By multiplying the contact areas using the semi-axes

and the peak contact pressures for Hertz and FE respectively, the results match each other well.

The difference between three methods in terms of mean pressure is much smaller than that of peak pressure according to Table 7.3. But the influence of detecting high stress concentration using ultrasound reflectometry can still be seen, and the contact patch from ultrasound reflectometry is slightly smaller than the other two methods, leading to mean pressure generally larger than Hertz and FE.

7.6 Summary

In this chapter the static wheel-rail contact was investigated. Contact pressures and contact sizes are characterized using ultrasound, and the finite element method. Although similar tests were carried out by Marshall et al [26]. using the scanning tank and ultrasonic probe, with the upgrade of the scanning program and hardware, images showing the contact patches with higher resolution and better quality have been acquired from the tests here. Results from ultrasound technique and finite element method were compared with Hertz predictions. Contact patches were single ellipses and contact pressure distributions followed ellipsoid pattern as well for all methods. Peak pressures from ultrasound reflectometry were much higher than those from other two methods due to the asperity contacts, average pressures of a certain area can be considered as a better comparing index in the future work.

Chapter 8:

Characterisation of Wheel-Rail Dynamic Contact using Ultrasound

8.1 Introduction

The contact condition between the wheel and the rail is paramount to the lifespan, safety and smooth operation of any rail network. The wheel/rail contact condition has been estimated, calculated and simulated successfully for years, but accurate dynamic measurement has still not been achieved. Current methods using pressure sensitive films [10] and controlled air flow [9] have been employed, but are both inevitably changed the contact conditions. Therefore currently there is not a practical measuring technique which can characterise dynamic wheel-rail contact.

The ultrasonic reflectometry method being a non-destructive measuring technique, which has been proved successful in characterising a variety of static machine element contacts such as ball-on-flat, bolted joints [29], wheel-rail contact [26]. The static scanning tests of ball-on-flat and wheel-rail contact using ultrasound have also been carried out in this research topic (Chapter 4 and Chapter 5). Besides, pilot study of dynamic ultrasonic measurements has been introduced by scanning over a quasi-static wheel-rail contact [32]. Ball-on-flat dynamic contact has been investigated in Chapter 4 as well. The ultrasonic scanning probe used for static measurements is no longer applicable in dynamic tests, the 64-element ultrasonic array was applied. The wheel-rail dynamic contact tests were carried out in a full scale wheel-rail test rig.

8.2 Experimental Details

8.2.1 Apparatus

A full-scale wheel-rail wear test rig (shown in Figure 8.1) was used to carry out the tests. The rig is hydraulically driven and can apply a vertical load up to 200kN. A wheel (5) is suspended on an axle which rotates with two journal bearings located in a loading frame (2) and can rotate freely, the vertical actuator (1) is used to simulated axle weight acting on the wheel, a rail section (6) is fitted and clamped at the bottom into a sliding bed with an inclination of 1 in 20. The rail is driven by a ring main system (3) and can be pulled and pushed longitudinally, the wheel rotates due to friction as the rail moves.

Figure 8.1 Full Scale Wheel/Rail Wear Test Rig (1: Vertical actuator; 2: loading frame; 3: Longitudinal Driving System; 4: Lateral Ram; 5: Wheel; 6: Rail)

8.2.2 Test Conditions

The wheel is a full-size standard 920mm diameter R7 wheel with a worn p8 profile. A 1200mm long UIC60A rail section is used. As described in Section 8.1, the wheel rolls over the rail as the rail is pulled, during one pass the wheel rotates about 1/3 of a full revolution. For the experiments introduced here, a 200mm long rolling path was used as test zone. During the testing period, the wheel is lowered on the rail by a vertical ram and loaded up, the rail is pulled forward along longitudinal direction so that the wheel is able to roll over the rail in opposite direction due to friction. After one pass, the rail is pushed backward and the wheel rolls reversely, in this way two measurements are taken. Since there is no constraint mechanism for wheel lateral movement, the contact position between wheel and rail is not fixed, there is a 2mm-3mm lateral displacement throughout one pass. Therefore, the initial contact is tread contact, but can extend to near the flange area at the end.

8.2.3 Test Equipment

A 64-element ultrasonic scanning array was used for taking measurements, the array has 8 channels, and each channel consists of 8 ultrasonic pulsing elements, all the elements are arranged in a line, as shown in Figure 8.2. The array is 42mm long and actual pulsing length is about 40mm.

Figure 8.2 Ultrasonic Scanning Array and Multiplexor

A hole was machined on the testing rail specimen to fit the array in. A holder was made to clamp the array in position while taking measurements. The hole is located about 1/3 of the way along length from the starting point along longitudinal direction, as shown in Figure 8.3.

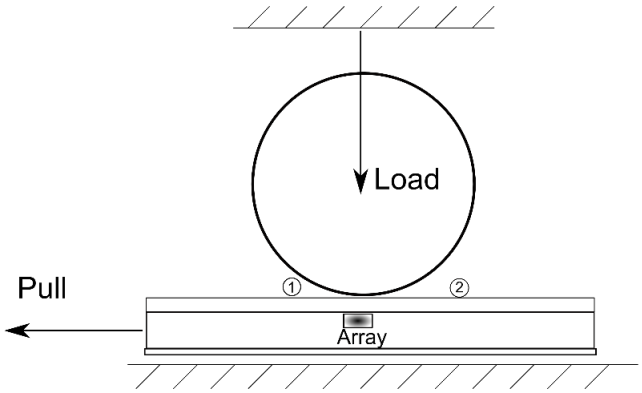

Figure 8.3 Array Longitudinal Fitting Position

In terms of lateral position, since the array is shorter than the width of railhead, it is impossible for the scanning area to cover the whole railhead. But with proper fitting, the array is enough to capture all the contact information as shown in Figure 5.

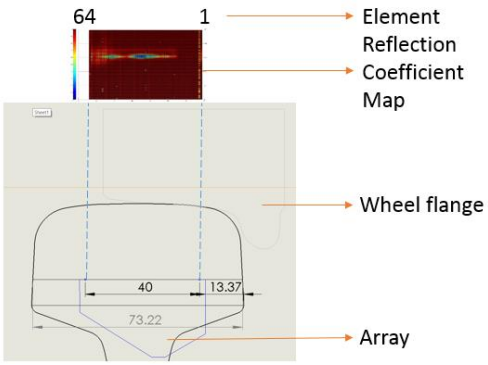

Figure 8.4 Array Lateral Fitting Position

8.2.4 Data Acquisition & Post-Processing

Once the full-scale rig and the scanning array has been set-up, a measurement can then be carried out. The ultrasound incident signals and reflected signals are displayed in a group of 8 (one channel) on the oscilloscope with respect to time latency. Fast Fourier Transformation (FFT) of signals is applied to eliminate multi-frequency interference and acquire better data. The reflected signals from contact region are zoomed in and highlighted, peak to peak value of each signal was recorded continually as test proceeds (Figure 8.5).

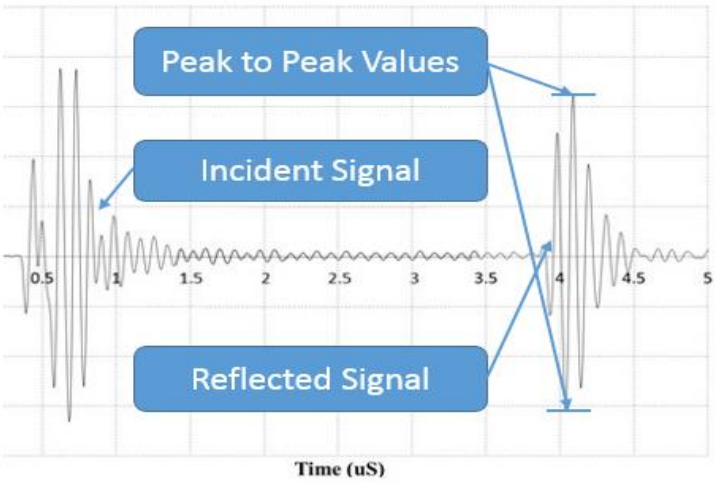

Figure 8.5 Ultrasound Signals on Oscilloscope

One channel can pulse and take measurements a couple of times during one switching cycle, recorded data for each channel are averaged and arranged in a way synchronised to physical display of transducers in the array. After that, a row of data which are measured outside the contact region is chosen as reference, reflection coefficients can be acquired by dividing all the data with corresponding reference, a map of reflection coefficients can then be plotted against time as shown in Figure 8.6.

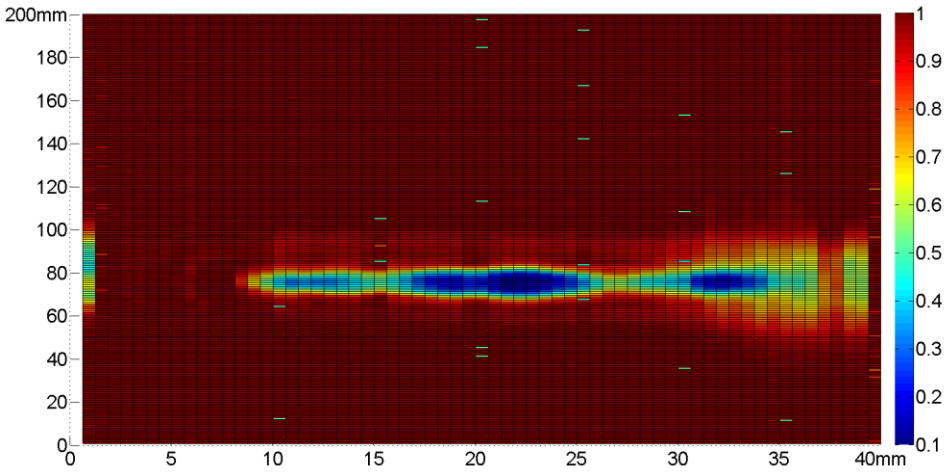

Figure 8.6 Typical Reflection Coefficient Map

As it is mentioned in ultrasound principle section, for two bodies with similar or same materials in contact against each other, the contact stiffness K can be determined by equation (3), $|R|$ can be obtained by dividing the amplitude of reflected signals by that of incident signals.

A series of calibration tests were carried out by Marshall et al. [26] with different pairs of wheel-rail surface roughness: unused, worn tread, worn flange and sand damaged. A calibration curve was plot and linear relationship between contact stiffness and contact pressure was obtained for each case respectively. For the worn tread case that applies here, the relationship is:

$$p = 123K \tag{8.1}$$

Contact pressure maps can thus be plotted out as Figure 8.7.

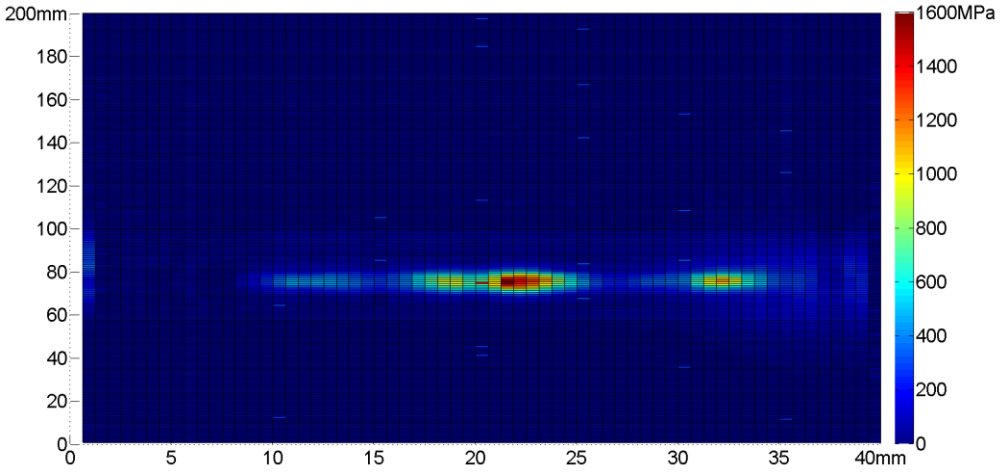

Figure 8.7 Typical Contact Pressure Map

The x-axis and y-axis refer to 64 elements and time respectively. The resolution of the x-axis is limited to physical arrangement of elements and fixed at 64; resolution of the y-axis is related to switching speed of multiplexor and rolling speed of the wheel, the higher the switching speed or the lower the rolling speed is, the better the resolution can get, The switching speed in tests here was 10Hz.

It should be noted that although the array is kept still measuring at one area of the railhead, according to the principle of movement relativity, the whole test can be regarded as the array swiping over the entire test length with the wheel rolling over a static rail at the point where the array is actually located. Therefore, the x and y-axis in the contact pressure map can be translated to actual longitudinal and lateral test length. Hence the contact pressure distribution can be displayed in a more straightforward way.

8.2.5 Results

A series of measurements were taken under different loads and rolling speeds. The test started with a load of 40kN at a rolling speed of 1mm/s, and then the load was increased 20kN each time up to 120kN (mass of the wheel had been taken into account). Figure 8.8 shows a pair of the full scans at 40kN and 1mm/s, the contact can be seen 1/3 of the

way along the test length as would be expected. The maximum contact pressure is 678MPa and 739MPa respectively, and for all the loads, maximum contact pressure taken from forward and backward tests differ no more than 10%, and around 5% in average.

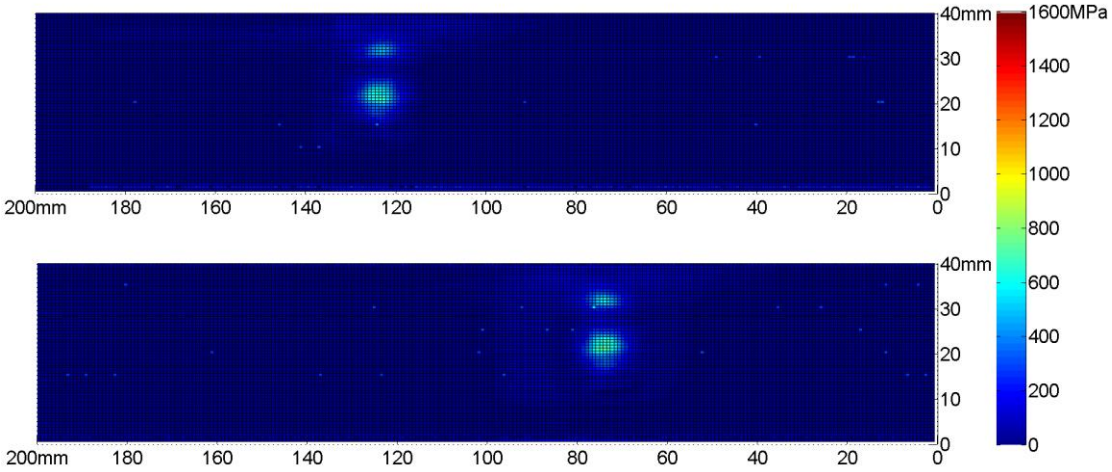

Figure 8.8 Full Contact Pressure Maps of Wheel-Rail Rolling Contact under 40kN Load at 1mm/s

Figure 8.9 shows a series of contacts under the speed of 1mm/s with increasing loads applied. From the results it can be seen that contact area as well as contact pressure grows with increasing load. The contact patch grows from one side to the other and the main contact area splits into two as the load increases.

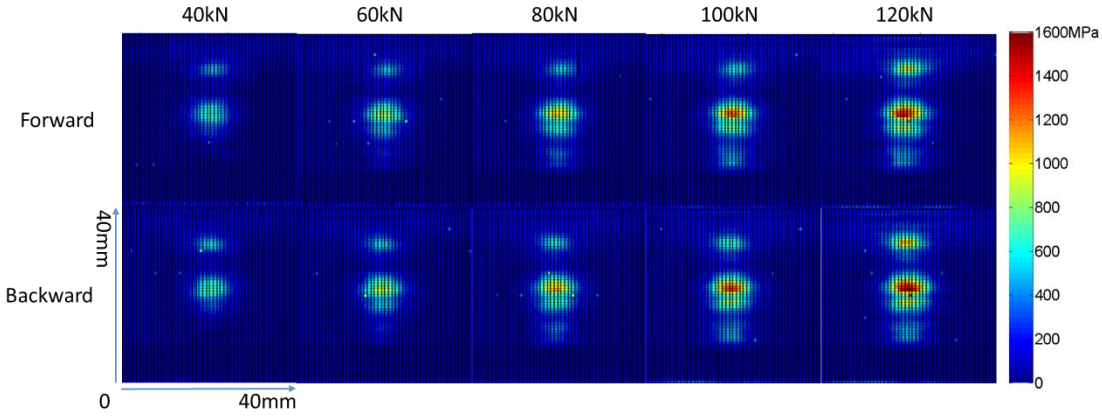

Figure 8.9 Contact Pressure Maps of Wheel-Rail Rolling Contact at 1mm/s (Top: Rolling Forward; Bottom: Rolling Backward; From Left to Right: 40kN, 60kN, 80kN, 100kN, 120kN)

Results from the same load, but inverse rolling direction match with each other very well in terms of contact area as well as pressure distribution. This indicates that the array is capable of producing consistent, repeatable measurements

Tests at a rolling speed of 5mm/s were carried out later with same loads applied, the array was moved about 3mm along lateral direction compared with first tests. Figure 8.10 shows a pair of the full scan for area at 40kN and 5mm/s.

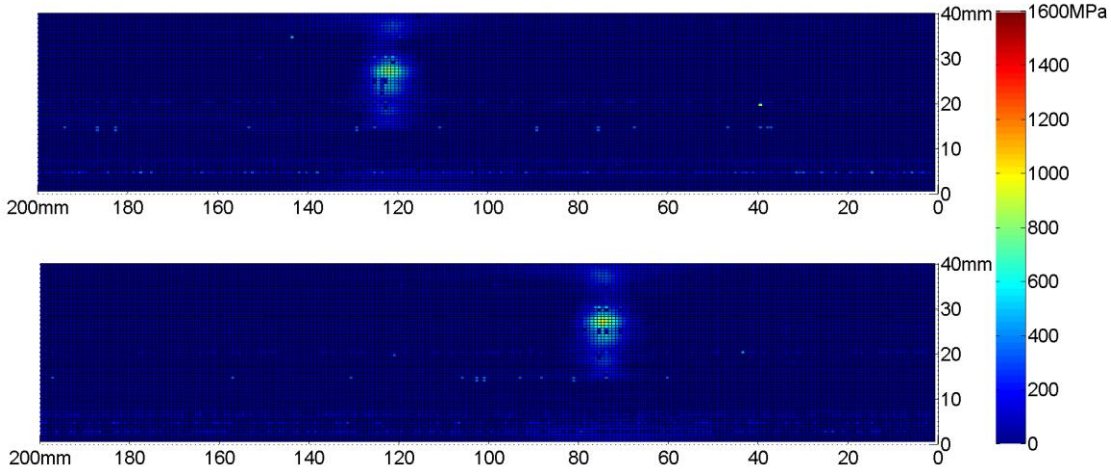

Figure 8.10 Full Contact Pressure Maps of Wheel-Rail Rolling Contact under 40kN Load at 5mm/s

Figure 8.11 show a series of contacts under the speed of 5mm/s with increasing loads applied.

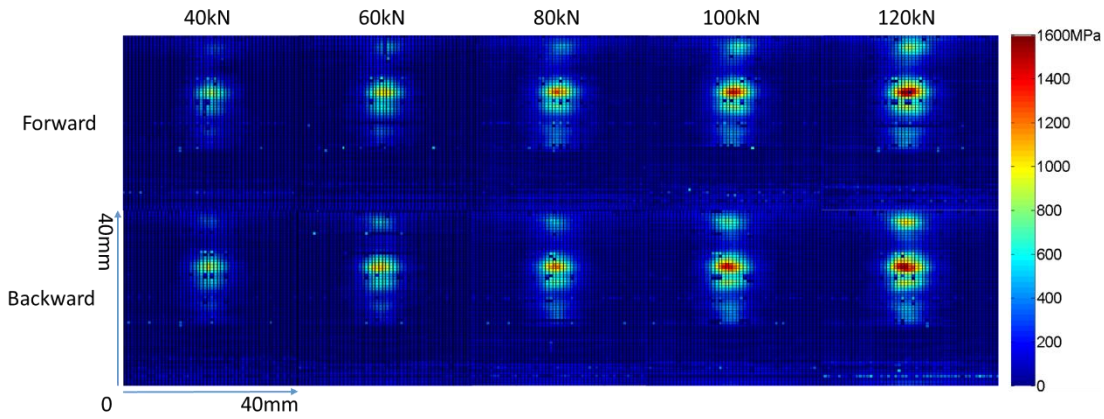

Figure 8.11 Contact Pressure Maps of Wheel-Rail Rolling Contact at 5mm/s (Top: Rolling Forward; Bottom: Rolling Backward; From Left to Right: 40kN, 60kN, 80kN, 100kN, 120kN)

8.2.6 Discussion

8.2.6.1 Analysis of Ultrasound Results

Compared with pressure maps of 1mm/s tests, more "defective" cells are observed in 5mm/s results. This is because less information was recorded in the same time as the

rolling speed increased, which led to insufficient data for averaging. However, results from 5mm/s still have enough information for each contact generally: contact patches look almost the same as the corresponding ones in 1mm/s tests; contact pressure distributions also match quite well. Maximum contact pressure and contact area are plotted against load for tests at the two speeds, as shown in Figure 8.14. Since the difference between results from forward and backward tests is acceptable, only data from the forward tests is plotted.

From the results it can be seen that contact area as well as contact pressure grows obviously with increasing loads. A double contact is seen at the beginning; the contact patch grows from one side to the other laterally, the main contact area split into two as the load increases, which results in triple or even quadruplet contact. Results from same load but inverse rolling direction match with each other very well in terms of contact area as well as pressure distribution. This indicates that the array is applicable for duplicative tests in the long run.

Compared with pressure maps of 1mm/s tests, more "bad" points are observed in 5mm/s results. This is because less information was recorded in a same time as the rolling speed increased, which leads to insufficient data for averaging, transmission data which ought to be ignored were inevitably taken into account. However, results from 5mm/s still have enough information for contact generally: contact patches look almost the same as corresponding ones in 1mm/s tests; contact pressure distributions also match quite well.

In a 2-dimensional plot, the "visible" contact patches (for example as shown in Figure 8.7) are larger than the actual nominal contact areas. This is because the ultrasonic array is working by taking averages of all data in the region it is interrogating, and this region cannot be infinitely small, the boundary between the contact area and non-contact area is not a clear line, but a transmission area, which is noted as the "blurring" effect; Another reason is that there are elements scanning areas close to the rail edges which have curved profile. As the load increases, the rail will deform, and any tiny deformation around the rail edges will result a large amplitude drop of reflected signals, and this effect is also captured in the 2-D plots. To determine the area, a decision must be taken on where, in terms of contact pressure, to filter out data around the contact zone. As shown in Figure 8.13, for wheel-rail contact under all loads, the contact area drops continuously with the bottom limit pressure going up. The contact pressure is calculated from the reflected coefficient, therefore to choose a proper bottom pressure limit, a confidence interval of reflection coefficients must be decided to distinguish contact area and non-contact area. From equation (2.4) and equation (2.5), the bottom pressure limit P_{btm} is calculated as:

$$p_{btm} = 123 \times \frac{\omega z}{2} \sqrt{\frac{1}{|R_{top}|^2} - 1} \tag{8.2}$$

Figure 8.12 shows the distribution of reflection coefficients in lateral direction under 40kN load.

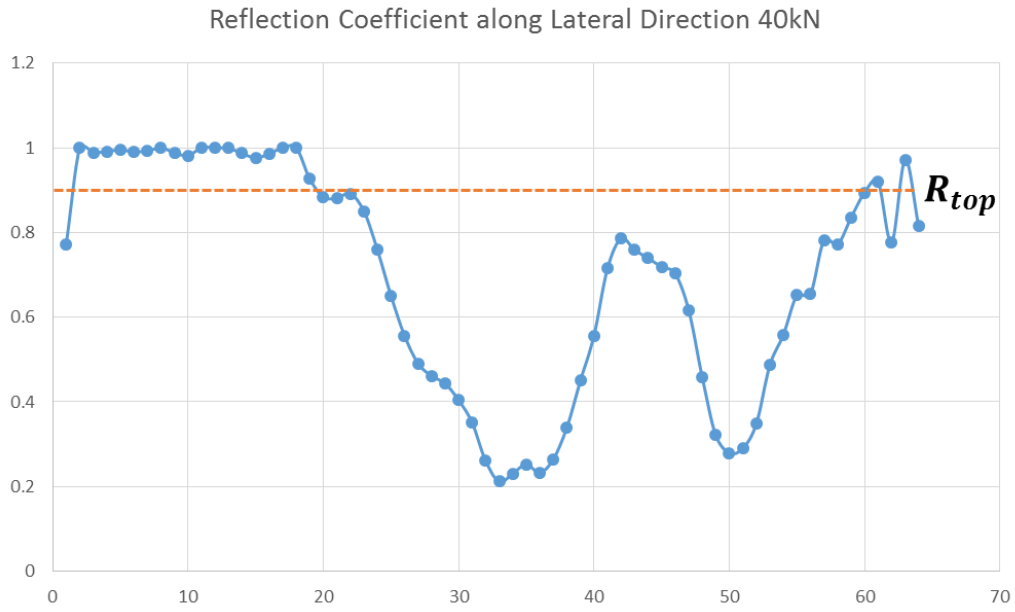

Figure 8.12 Reflection Coefficient along Lateral Direction

from the Figure 8.12, it is debatable but safe to pick the cut-off reflection R_{top} as 0.9, through equation 8.2, p_{btm} is determined as 77.6188MPa, and this bottom limit is only for 40kN load test. Therefore it is more reasonable to adopt higher p_{btm} for increasing loads. According to Hertz theory (Equation 3.1 and 3.2), the maximum contact pressure and the average contact pressure are proportional to $P^{1/3}$, where P is the applied load. Assuming the p_{btm} follows the same pattern, the coefficient was set to 1/3 power to the load ratio. Then the p_{btm} for loads from 40kN to 120kN were 77.61MPa, 88.85MPa, 97.79MPa, 105.34MPa and 111.94MPa respectively. From Figure 8.13 the contact area under each load is 285, 322.5, 345, 367.5, and 373mm ²for tests under loads from 40kN to 120kN at the rolling speed of 1mm/s.

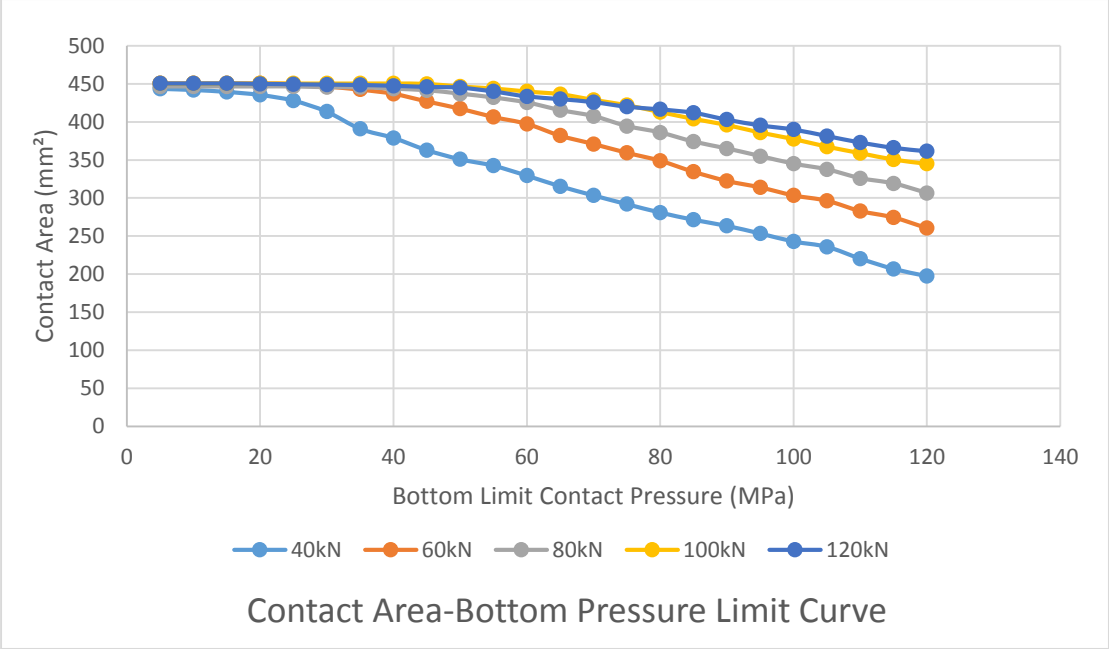

Figure 8.13. The Contact Area-Bottom Pressure Limit Curve under Different Loads for 1mm/s

(Contact area for a rolling speed of 5mm/s can be calculated in the same way)

The p_{btm} can also be used for benchmarking the load. Each single pressure result shown in Figure 8.10 contains 250×64 cells, and area of one cell is 0.5mm^2. By neglecting the values lower than p_{btm} and obtaining the total pressure by summing up all the rest pressure in each cell, the benchmark normal load is the multiplication of the total pressure and area of one cell. In this way, the benchmark load at 1mm/s test and 5mm/s can be seen in Table 8.1

	40kN	60kN	80kN	100kN	120kN
1mm/s	52	78	102	130	156
5mm/s	48	74	100	125	149

Table 8.1 Benchmark Load of Dynamic Wheel-Rail Measurements

The reason why benchmark loads are generally 25% larger than nominal loads applied is that there are still some out of contact measurements taken into account due to noise, signal fluctuations or electrical interference, etc., despite the fact that most have been ignored with the p_{btm}.

As shown in Figure 8.14, the contact areas and maximum contact pressures under all loads are compared with each other, data from forward tests are used.

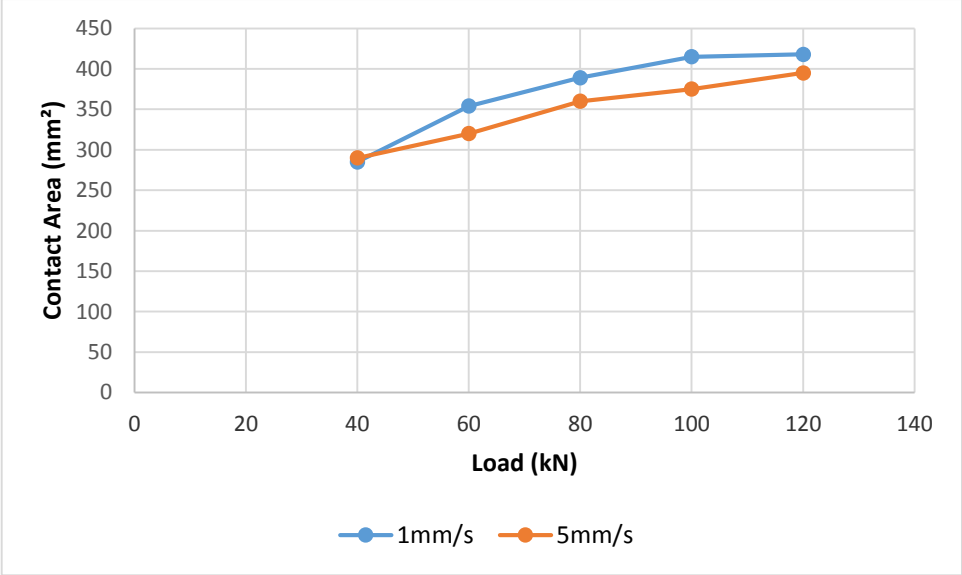

(a)

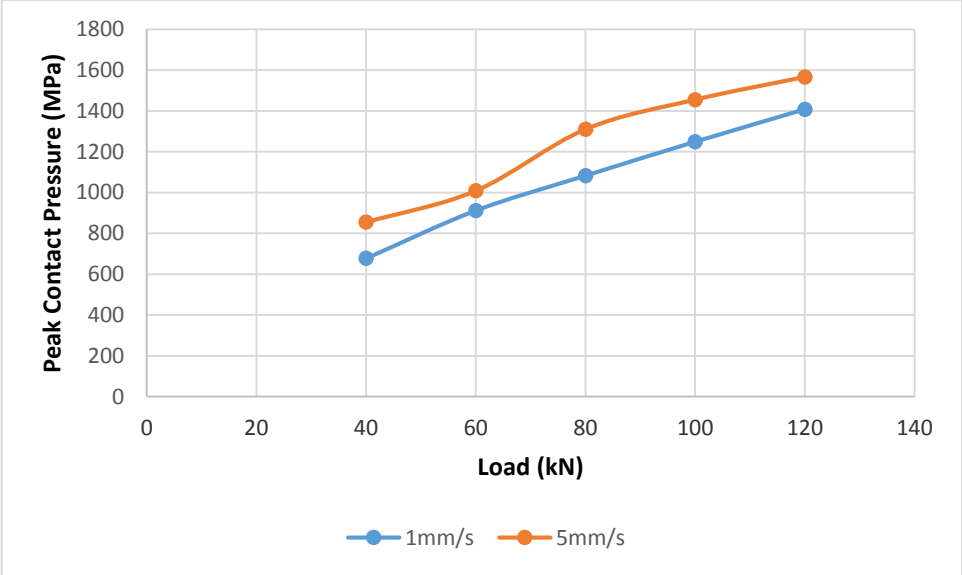

(b)

Figure 8.14: (a) Contact area comparison; (b) maximum contact pressure comparison

8.2.6.2 Finite Element Analysis

A 3-D model of the test specimens was simulated in finite element software. Profiles of the wheel and the rail in dynamic tests were measured using a profilometer, the CAD drawings of the profiles were then imported into modelling software and stretched to 3-D model. Although the real surface conditions cannot be simulated through direct stretching in the software, the influence of worn wheel and rail profile to the contact, however, can be reflected in the simulation. The contact simulated here is static. Similar to what has been done in Chapter 7, CONTAC48 elements were used to model the contact pair, and pure penalty algorithm was used. Initial interfacial stiffness was set to 0.1 and the contact problem was solved iteratively with changing stiffness in each iteration step. The bottom of the wheel specimen was fix supported and the load was applied from top of the rail perpendicular to the rail top surface. Multiple contacts are

also observed in simulation results. The contact pressure distribution appears to be incorrect due to the complexity of worn wheel profile, but the contact shape is available as a reference (shown in Figure 8.15).

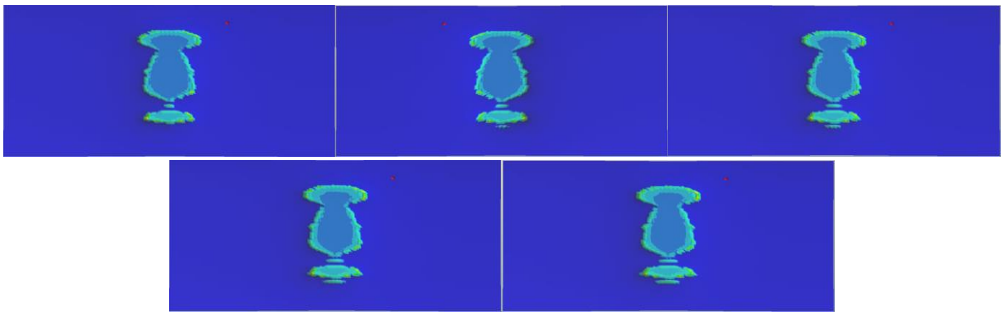

Figure 8.15. FE Simulations of Wheel-Rail Static Contact using the Same Wheel and Rail Profiles (From Left to Right: 40kN, 60kN, 80kN, 100kN, 120kN)

Contact area from the ultrasound measurements were compared that from FE simulations (Table 8.2). The contact area calculations from FE are approximations by separating the contact patch into several regular ellipses.

Load (kN)	40	60	80	100	120
FE (mm^2)	262.75	270.5	275.8	282.4	290
US (mm^2)	285	322.5	345	367.5	373

Table 8.2 Contact Area Comparison

Big differences in contact sizes between FE and the ultrasound technique were found through Table 8.1, especially under high loads. In FE simulations, the results are basically influenced by one changing factor, which is the load, results are normally changing stably and regularly. Besides, the boundary between contact region and non-contact region in FE is relatively clear, but in ultrasound measurements, the boundary are usually blurring. What is more, the way of introducing a bottom limit pressure to distinguish contact area from non-contact area are debatable and probably can be improved for more accurate contact area calculation. Because there was not a criterion to pick the cut-off reflection R_{top} and the wheel-rail contacts characterized were different from Hertz predictions.

Another validation has been taken by applying Fuji contact film. The test was carried out by attaching the film on the rail top surface and the wheel is loaded and unloaded cyclically on the rail. The Fuji film can measure contact pressure up to 300MPa, which is far lower than average pressure of wheel-rail contact. However, as the wheel was loaded over the rail and the covering film, a trace of contact patch will be fully recorded on the film as red color, the contact area as well as the contact patch can be used as validation. Figure 8.16 shows the results comparison from three approaches under

40kN and 100kN. From Figure 8.16 it can be seen that contact patch from FEA and ultrasound measurements consists of multiple smaller contact ellipses. The result from Fuji film, however, was one large red patch because most parts of the contact area has exceeded the top limit of the film. But the nominal contact area from Fuji Film is generally the same as that from ultrasound technique.

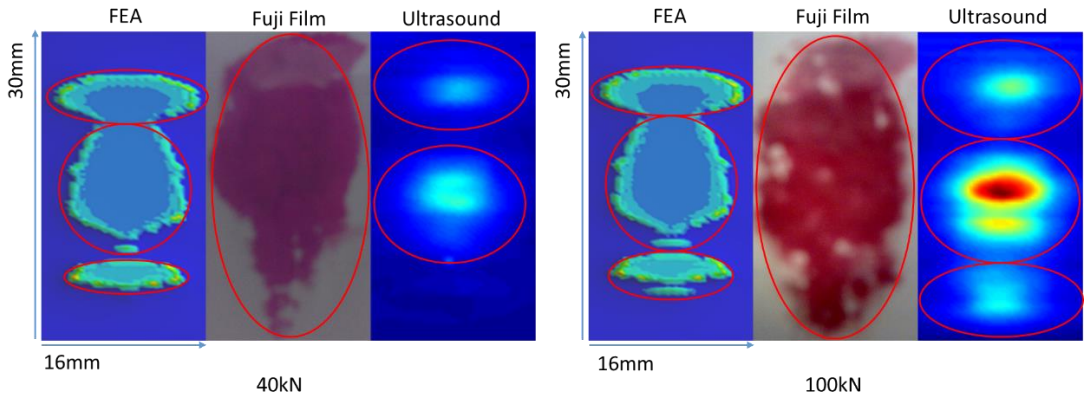

Figure 8.16 Contact patch from Fuji Film and ultrasound measurements (Results from FEA and Fuji Film were static wheel-rail contact and results from ultrasound reflectometry were dynamic wheel-rail contact)

A picture of the tested wheel and rail was taken to show the approximate contact position as shown in Figure 8.17. From the picture it can be clearly seen that the contact position is located in the wheel tread-rail head contact zone. The white line (within the highlighted box) marks the contact "trace" as the wheel rolls over the rail, which gives a reasonable guide to where the contact is.

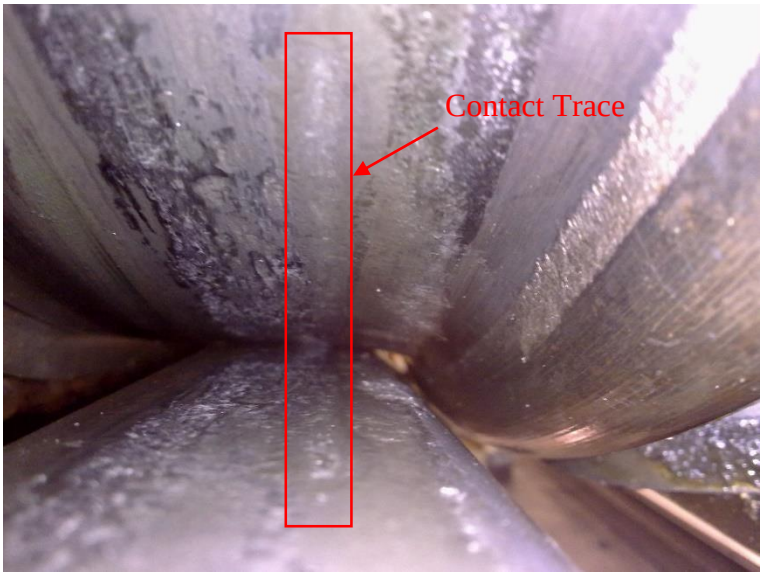

Figure 8.17 Picture of Investigated Wheel/Rail Contact

One contact pressure result was plotted on a 200mm long 3D UIC60A model according to position of the array (Figure 8.18). Compared with real picture, position of the main contact looks roughly the same.

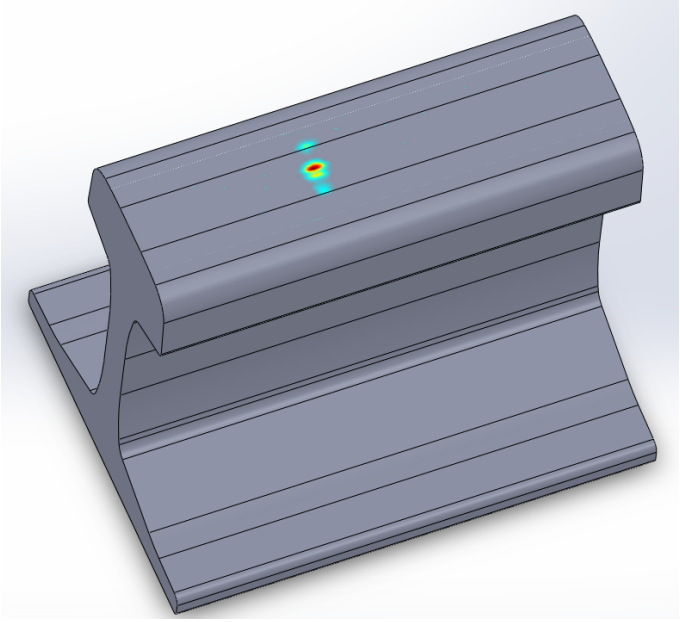

Figure 8.18: Contact pressure displayed on a 1:1 3D rail model

8.3 Summary

The new ultrasonic measuring technique is able to characterise dynamic contact and take real-time measurements using ultrasonic scanning array. Obvious changes in contact area and contact pressure are observed with increasing loads; with the current system the effect of speed change on measurement has been characterized, however results from two speeds both display contact information clearly, which proves the capability of the technique in a range of conditions. Currently the technique has limited capability to measure at high wheel rolling speed, but theoretically measurements can be taken at full line speed with upgraded equipment.

Chapter 9:

Rail Endpost

9.1 Introduction

Tracks are not two lines of continuous steel, but many sections of rails. As shown in Figure 9.1, railway track is divided into short sections of the same length, and neighbouring rail sections are electrically isolated from each other. Each rail section contains an individual electric circuit which consists of a power source and a signal indicator. Under normal situations, the signal indicator is connected to the circuit and the indicator state is marked on. When a train passes over the section, the electric circuit is shorted by the train wheels and axle, the signal indicator is disconnected from the circuit and the state turns off. By examining the states of every indicator and checking which one is off, the place of the train can be located. Because the rail material is conductive, in order to create individual electric circuits, two neighbouring rail sections are connected by insulated block joints, and the endpost is made of nonconductive materials, normally nylon.

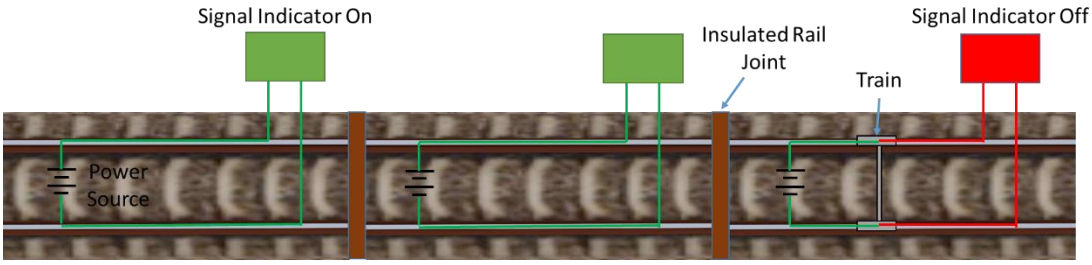

Figure 9.1 Individual Electric Circuits for Location Train Positions

As described above, an insulated rail joint (IRJ) is used to conjunct and insulate two neighbouring rail sections. The insulated rail joint consists of two steel joint bars, which is noted as fishplates. The fishplates are normally fitted onto either side of the rails with a number of bolted joints. As the fishplates are conductive as well, a layer of insulating material is applied to encapsulate the fishplates including the gaps between bolts and bars. Meanwhile, the adjoining rails have a 5mm to 15mm gap in between for insulating. There are some tracks where nothing is placed in to fill the gap, the contact conditions is catastrophic when wheels pass over the gap without any supporting component, so in most cases, an endpost is put in.

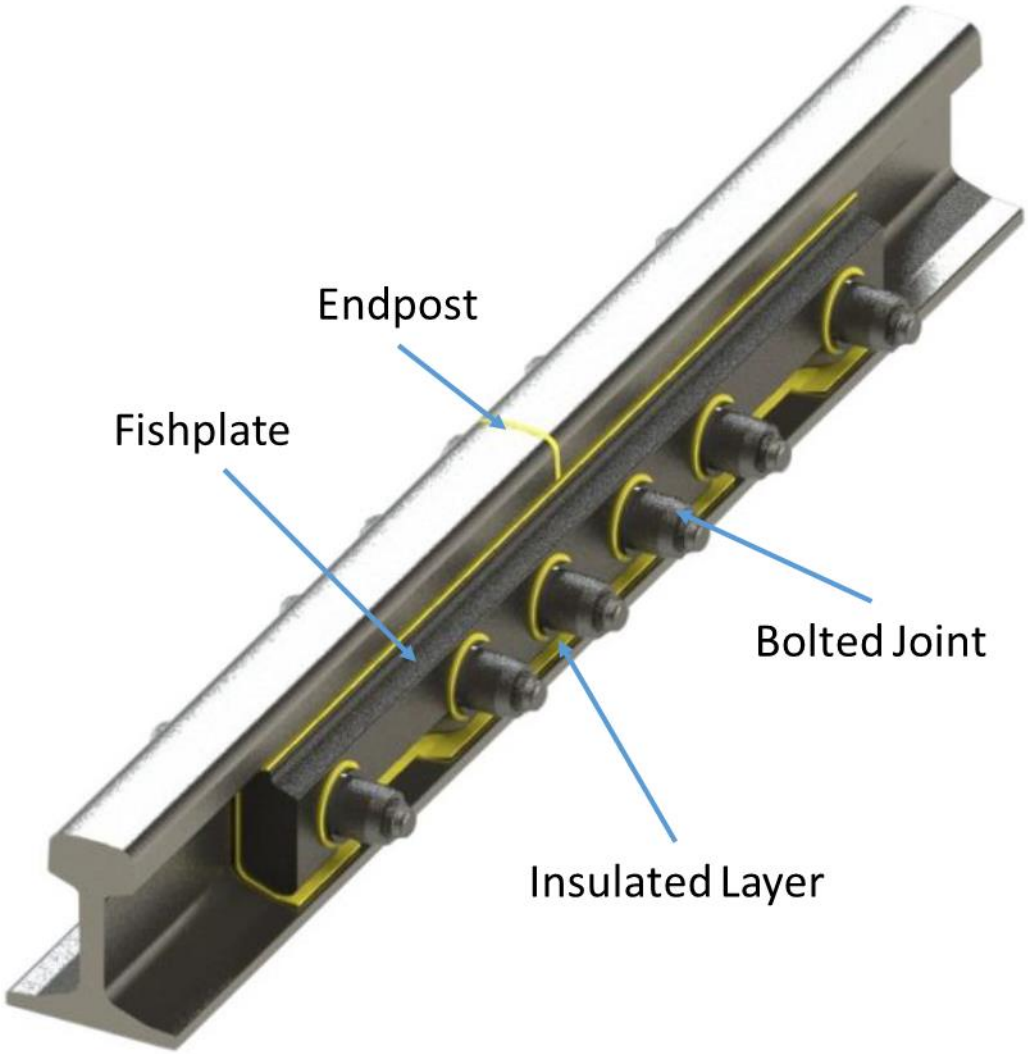

Figure 9.2 Insulated Rail Joints and Endpost

Because of the existence of IRJs, the local strength, especially the bending strength around the rails is lower than that of normal rails.

Due to the discontinuities between two rail sections and the natural properties of nonconductive materials, the contact environment between wheel and rail endpost is harsher than normal conditions. The Young's modulus of rail endpost materials is much lower than that of steel. When the train passes over, the endpost deforms greatly under high normal load. As it can be seen from Figure 9.3, once the endpost deforms, there is a significant height difference between it and neighbouring two rail sections. The weight of the train is burdened by edges of the rail sections, leading to a high stress concentration at the edge. Sandstrom and Ekberg investigated the endpost contact problem using FE simulations [32]. Figure 9.4 shows the contact stress distribution along the longitudinal (rolling) direction from the simulations, it can be seen that there are great stress differences between the rail edges and the endpost. In the long term, the rail edges keep deforming towards the endpost, and squeezing it. Therefore, a variety

of severe failures such as cracks and delamination of endpost, plastic flow of railhead will occur in the periodic loading and unloading process. Getting to know the contact between wheel and rail endpost will help in understanding the failures of the endpost and rail edges to help create a better design and lifespan prediction.

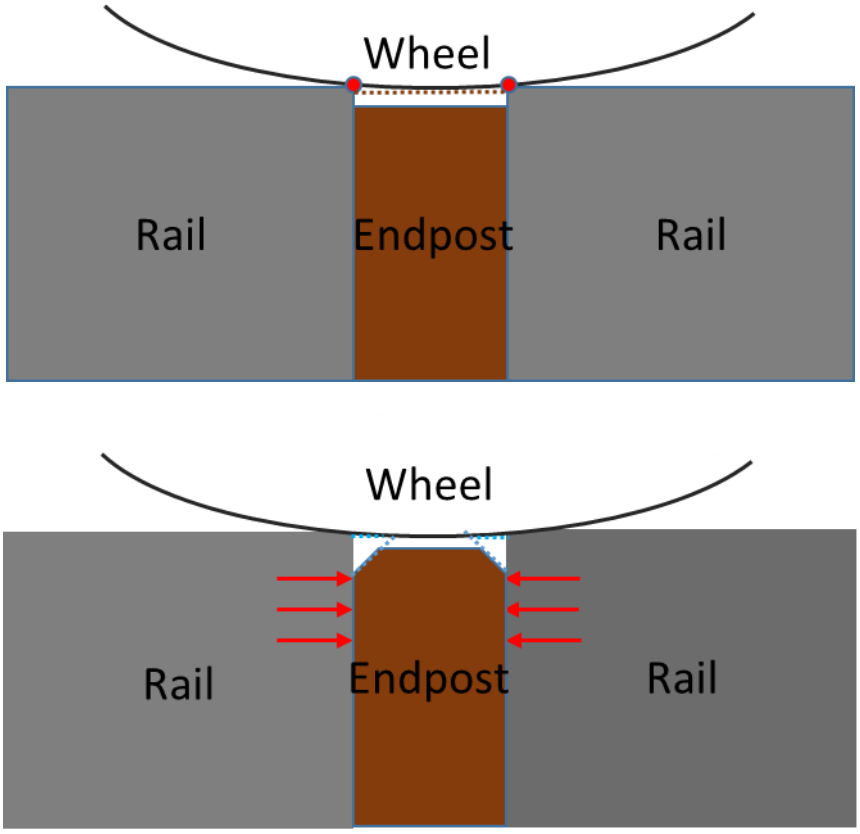

Figure 9.3 Deformation of Rail and Endpost as Wheel Rolls over

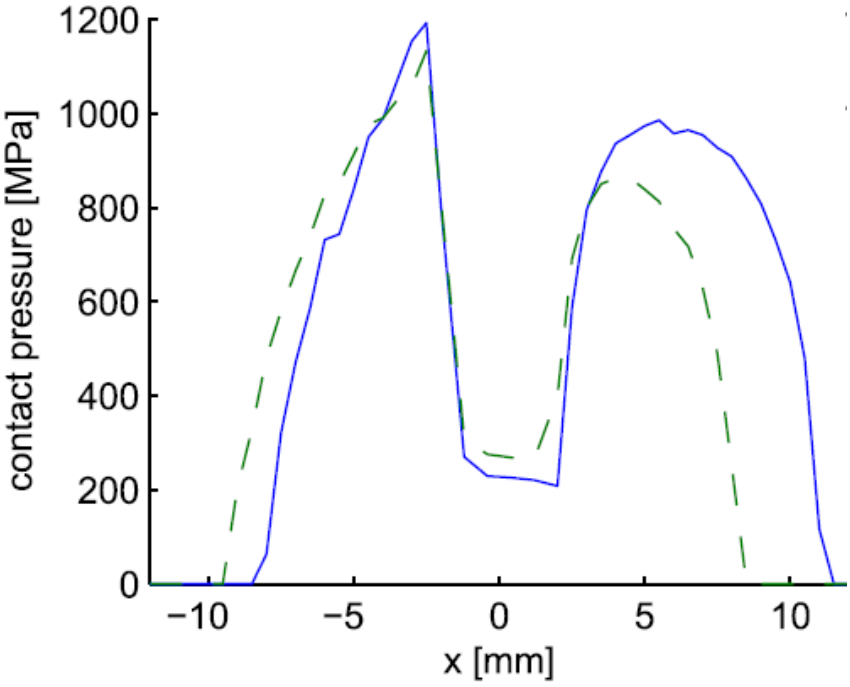

Figure 9.4 Contact Pressure Distribution along the x-axis (Rolling Direction) [32]

In this chapter, an endpost sample was clamped in between two rail specimens and loaded up against a wheel specimen in a loading frame. Ultrasound was used to characterise the contact. There is no previous research of using ultrasound to investigate a contact of combined materials, the study is also helpful in broadening the applicability of ultrasound measurements in various situations. Finite element analysis (FEA) is also used for comparison and validation.

9.2 Experiment Details

9.2.1 Test Objectives

Endposts have a series thickness for varied conditions. Different thickness can lead to significant changes in contact, so it is necessary to test endpost with different thickness. In the tests carried out here, a 6mm thick and a 10mm thick endpost were tested respectively. The Endpost material was Nylon66, which has a density of 1.183g/mm ^{3}, with a Young's modulus of 3GPa. The specimens are shown in Figure 9.5. The wheel specimen is cut from an R7 wheel, and the two rail specimens were cut from UIC60A rail. Both the wheel and the rail specimens were quite worn.

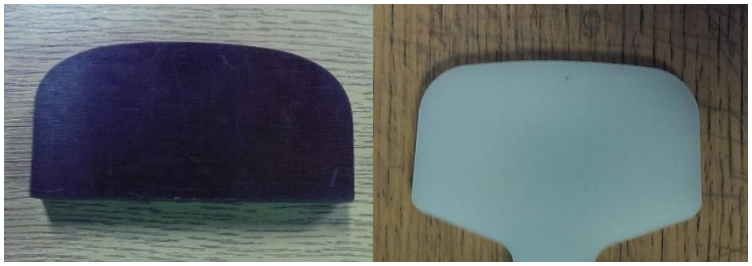

Figure 9.5 Endpost Specimen

The endpost is then placed in between the two rail sections and clamped in a slot to prevent movements (as shown in Figure 9.6).

Figure 9.6 Endpost with Rail Sections

9.2.2 Test Set-up

Because the test is using ultrasound for static measurements, the basic test rigs and set-up was similar as static wheel-rail tests (Chapter 7): the UPR, PC, scanning tank, loading frame and ultrasonic transducer were used here as well. The difference is the wheel specimen is on top and rail parts are at the bottom, otherwise it would be difficult for data processing as the speed of sound is quite different between nylon and steel.

The loading frame was fixed on the scanning tank with clamping blocks and bolts. The specimens were loaded up using a hydraulic jack. After proper sealing, distilled water was poured into the scanning window formed with the wheel top and the frame (as shown in Figure 9.7).

Figure 9.7 Loading Frame and Scanning Window

The ultrasonic probe was sunk into the water couplant to the depth that the ultrasonic signals focus at the contact interface. During the test, the probe moves in the x-y plane and starts pulsing and receiving signals. Through data processing in a PC, a 2-dimensional reflected voltage map can be plotted (as shown in Figure 9.8a). The profile of the wheel was curved, to avoid signal scattering and attenuation in the material and at the surface, a reference test was taken by scanning the same area without contact or load (shown in Figure 9.8b). And then a map of reflection coefficient could be acquired (as shown in Figure 9.8c).

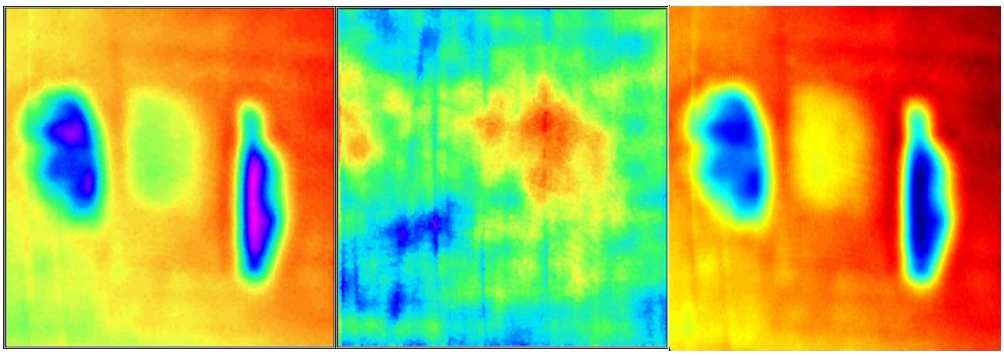

(a) (b) (c)

Figure 9.8 (a) Maps of Reflected Voltage (b) Reference (c) Reflection Coefficient

9.2.3 Ultrasound Scanning Results

A series of loads were applied from 30kN to 80kN every 10kN for both 10mm endpost tests and 6mm endpost tests. Figure 9.9 and Figure 9.10 shows reflection coefficient maps of 10mm endpost contact tests. Small displacements are still inevitable due to vibrations of the scanning tank, but this should not be a problem as long as all the contact information is captured.

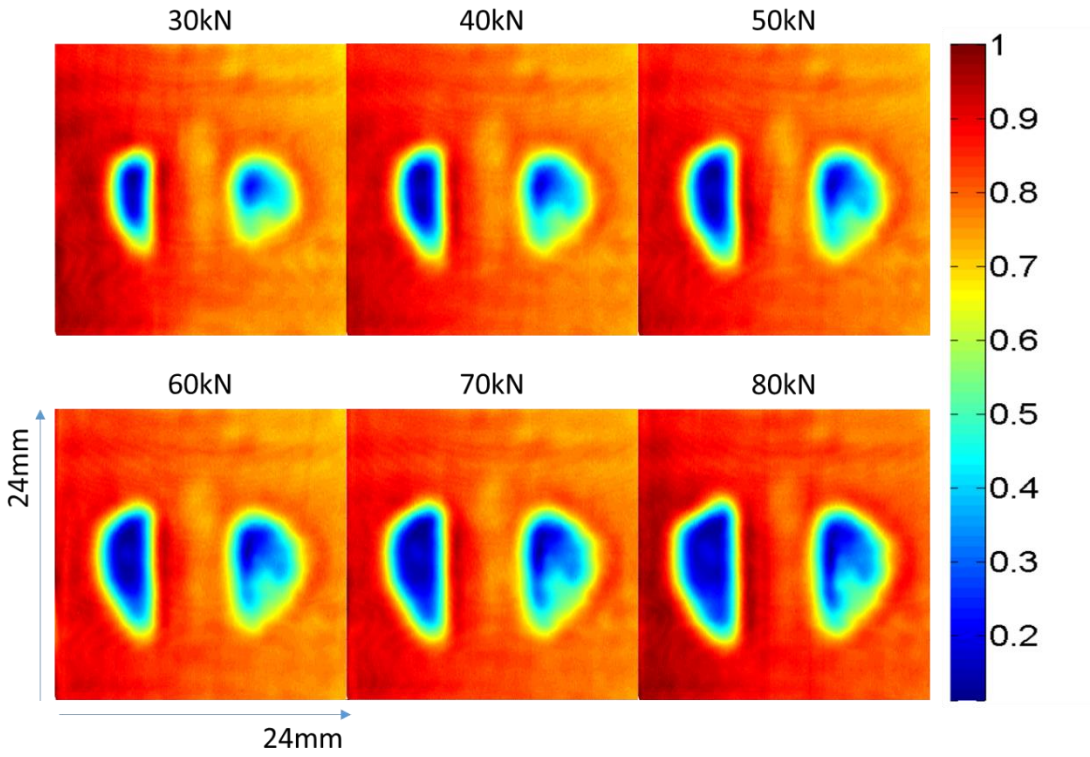

Figure 9.9 Reflection Coefficient Maps of 6mm Endpost Static Tests

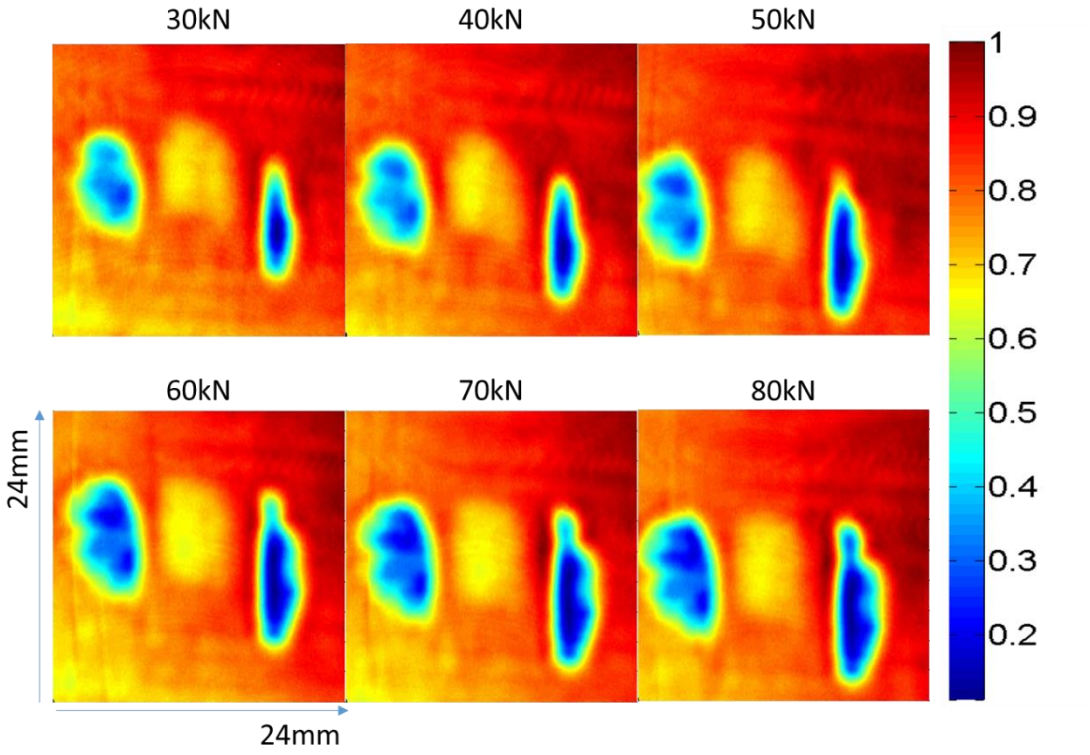

Figure 9.10 Reflection Coefficient Maps of 10mm Endpost Static Tests

Since the tests were scans over combined materials, the contact patch should be divided into three parts: wheel-rail (left), wheel-endpost, wheel-rail (right) for further processing. Both the speed of sound and density of Nylon is smaller than those of Steel, therefore the acoustic impedance of Nylon is smaller than that of Steel. According to Chapter 4, steel-steel contact should follow equation 4.4 and steel-nylon contact should refer to equation 4.3. Thus from equation 4.3 and 4.4, we can derive the interfacial stiffness K through:

$$K = \frac{\omega z_1}{2}\sqrt{\frac{1}{|R|^2} - 1} \tag{9.1}$$

for wheel-rail contact, and:

$$K = \omega z_1 z_2 \sqrt{\frac{1-|R|^2}{|R|^2(z_1+z_2)^2-(z_1-z_2)^2}} \tag{9.2}$$

where z_1 and z_2 are acoustic impedances of steel and nylon respectively, $|R|$ is the modulus of the reflection coefficient, $\omega = 2\pi f$ is the angular frequency. Through equation 9.1, contact stiffness maps can be plotted for wheel-rail parts. Considering the wheel and rail specimens were worn, the relationship between contact pressure P and contact stiffness K is $P=123K$ [26], contact pressure maps of the rail sections were plotted for both 6mm and 10mm endpost tests (as shown in Figure 9.11 and Figure 9.12).

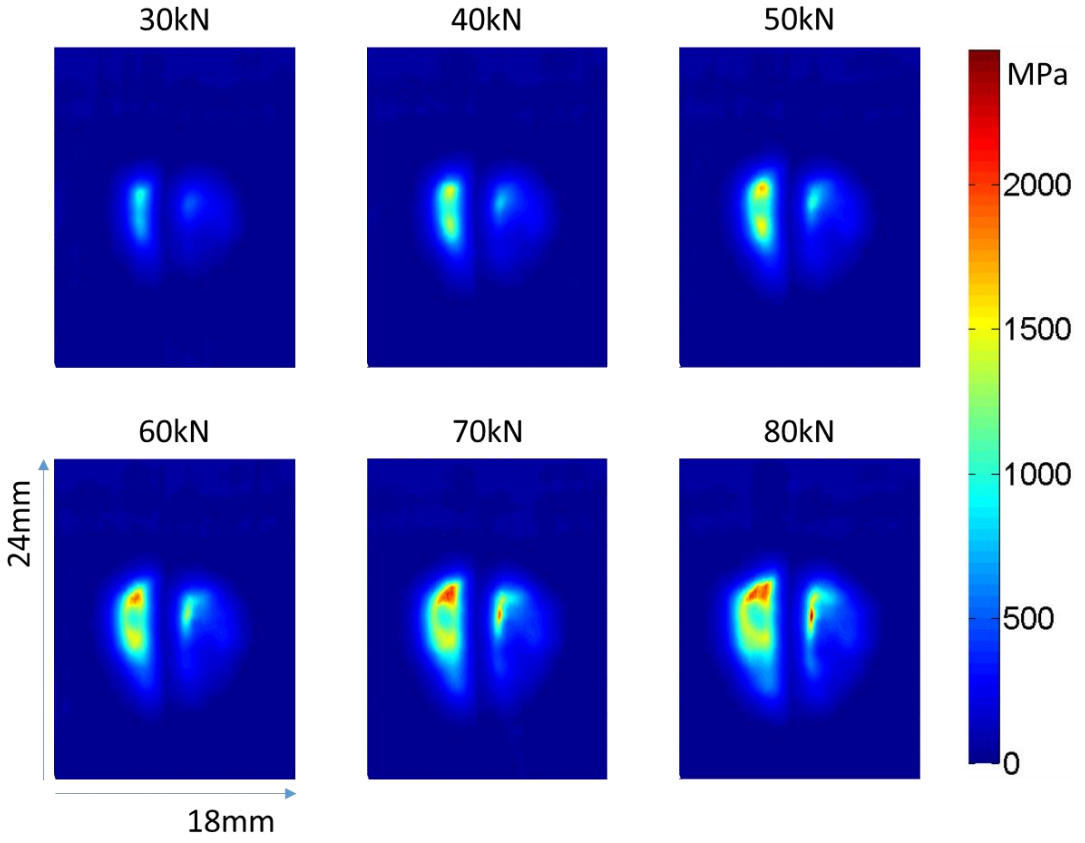

Figure 9.11 Contact Pressure Maps of Rail Sections with 6mm Endpost (Static)

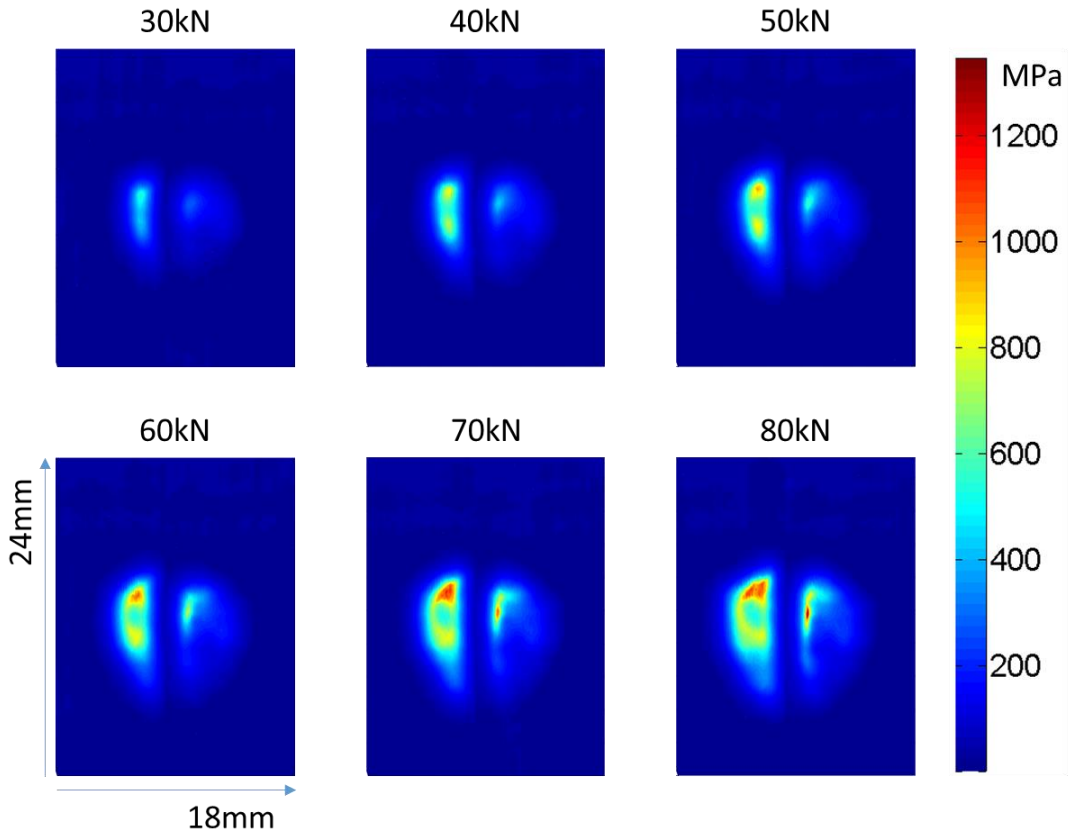

Figure 9.12 Contact Pressure Maps of Rail Sections with 10mm Endpost (Static)

For both 6mm and 10mm endpost tests, it can be seen from Figure 9.11 and Figure 9.12 that contact patches of the rail section on the two sides are not the same. This is because there are tiny tolerances between the bars of the loading frame and the mid-loading plate. Hence the plate will incline a bit when it is loaded, leading to an unsymmetrical loading of two sides. Another thing which needs to be mentioned is that the scanning area is determined by pre-configuration in the scanning software and is always fixed for one series of tests, but during the scanning process or loading and unloading between two tests, the specimens were although clamped in some ways, but could have moved for a short distance due to oscillations. The misalignment can be seen obviously in Figure 9.11. But this issue will not be a big problem as long as all the contact regions were captured in the results.

In terms of the endposts, it should be noted that according to Equation 9.2, the reflection coefficient should not be lower than the bottom limit which equals to $\frac{z_1-z_2}{z_1+z_2}$, the density of the Nylon66 is 1183kg/m^3 , and the density of wheel steel is 8190kg/m^3 . By pulsing a beam of ultrasound signals through a sample material, measuring the pass distance of the signal and checking the responding time of the signal on the PC, the speed of sound in one material can be derived. In this way, the speed of sound in nylon66 and steel is 2600m/s and 5064m/s. By substituting Equation 4.1, the bottom limit of the reflection

coefficient is 0.8619, which is quite close to 1. However in practical measuring work, ultrasound signals can be influenced by a number of uncontrollable factors, and peak to peak values may be lowered because of tiny angle shift of the focusing transducer, electrical noise interference or mechanical oscillation caused by the scanning tank. These all would lead to the reflected coefficients *R* go below the bottom limit. The points where *R* went below the bottom limit were replaced with interpolation. Therefore some contact information were lost in the contact stiffness maps of the endpost. The contact stiffness maps of the 6mm and 10mm endpost are shown in Figure 9.13 and Figure 9.14.

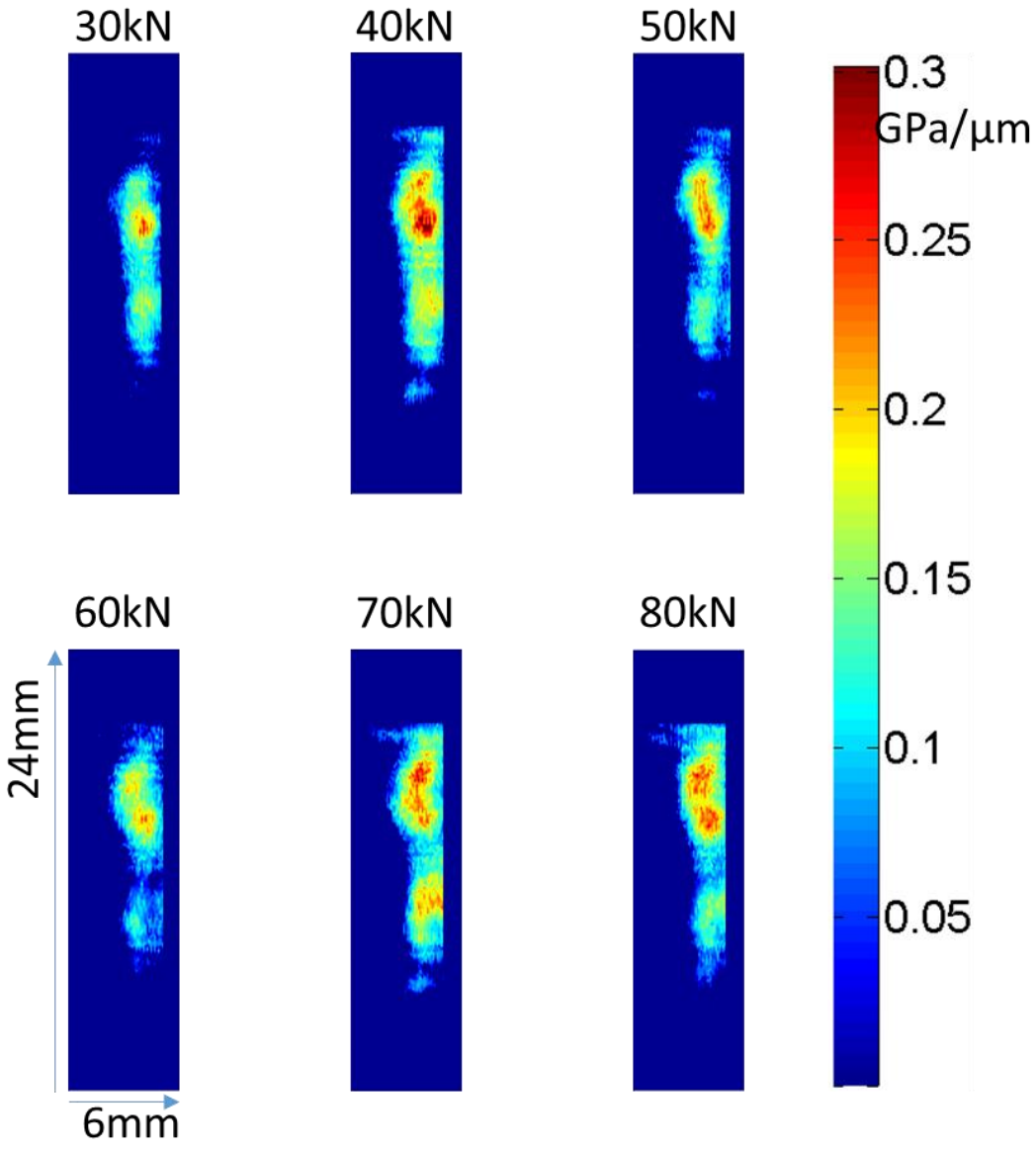

Figure 9.13 Contact Stiffness Maps of 6mm Endpost (Static)

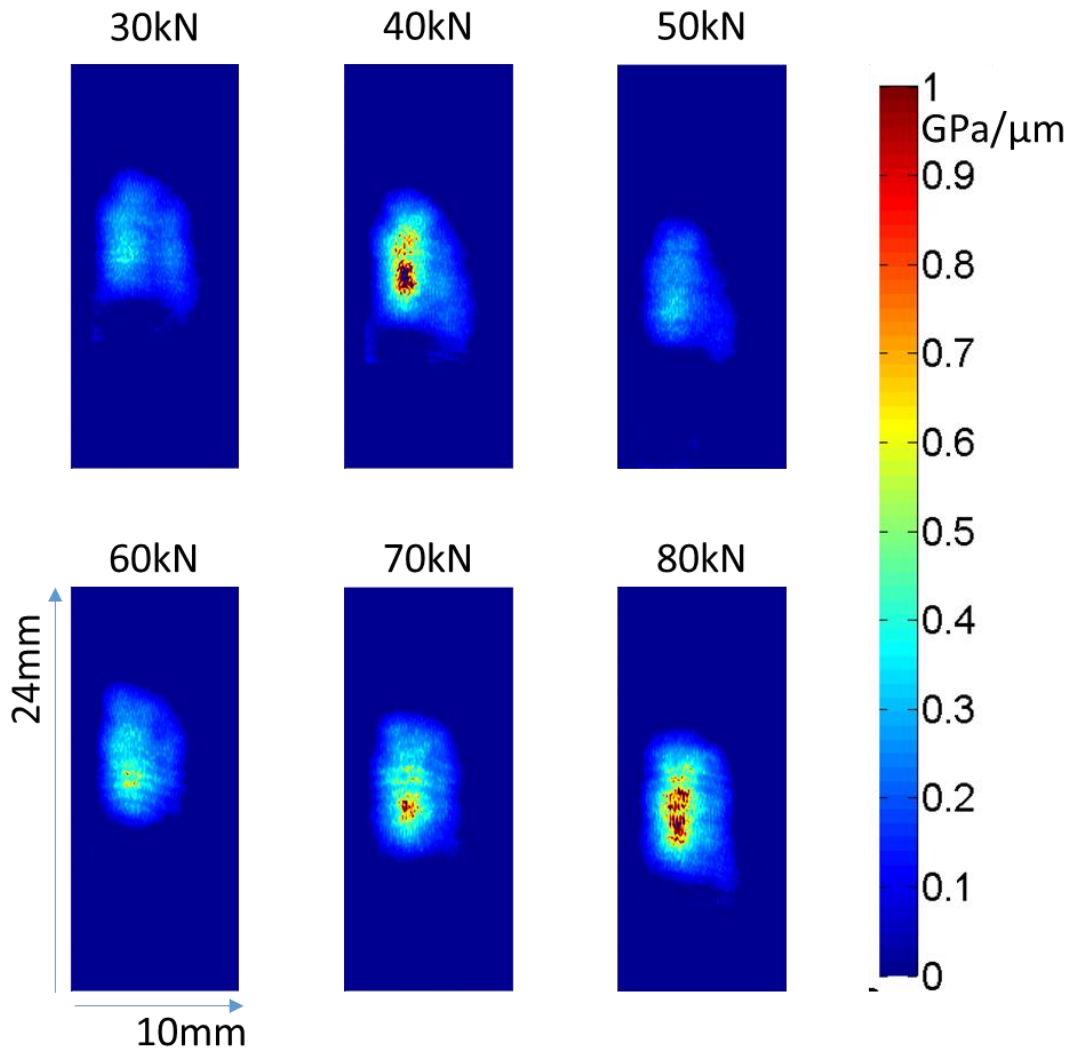

Figure 9.14 Contact Stiffness Maps of 10mm Endpost (Static)

The contact shapes of 6mm endpost appear a little odd in Figure 9.13, this is because information out of contact was all eliminated to emphasis the contact patch in data post-processing. However, this would not be an issue in drawing conclusions.

As with the contact pressure calculation, a calibration curve is needed. However, there is no previous ultrasonic tests on wheel-rail endpost, so it is essential to take a calibration test of steel against nylon to find out the relationship between interfacial stiffness and contact pressure for the roughness pair tested. A nylon cylinder was used in contact with a steel plate. Loads from 20kN to 60kN were applied, in order to match the pressure scale of endpost tests, the diameter of the Nylon calibration cylinder is 26mm. Shown in Figure 9.15 is a reflected voltage map of one calibration test, the pressure distribution cannot be ideally even in the whole contact patch, especially for non-metal material with nonlinear elastic properties.

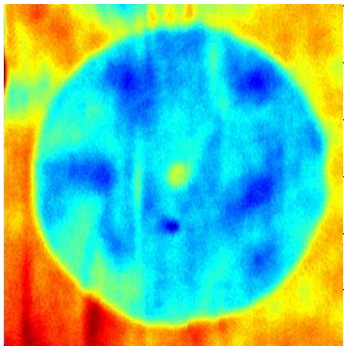

Figure 9.15 Reflected Voltage Map of One Calibration Test

Averages were taken for all the data in the calibration contact patch, and a *K-P* calibration curve was plotted (as shown in Figure 9.16).

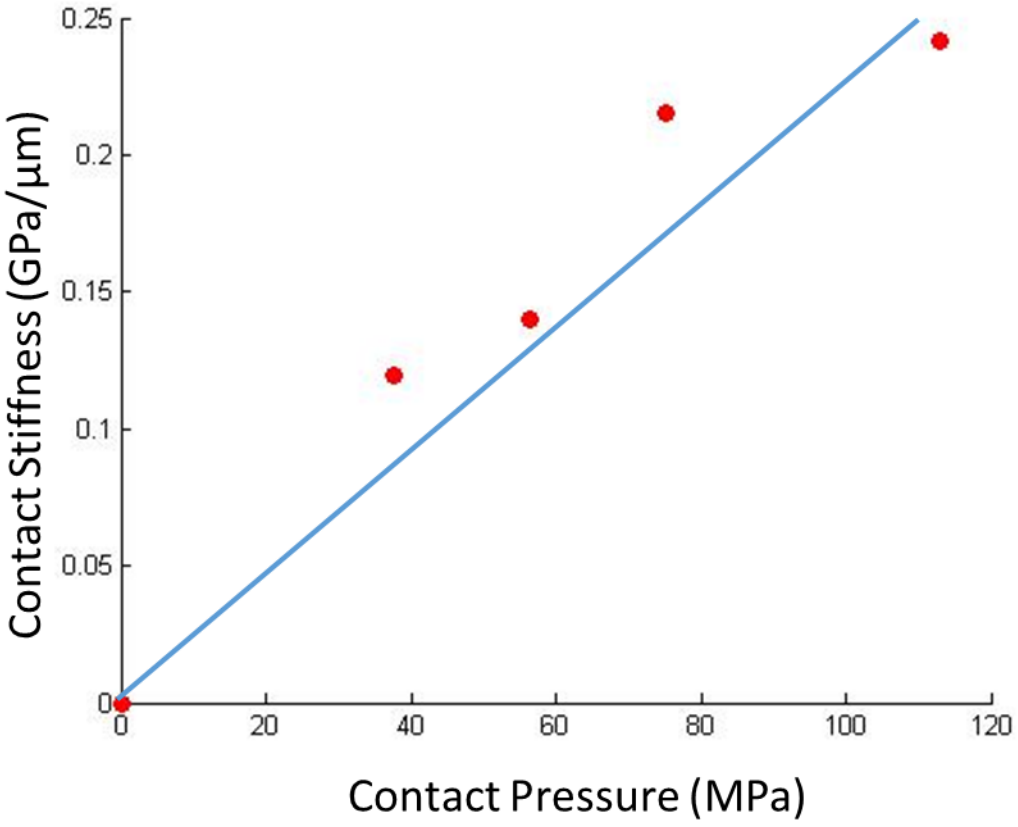

Figure 9.16 Calibration Curve of Steel-to-Nylon Contact

A line could be drawn with the data. The coefficient between contact stiffness and contact pressure is *P=450K*. It should be noted that the calibration test is debatable and can be improved with better equipment for more accurate result.

Since some results of the 6mm endpost and 10mm endpost contacts were interpolated, and a bottom limit was set for the reflection coefficients, maximum contact pressure of the endposts from ultrasound measurements can no longer truly show the contact conditions of wheel-endpost contacts. A line of contract pressure data was extracted along the longitudinal direction, where pressure of rail sections and endposts were all included. Figure 9.17 and Figure 9.18 show the pressure distribution along the longitudinal line.

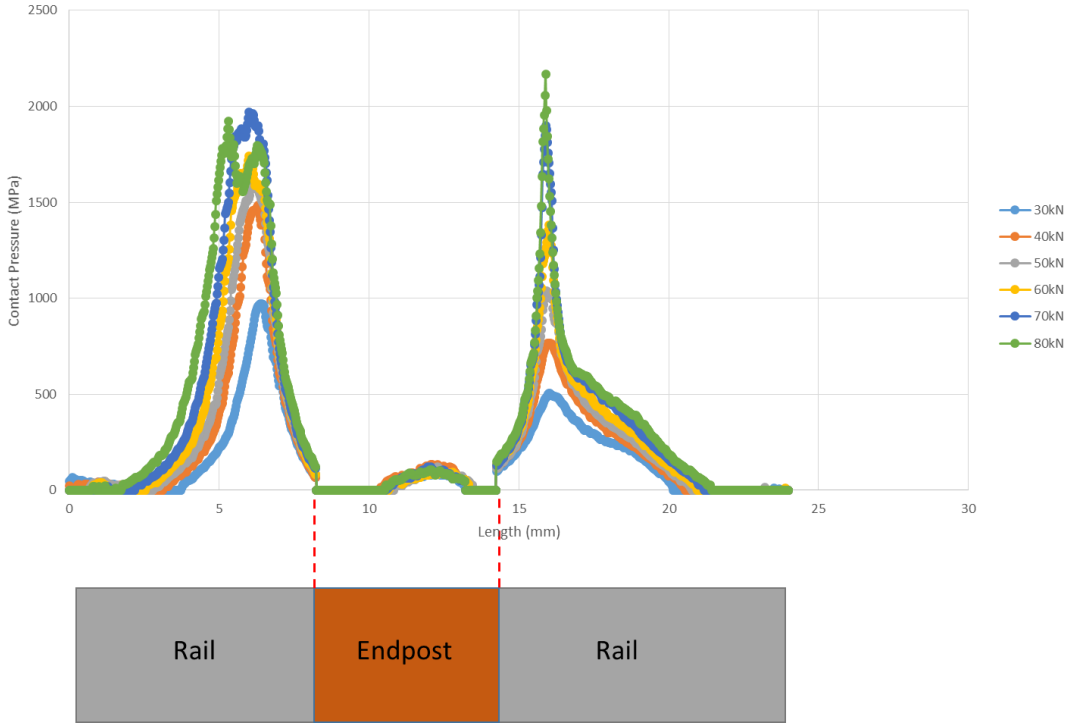

Figure 9.17 Contact Pressure Distribution along the Longitudinal Direction of 6mm Endpost Tests

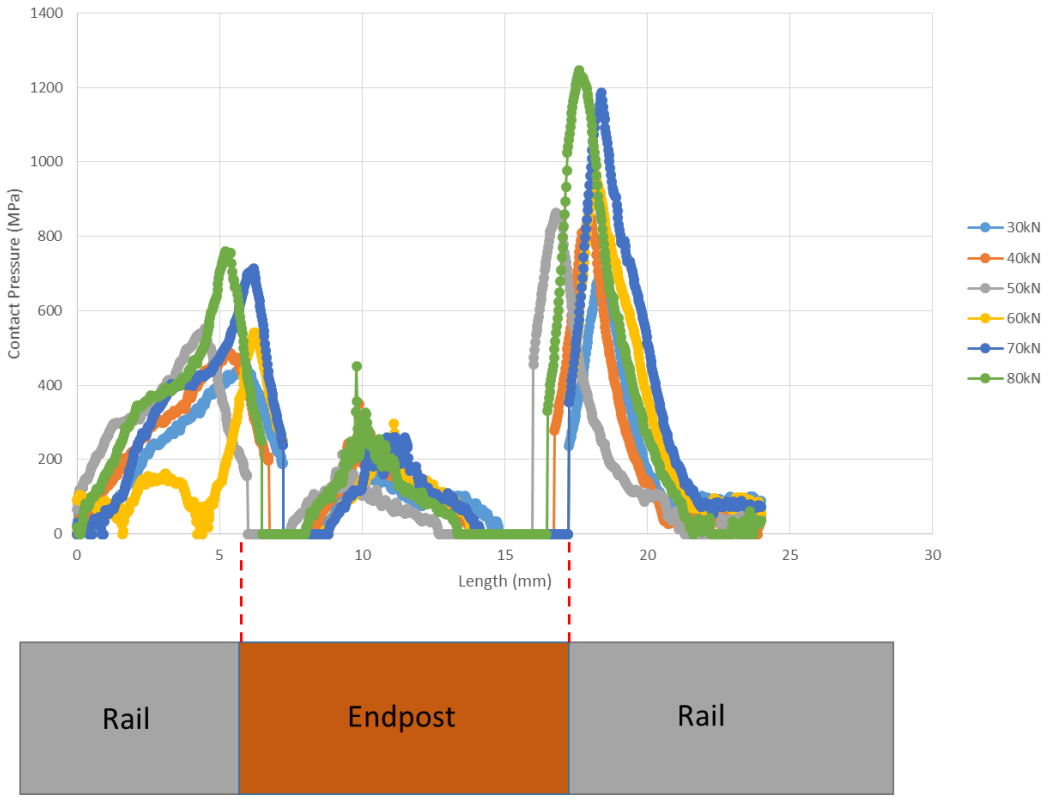

Figure 9.18 Contact Pressure Distribution along the Longitudinal Direction of 10mm Endpost Tests

From Figure 9.17 and Figure 9.18 the average pressure level of the endposts can be observed straight forwardly. Contact pressures of the 6mm endpost were around 100MPa, and pressures of the 10mm endpost were around 200-250MPa.

9.2.4 Finite Element Analysis

The test specimens used in the ultrasonic tests are modelled 1:1 in 3-dimensional modelling software and the contact problem is solved using finite element analysing software ANSYS. Loads from 30kN to 80kN were applied, simulations of 6mm and 10mm endpost were carried out respectively. The mesh of the potential contact regions were refined. The 3D model and meshed model can be seen in Figure 9.19, Young's Modulus and Poisson Ratio of nylon 66 were set as 2.5GPa and 0.4 respectively. The contact initial settings were similar to those in wheel-rail static contact simulations. Simulation results are displayed in Figure 9.20 and Figure 9.21. Here pressure distributions were plotted in different scale for rail sections and endposts, but they were put together for a more clear view.

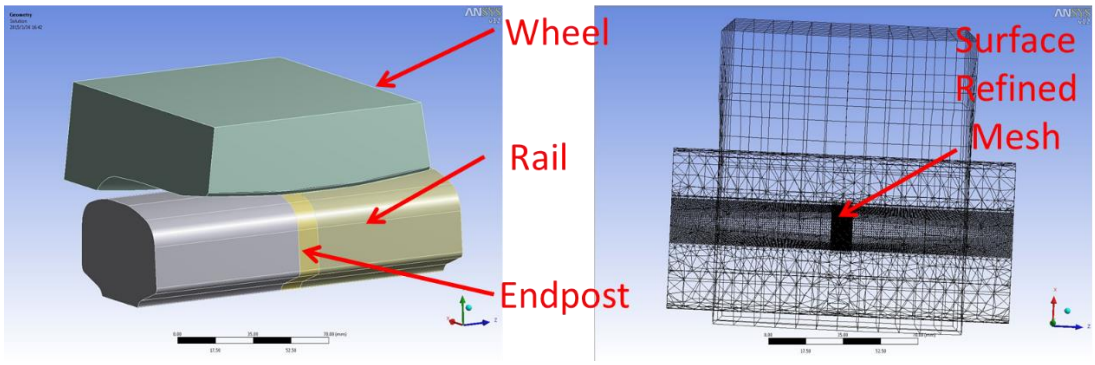

Figure 9.19 3 Dimensional and Meshed Model of Wheel-Rail Endpost Contact

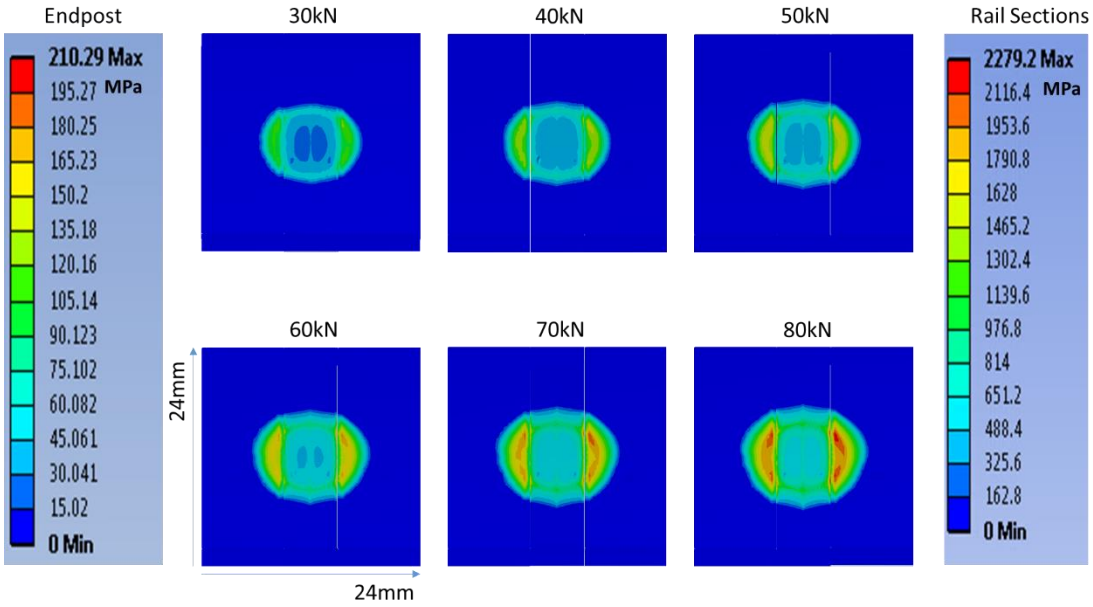

Figure 9.20 FE Simulations of the 6mm Endpost (Static)

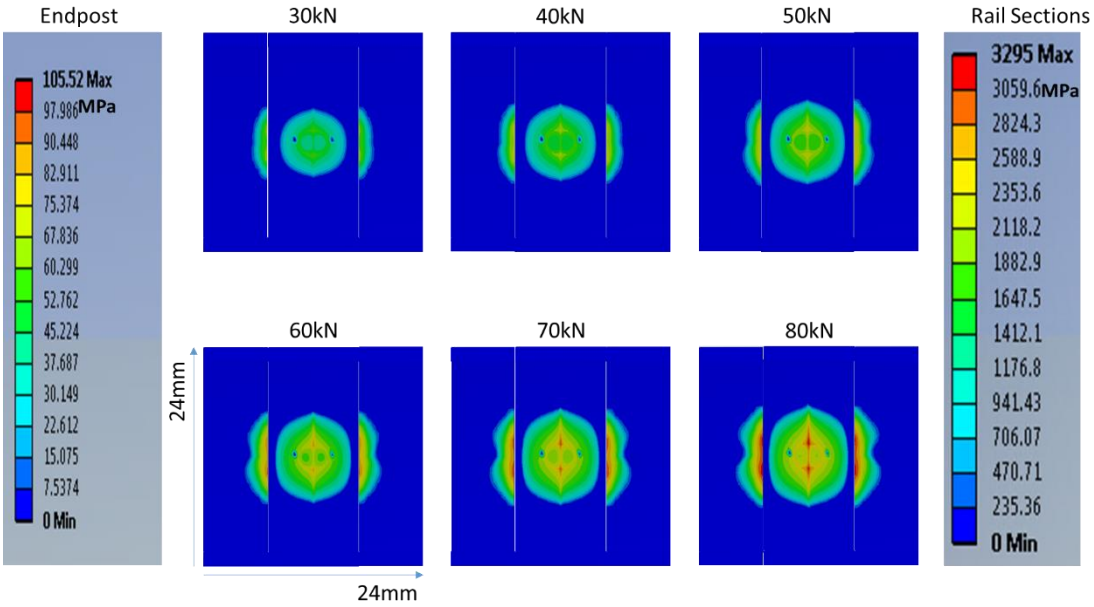

Figure 9.21 FE Simulations of the 10mm Endpost (Static)

The maximum contact pressures in the rail from FE simulations were compared with those from ultrasound measurements (as shown in Figure 9.22 and Figure 9.23).

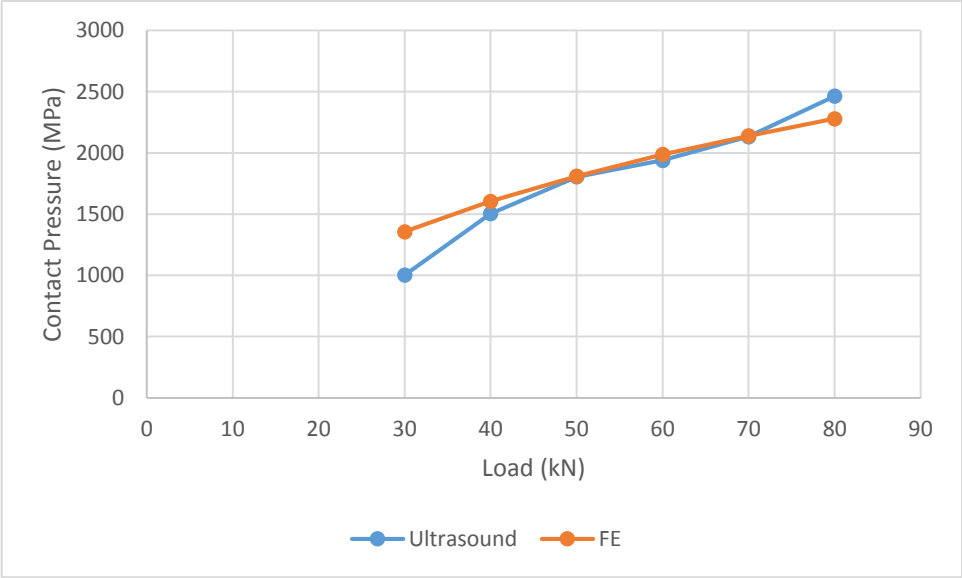

Figure 9.22 Contact Pressure Comparison between Ultrasound and FE of 6mm Endpost Test

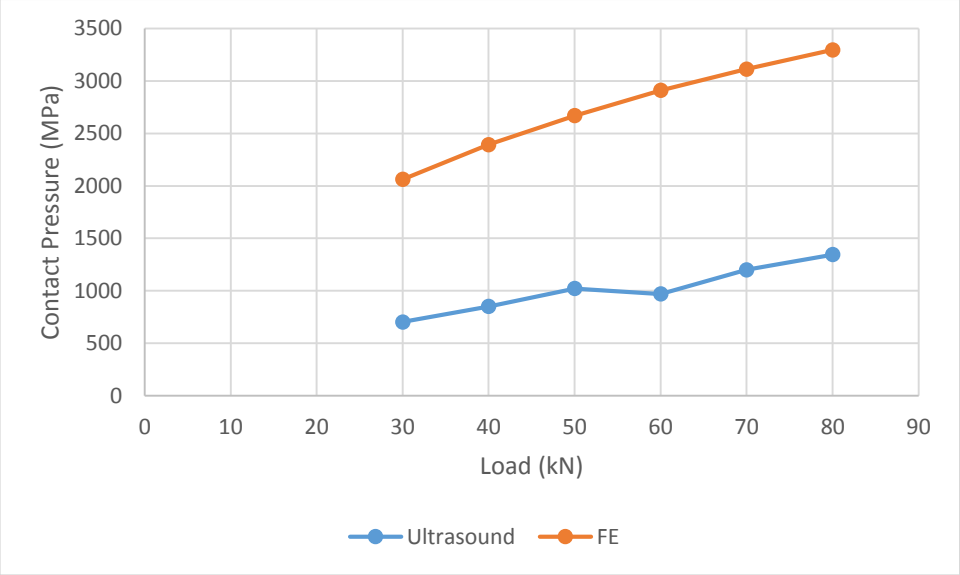

Figure 9.23 Contact Pressure Comparison between Ultrasound and FE of 10mm Endpost Test

9.4 Discussion

From the ultrasound test results and FE simulations in Figure 9.11, Figure 9.12, Figure 9.20 and Figure 9.21, it can be seen that the contact stresses at the edge of the rail sections are much higher than the stress at the endpost. Although the FE simulations Sandstrom and Ekberg has done on endpost were under totally different conditions: different load series, thinner endpost and traction forces taken into consideration, comparing Figure 9.20 and Figure 9.21 with Figure 9.4, the contact pressure distributions basically follow the same trend. In terms of the wheel-rail edge contact shapes, there is not very much difference between tests with 6mm thick endpost and tests with 10mm thick endpost regardless of the unsymmetrical loading, the shape of the contact patches on both ends appears to be narrower and longer than normal wheel-rail contact ellipse. This is also the case in FE simulations. But the contact shapes on the endpost in two series of tests are quite different. As shown in Figure 9.13 and Figure 9.14, the contact patch of 10mm endpost tests is more regular and elliptical and that of 6mm endpost tests appears more like a long strip. Besides, multiple contact patches were seen in 6mm endpost tests (Figure 9.13). This can be explained by the profile of the endposts. Close pictures of both 6mm and 10mm endpost specimens were taken (Figure 9.24). Because the endposts need to be machined to the profile as rail profile, and machine traces were sometimes inevitable. In Figure 9.24, top of the 10mm endpost specimen is relatively smooth, and small corrugations were found on top of the 6mm endpost. When the wheel was pressed over the endpost, it was some peaks of the corrugations that were in contact with the wheel, and this is why more than one contact patch were detected. Contact patches on the endposts from FE simulations may not show the real contact shapes accurately. This may be due to the meshing method and non-linear behaviour of Nylon material. However, the main aim of FE simulations here

is to compare the contact stresses level with results from ultrasound measurements, and it is comparable.

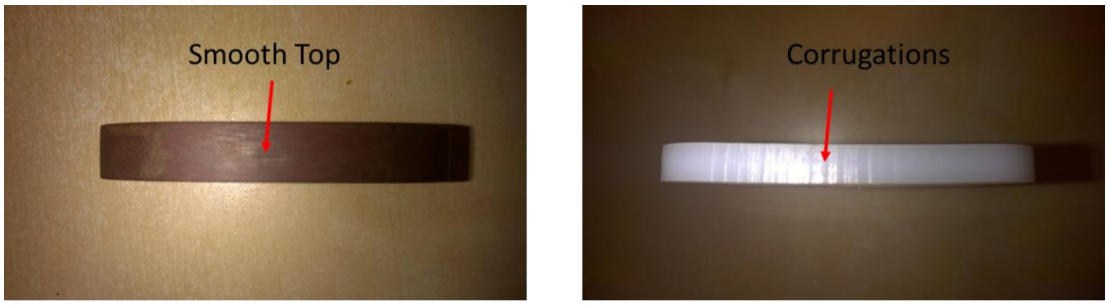

Figure 9.24 Endpost Specimens

As it can be seen from Figure 9.11, Figure 9.12, Figure 9.20 and Figure 9.21, the contact stresses at the rail edges increased as the load went up for both ultrasound measurements and FE simulations. In Figure 9.17 and Figure 9.18, the contact stresses on the endpost, however, hardly any growth can be seen. The contact pressures on the 6mm endpost were around 100MPa under all loads, and those on the 10mm endpost were around 200MPa. This is because when the load is relatively low, the deformation at the endpost is not significant, the wheel is to a certain extent in good contact with the endpost and the contact stress there is positive related with the normal load. As the load kept going up, the endpost starts deforming largely and no full contact between the wheel and the endpost can be held. Contact pressures on the 6mm endpost are generally lower than pressures on the 10mm endpost, this could probably be explained by the corrugations mentioned above as well. Because the maximum stress a peak of the corrugations can afford is lower than the whole top part of the endpost. Contact pressures on the endpost from FE simulations were growing steadily with a maximum of 210MPa for 6mm endpost and 105MPa for 10mm endpost under 80kN.

As with the contact pressures on rail sections, peak pressures were compared between ultrasound measurements and FE simulations. Although in the 6mm endpost case results from both method match each other very well from Figure 9.22, in the 10mm endpost case shown in Figure 9.23, maximum contact pressures from FE were all much higher than ultrasound measurements. Theoretically, thicker endpost means larger gap between two rail sections, and the stress concentration ought to be more severe. Peak pressures from the 10mm endpost tests were generally lower than those from the 6mm endpost tests, which was off the theoretical expectations. The reason could also be the corrugations on the 6mm endpost, when the peaks of corrugations on the 6mm endpost deforms to an extent and no further load would be pressed on the endpost, almost all the load were burdened by the rail sections. Sharp rises and drops of contact pressure were observed on the right rail sections in Figure 9.17, which indicates that there might be some odd point contacts leading to extreme high contact pressure. The FE

simulations deal with models with smooth surfaces and the relative wheel-rail contact positions which is sensitive in FE simulations cannot be set identical to the test conditions. So the FE simulations were used as a reference of theoretical cases and a validation of relative pressure distribution of the endpost and the rail sections.

One more thing which needs to be mentioned is that there regions close on two sides of the endposts were totally not in contact with the wheel (Figure 9.12 and Figure 9.13), this can also be seen from Figure 9.16 and Figure 9.17. When the wheel was pressed against the endpost and rail sections, the whole endpost head deformed normally including regions close to the edges. After that, any increasing loads would be pressed on the rail sections.

Due to limitations of the test equipment, it is difficult to load up the test specimens ideally symmetrical. In most cases, rail section at one side suffer more load that the other side, resulting in different contact patches and contact pressure on two sides. These tests in another way are the real cases as they simulate the instance where the wheel is about to leave one rail section and moves on to the next one.

9.5 Summary

In this chapter, the rail endpost contact was studied using the ultrasound reflectometry. A 6mm and a 10mm thick endpost were tested respectively. This is the first time ultrasound reflectometry was used in scanning compound contacts (metal-metal and metal-non-metal). From the test results, in both series of tests, the pressures near edges of the rail sections were far higher than pressures on the endpost. Contact patches on the rail sections were narrow. This will lead to a rapid wear on the edges of the rails. Contact pressure on the endposts remained still as loads increased, and the contact patches kept roughly the same size. Compared with wear caused by normal pressure, the endpost would suffer more from the compression of the rail sections on both sides once they deformed towards middle under high contact pressure. Results from ultrasound method were compared with FE simulations. Pressures on the rail sections from FE were generally lower than ultrasound measurements for 10mm endpost tests, and higher for 6mm endpost.

Although the mismatch between ultrasound measurements and FE simulations indicates that some improvements are needed in the future. The ultrasound measuring technique has been proven useful in characterising the relative pressure difference between the rail sections and the endpost, and the method managed to plot detailed pressure distributions of real contacts with combined materials. Due to the surface condition difference of the two endpost specimens, the pressures comparison did not meet the expectation. But in real cases, the endpost cannot always be fitted in between

two rail sections perfectly, there might be height difference, profile difference between the endpost and the rail or surface conditions difference between endposts as the case in this chapter. All these mismatches may result the actual pressure values quite different from theoretical predictions, and the ultrasound scanning technique has its advantage in characterising contact of real cases especially with the potential complexities compared with other simulation methods.

Chapter 10:

Conclusions

10.1 Conclusions

In this chapter the conclusions are drawn for the whole project.

In this project, a novel ultrasonic technique has been developed for characterising dynamic contact of machined elements. The contact stresses and contact sizes are measured under different contact cases.

Before applying the ultrasonic technique onto the ball flat contact and wheel rail contact, static measurements were taken on both types of contacts.

The nitrile balls and perspex plate were used as test specimens for static tests so as to provide reference for dynamic measurements. Contact sizes were obtained and contact stresses were derived. The contact sizes acquired from ultrasound measurements match well with Hertz prediction and FEA in low normal loading case, which is same as expected because the nitrile-perspex contact behaves to be full elastic contact. In terms of the contact pressure determination, since no previous research work on characterising contacts between non-linear materials has been done using the ultrasound, especially never on contact stress. There is no similar result or more specifically, no calibration curve which can be referred. A series of calibration tests were carried out using a small and thin nitrile disc in contact with the perspex plate in an attempt to obtain a valid calibration curve. Unfortunately due to the flexible property of nitrile and the limitations of experiment conditions. The contacts in the calibration tests cannot be perfectly symmetrically loaded up, resulting an uneven contact patch. The contact patch was manly divided into four zones according to their average level of contact stiffness. Data from each zone were picked up for plotting calibration curves and eventually four curves were plotted. For pilot study as this case, it's arguable but worthwhile to set up a potential contact pressure –interfacial stiffness zone according to the four curves.

The static wheel rail contact has been studied for many years using different kinds of approaches. Ultrasound measurements similar to what has been done in this project have been carried out by Matt Marshall. But the static tests carried out here were using upgraded software and hardware. The quality of contact pressure distribution figure was proved to be much better than previous work with higher resolution, clear boundaries and less noise. Both contact size and contact pressure measurements from ultrasound match pretty well with those from Hertz prediction and FEA. This is because the contact type investigated is a typical wheel tread to rail head elastic contact, which satisfies the assumptions of Hertz theory well. The maximum contact pressure results from ultrasound are the highest under all loads compared with results from the rest two methods due to stress concentration at the contacting asperities captured by ultrasound.

The novel measuring technique was applied with a 64-element ultrasonic scanning array. And some pilot tests were carried out on nitrile ball-perspex plate contacts. Measurements were taken under a series of normal loads at different speeds. Since the main aim of these tests is to test the applicability of the new technique and provide pilot studies for full scale wheel rail dynamic tests, the contact stress determination is not concerned in this part. Three speeds were tested: 1.4mm/s, 4.2mm/s and 7mm/s. Figures of contact obtained from 1.4mm/s tests are of best quality, contacts under all loads were welly captured. Results at the speed of 4.2mm/s are not that good but all contacts were detected. Results at the speed of 7mm/s are the worst, contacts under low loads can hardly be seen in the figures, but the ones under high loads can be observed. This is due to the limitation of the switching speed of the array program. Higher speed leads to less data been recorded in one full scanning cycle, and the quality of the plots drops. All three sets of tests were focused on rolling contacts. Another set of tests were carried out on 100% sliding contact as comparison, no significant difference was found between sliding and rolling in terms of contact shape and pressure distribution. Besides, three steel balls in contact with a track of groove on a steel rotating plate were measured to test the possibility of taking measurements with the array doing cyclic movements. The result is a little bit faint but promising that all three positions of contacts, although small, are detected by the rotating array. This provides a potential possibility of future tests by attaching similar sensors onto the rotating wheel non-destructively and taking measurements.

With sufficient pilot tests done on small scales, the new technique was eventually moved onto the full scale wheel rail test rig. Contact between a wheel with worn p8 profile and a new UIC60A rail was scanned. The tests were carried out at 1mm/s and 5mm/s, for each speed, loads were applied from 40kN to 120kN with a step of 20kN, and measurements were taken twice under one load as wheel went backward and forward. Due to the worn p8 wheel profile, a couple of contacts were observed in an individual measurement. The contact patch grows gradually as the load increases, but results from a pair of backward and forward tests approximately keep the same, which is good as it shows the stability and repeatability of the scanning method. Results from 1mm/s look very good and much better than those from 5mm/s, but results from 5mm/s are also acceptable. The whole series tests successfully proved the feasibility of the

novel technique. Contact pressures were calculated by referring to calibration curves plotted in previous ultrasound work. The contact pressure results from two speeds were compared with each other and the peak stress is within the normal region. An approach to estimate the contact area was proposed and the contact area results were compared with results from Fuji pressure sensitive films and FEA.

As with the wheel-rail endpost contact, only static measurements were taken as the main concern is to determine contact pressure on the endpost and stress concentration at the railends. The static measurements can offer higher resolution than the ultrasonic array for dynamic tests. FEA was also taken as comparing method. High contact pressures were found around the edges of the rail sections, and the pressures on the endposts kept in a relatively low level for both 6mm tests and 10mm tests. Because it is the first time the ultrasound scanning technique was used on investigating wheel-rail endpost contacts, there are debatable aspects such as the calibration of steel-nylon contact, and mismatch of contact pressures was found in comparison with FEA. In the whole view, the method has been proven successful in characterising contacts of combined materials.

10.2 Future Work

The nitrile ball-on-flat tests will be improved in the future for both static and dynamic cases. Due to the non-linear properties, more calibration tests will be carried out for better revealing the *P-K* relationship. Furthermore, FE simulations of both static and dynamic non-linear ball-on-flat will be taken as a validating method. The difference of ultrasound measurements between rolling and sliding contacts will be further investigated with a faster scanning array. The steel-in-groove dynamic test will be used for actual ball-bearing contacts.

As with the wheel-rail dynamic contact tests, fast rolling speed is on the way for testing with fast array switching speed. And new concepts are under experimenting for faster rolling speed contact characterisation. For instance, by assuming the contacts of continuous 8 wheel-rail cycles be identical, only one channel (8 elements) of the array is measuring in each cycle and consequently merging measurements from all 8 channels in 8 cycles into one and take that as one full measurement. In this case, the switching speed of the array is no longer a limitation and theoretically, the method can be applied in field wheel-rail tests with 50m/s or even more. Another thinking is by attaching ultrasonic transducers on the two sides of the rail, pulsing from one side and receiving from the other side, where no holes needed to be cut or other structure modification needed to be done on the rail. Dynamic tests with attack angles and partial slips will also be planned in the future. Meanwhile, more professional finite element simulations will be taken for dynamic contacts with better modelling and solving approaches.

In terms of rail endpost contact characterisation, further calibration tests will be carried out for wheel-endpost contact, and the wear behaviour near the rail edges will be investigated in the long term. More accurate finite element analysis will be done. Plus, the array is planned to be used for measuring endpost contact dynamically as well.

References

[1] F.W. Carter, "On the action of a locomotive driving wheel", *Proc. R. Soc., London,* 1926, Series A, pp. 151-157.

[2] K.L. Johnson, Contact mechanics, *Cambridge University Press*, 1985.

[3] J.J. Kalker, "Three-Dimensional Elastic Bodies in Rolling Contact", *Kluwer Academic Publishers, Dordrecht/Boston/London,* 1990.

[4] J.J. Kalker, "A Fast Algorithm for the Simplified Theory of Rolling Contact", *Vehicle System Dynamics*, 1982, Vol. 11.

[5] S. Cretu, "The influence of roughness on pressure distribution and stress state of concentrated contacts subjected to normal loads", *Bul. Inst.Polit. Iasi, XLXIII (LVII), 1-2, s. Constructii de masini*, 2007, pp. 1-12.

[6] J.P. Pascal, G. Sauvage, "New method for reducing the multicontact wheel/rail problem to one equivalent rigid contact patch", *Vehicle System Dynamics*, 1991, 20, 1, pp. 475-489.

[7] F.P. Bowden, D. Tabor, "The Friction and Lubrication of Solids", *Clarenden Press, Oxford*, 1950.

[8] H. Fesseler, E. Ollerton, "Contact Stresses in Toroids Under Radid Loads", *Brit. J. Appl: Phys*, 1957, Vol. 8, No. 10, pp. 387

[9] M. Pau, F. Aymerich, F. Ginesu, "Measurements of nominal contact area in metallic surfaces: a comparison between an ultrasonic method and a pressure sensitive film", *Wear,* 2001, Vol. 249 pp. 533-535.

[10] W. Poole, "The measurement of contact area between opaque objects under static and dynamic rolling conditions", *Proceedings of Contact Mechanics and Wear of the Wheel/rail System*, 1987, University of Rhode Island, Waterlooville Press, pp. 59-72.

[11] R. Lewis, R. S. Dwyer-Joyce, "Wear mechanisms and transitions in railway wheel steels", *Proceedings of the Institution of Mechanical Engineers Part J: J. Engineering Tribology*, Vol. 218, pp.467-478.

[12] J.J. Kalker, "A Strip Theory for Rolling with Slip and Spin", *Koninklijke Nederlandse Akademie van Wetenschappen, Series B70,* 1967, pp. 10-62.

[13] J.J. Kalker, "The Tangential Force Transmitted by Two Elastic Bodies Rolling Over Each Other with Pure Creepage", *Wear,* 1968, Vol. 11, pp. 421-430.

[14] O. Polach, “A Fast Wheel-Rail Forces Calculation Computer Code”, *Vehicle System Dynamic Suppl.* 1999, Vol. 33, pp. 728–739.

[15] P. Wriggers, V.T. Van, E. Stein, “Finite Element Formulation of Large Deformation Impact-Contact Problems with Friction”, *Computers and Structures,* 1990, 37, Vol. 3, pp. 319-331.

[16] J.C. Simo, T.A. Laursen, “An Augmented Lagrangian Treatment of Contact Problems Involving Friction”, *Computers and Structures*, 1992, Vol. 42, No. 1, pp. 97-116.

[17] T. Telliskivi, U. Olofsson, “Contact mechanics analysis of measured wheel-rail profiles using the finite element method”, *Institute of Mechanical Engineering Part F*, 2001, Vol. 215.

[18] M. Wiest, E. Kassa, W. Daves, J.C.O. Nielsen, H. Ossberger, “Assessment of methods for calculating contact pressure in wheel-rail/switch contact”, *Wear 265*, 2008, pp. 1439–1445.

[19] M.A. Arslan, O. Kayabas, “3-D Rail–Wheel contact analysis using FEA”, *Advances in Engineering Software*, 2012, Vol. 45, pp. 325–331.

[20] V. Monfared, “Contact Stress Analysis in Rolling Bodies by Finite Element Method (FEM) Statically”, *Journal of Mechanical Engineering and Automation* 2012, 2(2): pp. 12-16.

[21] K. Kendall, D. Tabor, "An Ultrasonic Study of the Area of Contact between Stationary and Sliding Surfaces", *Proceedings of the Royal Society, Series A*, 1971, Vol. 323, pp. 321-340.

[22] A.G. Tattersall, "The Ultrasonic Pulse-Echo Technique as Applied to Adhesion Testing", *J. Phys. D: Appl. Phys*, 1973, Vol. 6, pp. 819-832

[23] B.W. Drinkwater, R.S. Dwyer-Joyce, P. Cawley, "A Study of the Interaction between Ultrasound and a Partially Contacting Solid-Solid Interface", *Proceedings of the Royal Society Series A*, 1996, Vol. 452, No. 1955, pp. 2613-2628.

[24] Hodgson, K., Dywer-Joyce, R.S., Drinkwater, B.W., "Ultrasound as an Experimental Tool for investigating Engineering Contacts", *Proceedings of the 9th Nordic Symposium on Tribology, 'Nordic 2000'*, Eds. Andersson, P., Ronkainen, H., Holmberg, K., 2000, Vol. 2, pp377-386.

[25] A.M. Quinn, B. W. Drinkwater, R.S. Dwyer-Joyce, “The measurement of contact pressure in machine elements using ultrasound”, *Ultrasonics*, 2002, Vol. 39, pp. 495-502.

[26] M.B. Marshall, R. Lewis, R.S. Dwyer-Joyce, O. Olofsson, S. Björklund, “Measuring Wheel/Rail Contact Stresses using Ultrasound”, *14th International Wheelset Congress*, 2004.

[27] M. Pau, “Estimation of real contact area in a wheel-rail system by means of ultrasonic waves”, *Tribology International 36*, 2003, pp. 687–690.

[28] J. Blitz, “Fundamentals of Ultrasonics”, 1963, London, England: Butterwoths.

[29] M.B. Marshall1, R. Lewis, B.W. Drinkwater, R.S. Dwyer-Joyce, “An ultrasonic approach for contact stress mapping in machine joints and concentrated contacts”, *Journal of Strain Analysis*, 2004, Vol. 39 No. 4.

[30] T.R. Thomas, R.S. Sayles, "Stiffness of Machine Tool Joints: A Random-Process Approach", Transaction of the *ASME, Journal of Engineering for Industry*, 1977, No. 76-WA/Prod-23.

[31] H.P. Brunskill, L. Zhou, R. Lewis, M.B. Marshall, R.S. Dwyer-Joyce, “Dynamic Characterisation of the Wheel/Rail Contact using Ultrasonic Reflectometry”, *Proceedings of the 9th International Conference on Contact Mechanics and Wear of Rail/Wheel Systems (CM2012)*, Chengdu, 2012.

[32] J. Sandstrom, A. Ekberg, “Numerical Study of the Mechanical Deterioration of Insulated Rail Joints”, *Proceedings of the Institution of Mechanical Engineers, Part F: Journal of Rail and Rapid Transit,* 2009, Vol. 223, pp. 265-273